GENERALIZED SYNTHESIS METHODOLOGY OF NONLINEAR SPRINGS FOR PRESCRIBED LOAD-DISPLACEMENT FUNCTIONS

by

Christine Vehar Jutte

A dissertation submitted in partial fulfillment
of the requirements for the degree of
Doctor of Philosophy
(Mechanical Engineering)
in The University of Michigan
2008

Doctoral Committee:

Professor Sridhar Kota, Chair
Professor Debasish Dutta
Professor Scott J. Hollister
Professor Gregory M. Hulbert

To Mom and Dad,

and

My dear husband, Andy.

Thank you for your love and support.

ACKNOWLEDGEMENTS

I am humbled by the generous ways that individuals have impacted my life. At the culmination of my doctoral work, I would like to recognize those who have been especially supportive and influential during my years at the University of Michigan.

I would like to thank my advisor, Professor Sridhar Kota, for his support and guidance throughout my graduate career. Under his mentorship, I have grown as a researcher and in turn become a stronger person. I am grateful to Professor Kota for understanding and appreciating my passion to make a difference in the world as an engineer, as this often influenced my choice of research topics. By listening to my ideas and providing valuable insight, Professor Kota guided me toward rewarding and worthwhile doctoral research. I am especially thankful to him for making the necessary and sometimes inconvenient adjustments to remain as an effective advisor despite my move to California. Overall, it has been a privilege to work with Professor Kota, and I thank him for his friendship and constant belief in me.

Other professors at the University of Michigan have also made an impact on my doctoral research. Members of my doctoral committee, Professor Debasish Dutta, Professor Scott Hollister, and Professor Gregory Hulbert, provided valuable advice and asked thought provoking questions that challenged me to address this research in a more thorough manner. Professor Shorya Awtar provided helpful explanations and offered new perspectives on my work.

I would be remiss if I did not acknowledge several individuals who strongly influenced my professional growth and career path. Dr. Kevin Hallinan from the University of Dayton and Dr. Mary Frecker from Pennsylvania State University provided me valuable advice pertaining to my research and career decisions. Ms. Mary Legatski, my mentor from the Washington Internships for Student of Engineering program in 2001, continued to support my professional growth during my years in graduate school.

Many thanks are extended to my colleagues in the Compliant Systems Design Laboratory at the University of Michigan. They include Dr. Charles Kim, Dr. Kerr-Jia Lu, Dr. Tony Tanakorn, Dr. Brian Trease, Mr. Zachary Kreiner, Mr. Michael Cherry, Ms. Audrey Plinta, Mr. Dragan Maric, Mr. Young Oh, Ms. Froukje Euwe, and Mr. Girish Krishnan. Their friendship and humor have made my days in room 2231 G.G. Brown truly memorable. Over the years, I have learned a great deal from my fellow lab members and am appreciative of all the insightful conversations we held in the lab. It has been an honor to share these years with such an intelligent and talented group of people. I am also grateful for the friendship and encouragement of another friend at the University of Michigan, Dr. Ercan Dede.

I would not have been able to reach this point in my life had it not been for my parents, Eileen and Ray. I am forever grateful for their love and encouragement along with the opportunities they have provided me. Their support, prayers, and perspective have helped me maintain a positive attitude throughout this graduate school experience. I would also like to thank my siblings, Ken, Kris, Ryan, and Mike and my in-laws, Betsy, Laverne, and Lisa for being a constant support system. In particular, I am grateful to Ryan's engineering insights and Lisa's advice on the doctoral research process.

I owe a very special note of gratitude to my dear husband, Andy. His constant support has enabled me to face the challenges of a doctoral degree and strive for my full potential. His companionship and love uplifted me during the busiest of times and made these years incredible. I am grateful that Andy always understood when I had to devote more time to work and less time to us. Thankfully, Andy and I were able to marry and move to California in the midst of this doctoral degree. Our wedding day on May 20, 2006 will always remain the highlight of my years at the University of Michigan and my life.

I would also like to acknowledge the National Science Foundation for funding me with a graduate research fellowship, the University of Michigan's Rackham Graduate School for supporting me with a Rackham Engineering Award and a Margaret Ayers Host Award, and the University's Department of Mechanical Engineering for its support over the last five and a half years.

I have been truly blessed with a wonderful opportunity at the University of Michigan. The support of the people mentioned above, along with the rest of my friends and relatives not mentioned, will always be appreciated. As I move forward, I am challenged to use all I have learned and gained from this experience to mentor and inspire others and make positive impacts on society.

TABLE OF CONTENTS

LIST OF TABLES

LIST OF FIGURES

CHAPTER 1

INTRODUCTION

Compliance, the flexibility of a material or structure, is prevalent in nature's designs. Biologist Steven Vogel (1998) claims that many of nature's designs exploit nonlinear compliance, usually via material nonlinearities, for better performance within their environments. Nature's management of *stiffness,* the inverse of compliance, is directly related to its exploitation of strain energy, the area underneath a stress-strain curve. When nature requires large amounts of strain energy to be stored, its material's stress-strain curve resembles a *softening* curve, as shown in Figure 1-1(a), whose curvature encompasses a large amount of area underneath the curve. A tendon is one biological tissue that exploits this stress-strain relationship. By storing large amounts of energy, even under small displacements, tendons are able to increase the efficiency of walking by first storing strain energy and then returning it during segments of the motion cycle. In contrast, when guarding itself against crack propagation, nature favors materials having minimal strain energy absorption as shown in Figure 1-1(b). This *hardening* stress-strain response is typical of skin (Vogel, 1998).

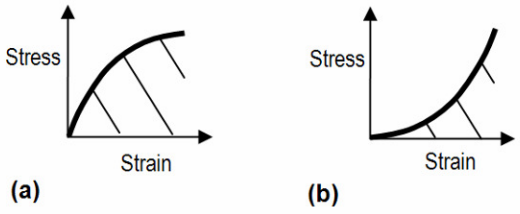

Figure 1-1: (a) Softening stress-strain curve; (b) hardening stress-strain curve.

Engineers also exploit compliance. By integrating compliance within a design, the Design-for-No-Assembly approach reduces a product's part count in order to minimize assembly costs (Buscemi, 2004). For example, a snap-fit, which is functionally compliant, eliminates the need for a fastener by geometrically locking two adjacent parts together as shown in Figure 1-2(a). Similarly, a toothpaste cap (Figure 1-2(b)) and one-piece salad tongs (Figure 1-2(c)) also utilize compliance.

(a) (b) (c)

Figure 1-2: Compliance in commercial products: (a) snap-fit, (b) toothpaste cap, and (c) salad tongs.

Like nature, engineers also employ compliance for energy storage purposes; however, most fabricated energy storage devices are *linear*, such as a helical spring. This dissertation explores the design and application of devices having *nonlinear* compliance. The foundation of this work is based on a more recent area of research, compliant mechanism design.

1.1 Compliant Mechanisms

Conventional mechanisms transfer force and motion by utilizing multiple rigid links and kinematic joints. Their design theory is well developed due to a century of research and application. In the past two decades, researchers have integrated compliance into mechanism design theories. The resulting designs are compliant mechanisms, which transfer force and motion by exploiting the flexibility of their members. These mechanisms are typically one-piece and joint-less. Their absence of joints offers benefits including the reduction of friction, wear, and backlash

(Ananthasuresh and Kota, 1995). Figure 1-3 illustrates a compliant gripper mechanism (Lu and Kota, 2006).

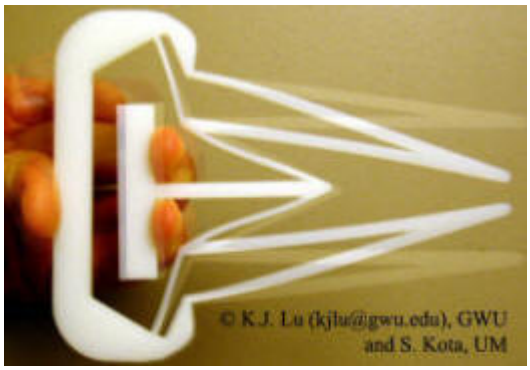

Figure 1-3: Compliant gripper mechanism (Lu and Kota, 2006).

Compliant mechanisms are categorized by their mode of force and motion transmission as shown in Figure 1-4. A *fully compliant mechanism* uses the elasticity of all of its members to transmit force and motion; thus, stress is likely distributed throughout the entire mechanism. A *lumped compliant mechanism* (e.g. toothpaste cap) employs its elasticity at a finite number of locations, while the rest of the mechanism is relatively rigid. As shown in the lumped compliant mechanism in Figure 1-4, these designs typically consist of thin flexural regions adjacent to thicker rigid regions, making their manufacturing more difficult and increasing the presence of stress concentrations. Finally, a *hybrid compliant mechanism* uses an assembly of both compliant and rigid components to transmit force and motion.

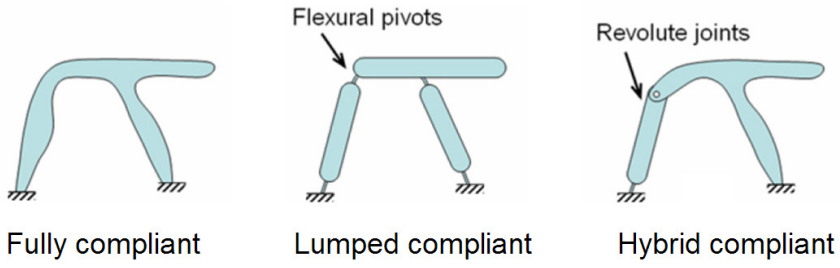

Figure 1-4: Categorization of compliant mechanisms (Lu, 2004).

1.2 Nonlinear Springs

Nonlinear springs are a class of compliant mechanisms having a defined nonlinear load-displacement function (Figure 1-5) measured at one point on the mechanism. This point is referred to as the input. All of the work applied at the input is absorbed as strain energy within the mechanism; hence, this dissertation refers to the mechanism as a spring. A spring's load-displacement function also defines its strain energy absorption rate, since the integral of the load-displacement function equals the spring's strain energy as shown in Figure 1-5. Various applications benefit from a nonlinear spring's load-displacement function (strain energy absorption rate).

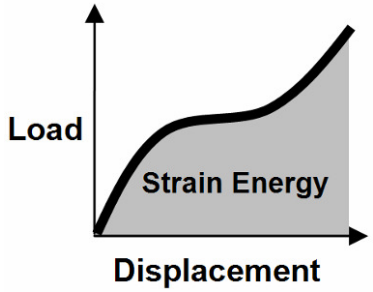

Figure 1-5: The solid black curve defines a nonlinear spring's load-displacement function and its strain energy absorption rate.

1.2.1 Applications

The following paragraphs expound upon four areas of nonlinear spring application. Additional applications include statically balanced mechanisms (Herder, 2001), shock absorbers (Parmley, 2000), designs for crashworthiness (Pedersen, 2004), and robotic joints (Migliore et al., 2007).

Prosthetics and Artificial Implants

Heel Region Properties in a Prosthetic Foot

During walking or running, a person applies large and varying impact loads on the heel. Therefore, the heel property regions of a prosthetic foot greatly affect the amputee's comfort and health. Klute et al. (2004) find that heel regions of prosthetic feet are viscoelastic and greatly vary from one product to another. Since viscoelastic materials are modeled as a J-curve spring in parallel with a damper, specific material

properties could be synthesized using a nonlinear spring in conjunction with a damping material.

Intervertebral Disc Implant

Spinal instability and lower back pain are often caused by intervertebral disc injury or degeneration (Klisch and Lotz, 1999). The disc is best modeled as a poroelastic material, having both a fluid and a porous, elastic solid-matrix. The annulus fibrosus, the solid-matrix, experiences multiaxial stresses *in vivo* and is modeled as an anisotropic nonlinear material due to a composite layering of collagen fibers. Although the springs developed in this work are constrained to behave orthotropically, the synthesis methodology offers a first-step approach to the design of implants that mimic biomechanical materials.

MEMS

Nonlinear behavior improves the performance of various microelectromechanical system (MEMS) devices, including actuator suspensions and bandpass filters. The patented MEMS actuator suspension by Rodgers (2005) uses nonlinear tensile forces to resist electrostatic actuation forces. A MEMS bandpass filter, which attenuates frequencies outside a prescribed bandwidth, has the potential to improve wireless communications. Rhoads et al. (2005) are developing such devices by using parametric resonances, while similar resonance characteristics are attainable with a nonlinear spring-mass system (Bajaj and Krousgrill, 2001).

Constant-force Springs

Various applications benefit from constant-force springs, a class of nonlinear springs. In Howell's (2001) dimensional synthesis work for constant-force compliant mechanisms, he referred to numerous applications that would benefit from a constant force spring, including:

1) Electronic connectors that sustain connection despite disturbances and part tolerances

2) Gripping device for fragile parts of different sizes
3) Coupling device between a machine and its end-effector that enables application of a constant force (relevant to wear testing and glass pane scoring)

Human Interfaces

High-end products offer their user superior support and tactile interfaces through nonlinear devices, including the lumbar supports on office chairs and knobs, dials, and switches found on cars and electronics. Chapter 8 demonstrates the design of a nonlinear spring that mimics the nonlinear response of a foam seat cushion.

1.2.2 Limitations of Conventional Spring Designs

A limited selection of nonlinear springs are available in the market. For instance, Figure 1-6 shows a constant-force spring, and Figure 1-7(a) shows a conical spring. These designs are limited to the coiled configurations illustrated in the two figures. Thus, their designs are not adaptable to specific space requirements. Secondly, to fully define a nonlinear spring's load-displacement function, designers specify a spring's (i) nonlinear stiffness rate, (ii) load-range, and (iii) displacement-range. In trying to match all three factors, it is rare that a designer finds a suitable spring that is commercially available. Figure 1-7(b) shows a nonlinear spring constructed from commonly available linear springs. However, the inherent stiffness discontinuities in dual (or multiple) helical spring assemblies are unavoidable (Parmley, 2000). Thus, a method for designing customized springs would address these limitations.

Figure 1-6: A constant-force spring (www.vulcanspring.com).

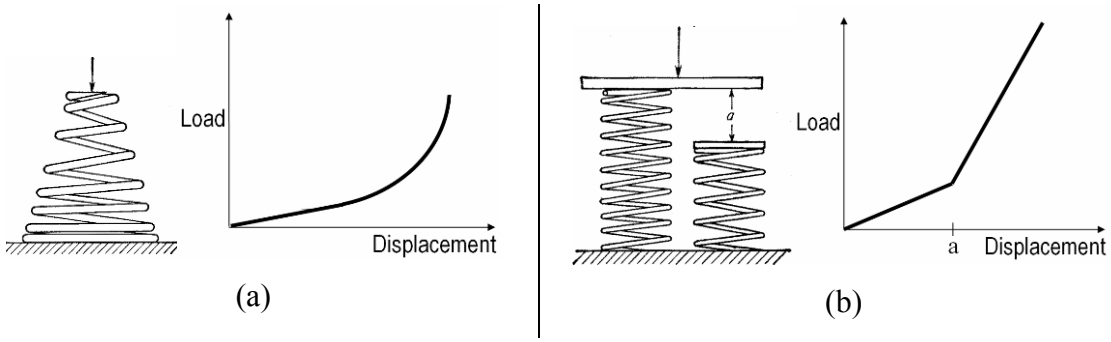

Figure 1-7: (a) Conical spring; (b) dual helical spring (Parmley, 2000).

An assembly of linear springs connected to a conventional rigid-link mechanism can also create nonlinear spring behavior. Jenuwine and Midha (1994) created spring-mechanisms for specified energy absorption by performing dimensional synthesis on the generalized spring-mechanism configuration shown in Figure 1-8; the spring-mechanism has two linear springs. Although these spring-mechanisms may be suitable in some applications, the designer is limited to one topology and the design consists of numerous links, joints, and springs. These limitations can be avoided with an equivalent nonlinear spring.

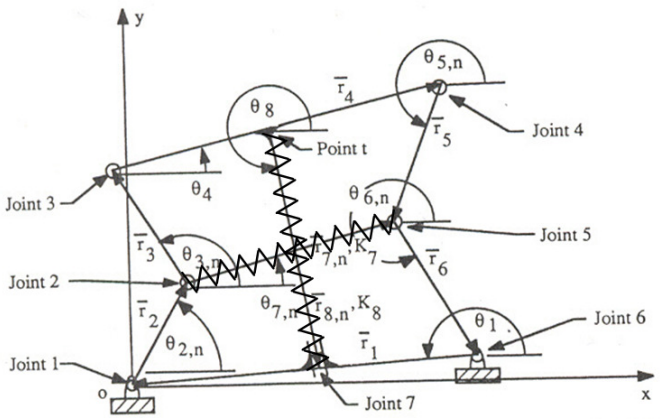

Figure 1-8: A multi-jointed spring-mechanism configuration (Jenuwine and Midha, 1994).

1.3 Geometric Nonlinearities

Rather than using multi-link mechanisms or multiple linear springs, this research explores the creation of nonlinear compliant mechanisms (springs) with distributed compliance. Structural nonlinearities generate nonlinear responses within devices. They include the following: (i) geometric nonlinearities, (ii) material nonlinearities, and (iii) change-in-status nonlinearities, such as noncontact-to-contact or slack-to-tension. Figure 1-9 illustrates their differences. Geometric nonlinearities generate structural nonlinearities through large deformations and rotations and may produce instabilities such as buckling. Material nonlinearities arise from yielding (elastic-to-plastic), responses to environmental changes such as temperature, and nonlinear stress-strain relationships due to constitutive laws (Levy and Spillers, 2003). Unlike material nonlinearities, geometric nonlinearities are not inherent to material properties and can be created or avoided by design. Change-in-status nonlinearities have abrupt changes in stiffness as shown in Figure 1-9. Geometric nonlinearities can prevent these discontinuities when designed to avoid buckling. This work investigates the exploitation of geometric nonlinearities to generate desired nonlinear responses.

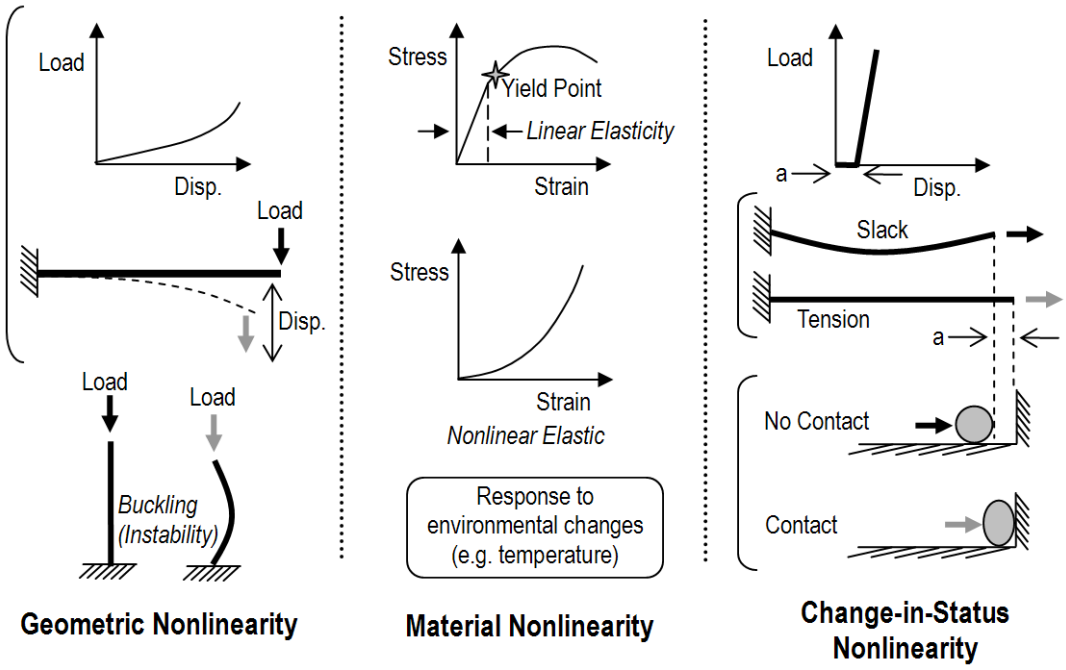

Figure 1-9: Three types of structural nonlinearities.

1.4 Closure

Since each nonlinear spring application requires a unique load-displacement function, nonlinear spring configurations must be custom designed. Currently, no generalized design methodology for nonlinear springs exists. Due to the complex nature of geometric nonlinearities, there is no intuitive approach to designing springs that exhibit desired nonlinear responses. To further complicate the problem, a spring design must also meet specified manufacturing, space, stress, and material constraints, which all pose tradeoffs with geometric nonlinearities. For instance, Figure 1-10 shows that a cantilever beam's geometric nonlinearities increase with a thinner cross-section, a longer length, relatively large end loads or displacements, and a lower modulus of elasticity. Table 1 depicts typical active constraints (e.g. manufacturing and stress) that bound the noted parameters. The obvious tradeoffs result in a challenging optimization problem for engineers. Thus, a systematic approach which exploits geometric nonlinearities, distributes stresses, and optimizes designs for desired nonlinear responses is required. This dissertation presents a generalized nonlinear spring synthesis methodology that (i)

synthesizes a spring for *any* prescribed nonlinear load-displacement function and (ii) generates designs having distributed compliance.

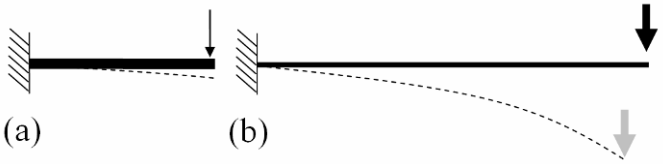

Figure 1-10: Two cantilever beams with beam (b) having a more prominent geometric nonlinearities than beam (a).

Table 1-1: Tradeoffs in nonlinear spring design.

Properties/parameters that increase geometric nonlinearities	Typical active constraints
Minimal in-plane thickness	Manufacturing constraints
Maximum length	Space constraints
Maximum input load or displacement	Stress constraints
Low modulus of elasticity	Material constraints

1.5 Organization of the Dissertation

This chapter introduced nonlinear springs and the general design problem being addressed in this dissertation. The next chapter reviews the relevant work in the area of compliant mechanism design and further distinguishes this work from others. Chapter 3 sets up the generalized nonlinear spring problem and provides an overview of the general design approach, whereas Chapter 4 provides the specific details of the generalized nonlinear spring synthesis methodology. Chapter 5 employs the methodology and presents four spring design examples. Chapter 6 investigates previously generated nonlinear spring designs to interpret how their shape, topology, and loading (i.e. axial and bending) influence their responses. Chapter 7 offers guidelines for arranging nonlinear springs in series and parallel and also provides scaling rules. Chapter 8 presents the results for two nonlinear spring designs that were fabricated for application and validation purposes. Chapter 9 extends the methodology to design anisotropic springs and compliant mechanisms; it also discusses manufacturing options for these springs. Finally, Chapter 10 summarizes the conclusions, contributions, and future work of this dissertation.

CHAPTER 2

LITERATURE REVIEW

Previous work in compliant mechanism design has focused primarily on the structural optimization approach, which determines the topology, shape, and size of a compliant mechanism. Topology optimization identifies the configuration of a mechanism's elements including the number, arrangement, and interconnectivity. A mechanism's topology largely influences its kinematics (Ananthasuresh et al., 1994). Shape/geometry optimization determines specific locations of the elements, and size optimization determines the elements' cross-sectional dimensions.

Most structural optimization methods for compliant mechanisms utilize linear analysis to approximate a mechanism's response. Linear analysis is generally acceptable for small displacement compliant mechanisms. When displacements are larger, linear analysis becomes less accurate in predicting a mechanism's response, hindering the optimizer from generating suitable topologies. Joo and Kota (2004) illustrated the differences between optimal topologies generated using linear and nonlinear analysis. When employing linear analysis, topologies were identical to one another even when optimized for different input displacements (both small and large). However, using nonlinear analysis, a unique topology was generated for each input displacement, justifying the importance of nonlinear analysis in large displacement compliant mechanism synthesis.

Since the research presented in this dissertation generates compliant mechanisms/springs having significant geometric nonlinearities, the following sections expound on various compliant mechanism synthesis methodologies employing nonlinear analysis. Whether optimizing for small or large displacements, the general approach to compliant mechanism synthesis has typically been the same. Readers interested in

learning more about earlier synthesis methodologies using linear analysis may either refer to Kim (2005) for a summary or the following selected works: Ananthasuresh et al., 1994; Frecker et al., 1997; Sigmund, 1997; Hetrick and Kota, 1999; Joo et. al, 2000; and Lu and Kota, 2003.

2.1 Spring Synthesis versus Compliant Mechanism Synthesis

The majority of this chapter reviews compliant mechanism synthesis methodologies as opposed to spring synthesis methodologies since the spring design problem has yet to be addressed. By transforming a compliant mechanism problem into a spring problem, some of the existing synthesis methodologies may also be appropriate for the generalized nonlinear spring problem. However, *the spring problem is more constrained than the mechanism problem*, since the mechanism problem is not required to match a prescribed strain energy absorption rate. As indicated in Figure 2-1, nonlinear compliant mechanisms achieve a nonlinear response *between separate input and output points* by exploiting geometric nonlinearities, boundary conditions, and the strain energy absorption rate. A nonlinear spring's response is *defined by its strain energy absorption rate*; therefore, it may only exploit geometric nonlinearities and boundary conditions to achieve a nonlinear load-displacement function. Thus, the spring problem has fewer design degrees of freedom.

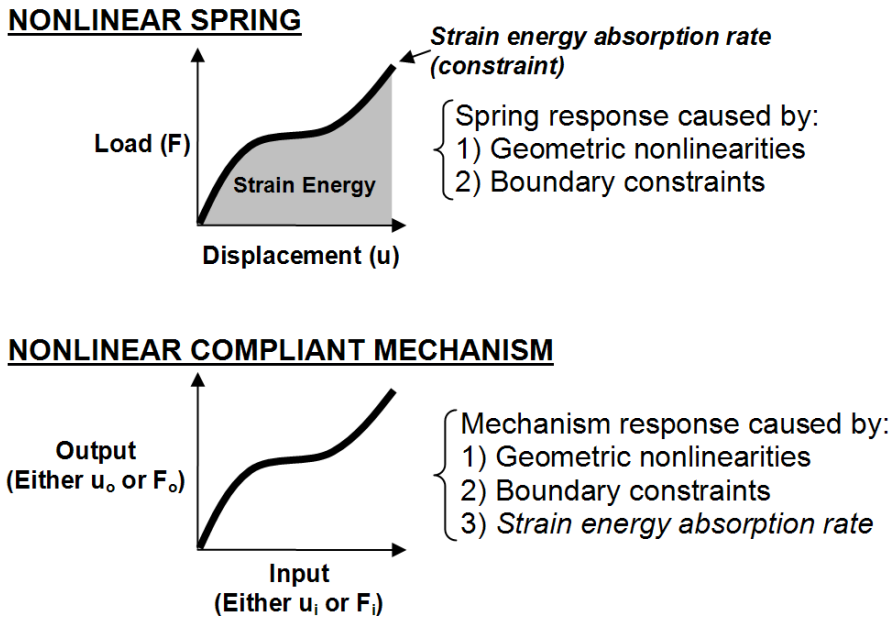

Figure 2-1: A comparison of a nonlinear spring (coincident input and output point) to a nonlinear compliant mechanism (separate input and output points). Unlike a compliant mechanism, a spring has a specified strain energy absorption rate.

2.2 Design Parameterization

This section provides further detail on the structural optimization method and compares various design parameterizations employed in existing synthesis methods. Structural optimization typically follows four steps. First, the design space is defined. This includes specifying (i) the space's overall dimensions and (ii) the location and boundary conditions of the input, output, and ground. Second, the design space is parameterized to represent different topologies using a single set of design variables. The modification of these variables creates new designs. Third, via an optimization scheme, designs are generated and evaluated based on the desired performance. The mathematical representation of the desired performance is contained within the objective function and constraints formulated by the designer. The optimization proceeds until an optimal set of values for design variables is found. Finally, the physical compliant mechanism is interpreted from the optimal design generated in the third step (Lu and Kota 2006).

In Step 2, the design space is generally discretized using either continuous or discrete design variables. The choice of design parameterizations, whether continuum-

based or discrete, can greatly influence a methodology's performance. Lu and Kota (2006) provided an excellent overview of the advantages and drawbacks of the two types of design parameterizations. A summary of continuum-based and discrete design parameterizations is provided below. Most of the works cited in this section are further elaborated on in Section 2.3, Relevant Work.

Two approaches are typical of continuum-based parameterizations. The first is the homogenization approach, which discretizes the design space using a mesh of quadrilateral elements as shown in Table 2-1(Step 2, first column). The second is the ground structure approach, which discretizes the design space using a network of truss or frame elements as shown in Table 2-1(Step 2, second column). In both cases, an element's contribution to the overall mechanism is indicated by a continuous design variable with upper and lower (non-zero) bounds. The variable commonly indicates an element's material modulus or cross-sectional area. The variable's lower bound is typically set to a value close to zero to maintain a fully connected topology while also indicating insignificant (or absent) elements within the topology.

Table 2-1: An illustration of topology optimization using two continuum parameterizations, (i) homogenization and (ii) ground structure (Lu and Kota, 2006).

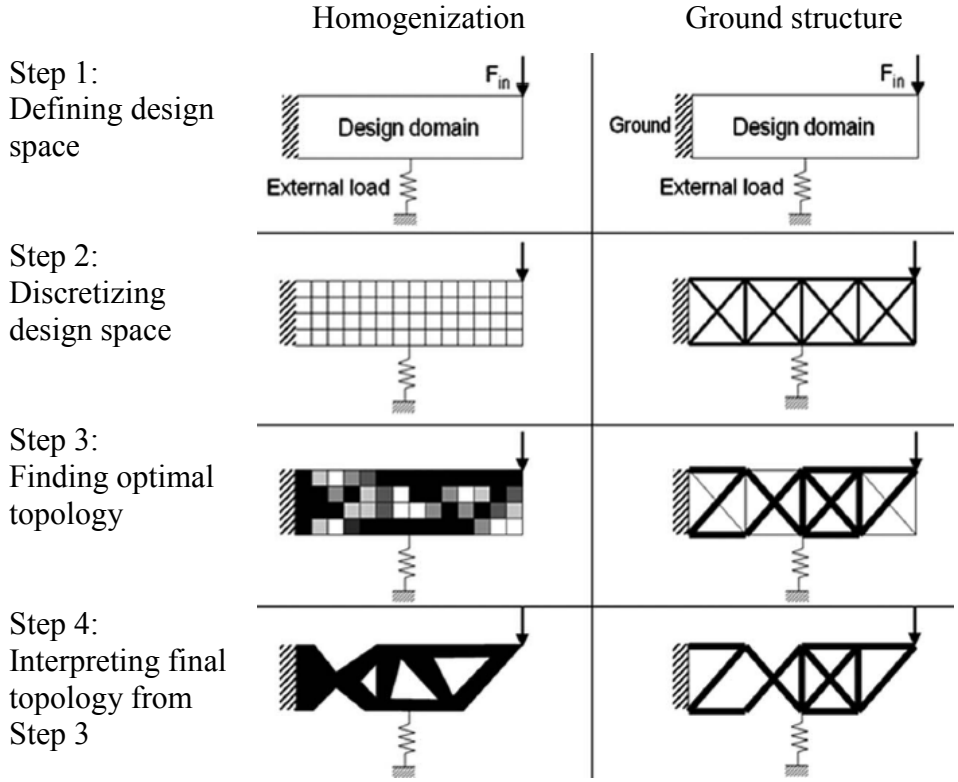

Table 2-1(Step 3) illustrates optimal topologies typical of the two approaches. The darker elements have a greater contribution in the topology than the lighter elements. Intermediate "gray" elements also exist. These gray elements complicate the interpretation of a final design, since the designer must determine which elements are present or absent from the topology in Step 3. Table 2-1(Step 4) shows one designer's interpretation of the topologies. Several works (Buhl et al., 2000; Bruns and Tortorelli, 2001; Pedersen et al., 2001) employ filtering schemes and penalties to eliminate gray elements below a prescribed threshold. However, these automated procedures can lead to disconnected designs. Another interpretation issue relevant to the homogenization approach is the appearance of hinges within the topologies. This occurs when two dense elements are connected by a single point and have adjacent low density elements (Figure 2-2(a)). The point acts as a rotational joint with a finite torsional stiffness, creating high stress concentrations and manufacturing complexities (Pedersen et al., 2006). Several works (Pedersen et al., 2001; Pedersen et al., 2006) employ a post-processing step to

replace the hinges with flexures (short beams) as shown in Figure 2-2(b). These flexures improve a topology's physical representation; however, high stress concentrations typically remain in the region which could decrease the life of the mechanism.

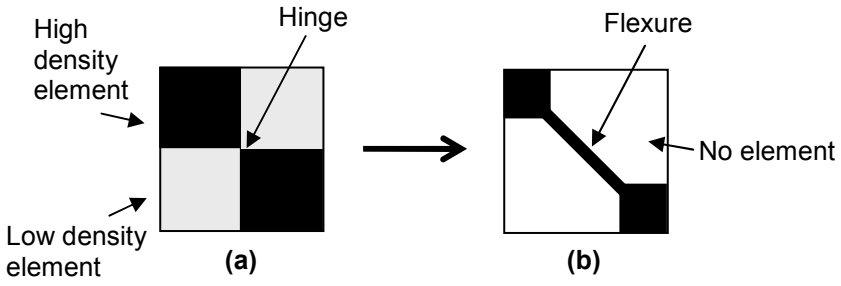

Figure 2-2: A hinge feature (a), typical of the homogenization approach, being converted into a flexure (b) in a post-processing step.

A discrete parameterization overcomes the interpretation issues apparent in the continuum-based parameterizations. Discrete variables enable elements to either be absent or present within a design; thus eliminating the 'gray area' interpretation step (Step 4). Discrete variables however can also generate disconnected structures and thus hinder the efficiency of the optimization. A fully connected structure is one that connects the input, output, and ground points. Connectivity in discrete parameterizations has been addressed in several ways. Some researchers passively avoid disconnected structures, by checking for connectivity after the design has been generated. Zhou and Ting (2005) employed spanning tree theory to check for connectivity, while Rai et al. (2006) simply checked the stiffness matrix for singularity. If a design is not fully connected, it is either discarded or highly penalized within the optimization. Other researchers actively avoid disconnected structures by employing a design parameterization that ensures a full connection between the input, output, and ground points. For example, Tai and Akhtar's (2005) design parameterization connected the input, output, and ground with three Bezier curves, which were then mapped to a mesh of quadrilateral elements. Lu and Kota (2006) extended this work by including three or more load paths (paths of beam elements between the input, output, and ground) as design variables within the parameterization. In both works, resulting topologies had full connection and no ambiguous gray elements. The parameterization presented in this dissertation includes similar characteristics.

A final distinction between continuum-based and discrete design parameterizations is their implementation into an optimization scheme. Gradient-based optimization algorithms, e.g. sequential quadratic programming, are only amenable to continuous variables, while discrete optimization algorithms, e.g. a genetic algorithm, are more suitable for discrete variables. Each type of optimization scheme has its advantages and shortcomings. Gradient-based algorithms generally outperform genetic algorithms in computational efficiency since they exploit information about the local solution space, whereas a genetic algorithm does not have this ability. However, a genetic algorithm is more likely to find a global optimum, since it more thoroughly explores the design space by beginning with multiple initial designs. A gradient-based algorithm begins with only one initial design, and therefore is likely to find a local optimum but not necessarily the global optimum.

2.3 Relevant Work

Since the research presented in this dissertation generates springs having significant geometric nonlinearities, this section reviews various design methodologies for *large displacement (nonlinear)* structures and compliant mechanisms, which implement the design parameterizations mentioned above. The performance of these methodologies is then evaluated with respect to the generalized nonlinear spring design problem.

2.3.1 Nonlinear Structures/Springs

Like a spring, a structure is not a force/motion transmission device, and therefore, any external disturbance is simply absorbed as strain energy within the structure. However, when optimizing structures, the primary goal is to design the stiffest structure by minimizing the absorbed strain energy. To approximate geometric nonlinearities under larger loads, a few researchers have employed nonlinear analysis within their structural synthesis methodologies. Buhl et al. (2000) and Bruns and Tortorelli (2001) both utilized homogenization design parameterizations and nonlinear analysis to minimize the strain energy absorbed in large displacement structures.

Other researchers have investigated structural topology optimization for crashworthiness in order to match a prescribed energy absorption rate upon impact. An

overview can be found in Pedersen (2004). A material nonlinearity, plasticity, is exploited to meet the specified nonlinear strain energy absorption rate.

This dissertation differs from the work above by designing *fully elastic* structures, i.e. springs, for any given nonlinear strain energy absorption rate. In the absence of material nonlinearities, the structural design must exploit geometric nonlinearities.

2.3.2 Nonlinear Compliant Mechanisms

Structural Optimization Methods

Over the last six years, many researchers have implemented nonlinear analysis into topology optimization of compliant mechanisms. In some works, compliant mechanisms were simply designed for a single input load or displacement (not a *range* of input loads or displacements) and typically optimized for a single performance metric, including maximum geometric advantage, minimum strain energy, or maximum efficiency. Bruns and Tortorelli (2001), Joo and Kota (2004), and Zhou and Ting (2005) applied nonlinear analysis to the single input, single output problems to accommodate larger input loads or displacements. Each used a different parameterization approach, i.e. homogenization, continuum ground structure, and binary ground structure, respectively.

At the same time, other researchers were employing nonlinear analysis to design compliant mechanisms for a *range* of input loads or displacements, making these works more relevant to the methodology presented in this dissertation. As shown in Figure 2-1, mechanisms were designed for a prescribed nonlinear response between separate input and output points. In all cases, the designs were optimized for minimum errors relative to the prescribed responses.

Pedersen et al. (2001) presented the design of path generation mechanisms having prescribed output paths for known input paths. The prescribed output paths were defined by M target points that correlated with M input displacements. Since the design space was discretized using the homogenization approach, resulting topologies included gray areas and hinge points. Pedersen et al. (2006) extended the methodology to create nonlinear transmission mechanisms given an actuator characteristic at the input and a prescribed constant-force response at the output. Since Pedersen et al.'s work more

closely relates to the research in this dissertation, it will be expounded upon in the next section.

Saxena and Ananthasuresh (2001) presented compliant mechanisms with prescribed input-force versus output-displacement relationships. A continuum ground structure parameterization was employed. One example optimized three crimper designs for respective nonlinear input-force versus output-displacement relationships. Another example optimized pliers for a curved output path. In both cases, resulting topologies indicated lumped compliance, e.g. structure-like trusses connected to one another via short flexural regions. The final example optimized a floppy drive mechanism, which was essentially a spring design since the input force and output displacement were both measured at the same location. The prescribed load-displacement relationship however was linear.

Tai and Akhtar (2005) presented two straight-line path generating mechanisms, one in the horizontal direction and the other in the vertical direction. For the design parameterization, three Bezier curves connected the input, output, and ground. After being optimized for shape and size, the curves were mapped to a mesh of quadrilateral elements. The resulting topologies had jagged profiles, requiring a subsequent post-processing step to smooth and refine the designs.

Rai et al. (2006) presented three large displacement compliant mechanisms, a displacement inverter, a straight line mechanism, and a curved path mechanism. Each design had a set of prescribed output displacements corresponding to input forces. A binary ground structure was employed. Instead of straight frame elements, each frame element followed a Hermite cubic curve whose endpoints were fixed on the ground structure. Rai et al. included a check to ensure that beam elements did not contact one another during deformation.

Section 2.4 further discusses these works with respect to the research presented in this dissertation.

Pseudo-Rigid-Body-Model

Aside from the structural optimization approaches above, the pseudo-rigid-body model approach (Howell, 2001) employs a completely different method for developing large displacement compliant mechanisms. This method essentially converts known,

rigid-link mechanism topologies into compliant mechanisms by replacing the conventional joints with flexures (Paros and Weisbord, 1965; Howell and Midha, 1994). Using this approach, established rigid-link mechanism synthesis techniques are transferable to the design of compliant mechanisms. The dependence on existing topologies however makes the method less generalizable than structural optimization methods. Yet this approach led to the design of constant-force springs, which will be further detailed in the next section.

A pseudo-rigid-body-model approximates a compliant mechanism's behavior via an assembly of components comprising rigid-links, conventional joints, and torsional springs. Howell (2001) provides a library of flexible members and their respective pseudo-rigid-body-models. Each model has a set of parametric equations that analyze the flexible member's load-displacement response. Therefore, given a topology, pseudo-rigid-body-models enable a designer to predict the behavior of large displacement compliant mechanisms without employing complex numerical analyses, such as finite element analysis.

2.3.3 Two Constant-force Examples

Two of the previous compliant mechanism design methodologies generated constant-force designs. The following examples illustrate the results.

Example 1

Howell et al. (1994) demonstrated the design of a constant-force spring using the pseudo-rigid-body model approach. The initial topology was chosen from a set of 28 pseudo-rigid-body model topologies enumerated specifically for constant-force springs (Murphy, 1993). Figure 2-3 shows the chosen pseudo-rigid-body-model topology, a slider mechanism. By replacing both the pin joints and torsional springs with flexible segments (defined as small-length flexural pivots) the topology is converted to a fully compliant mechanism as shown in Figure 2-4. With a horizontal input load at the slider and a small vertical disturbance, the un-deformed configuration in Figure 2-4(a) deforms to the configuration in Figure 2-4(b). By optimizing the dimensions of the rigid links and the flexible segments, the final design responded with a constant-force load-displacement function at the input.

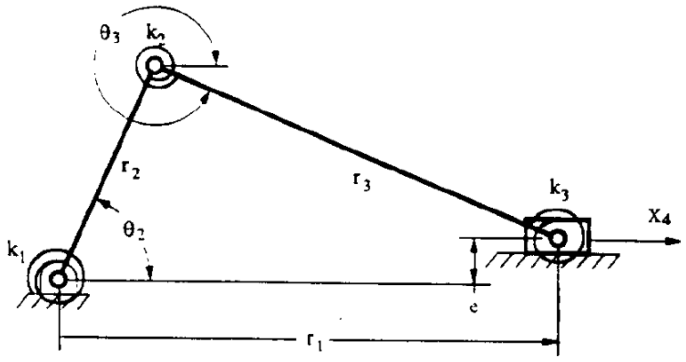

Figure 2-3: The pseudo-rigid-body-model for a slider mechanism

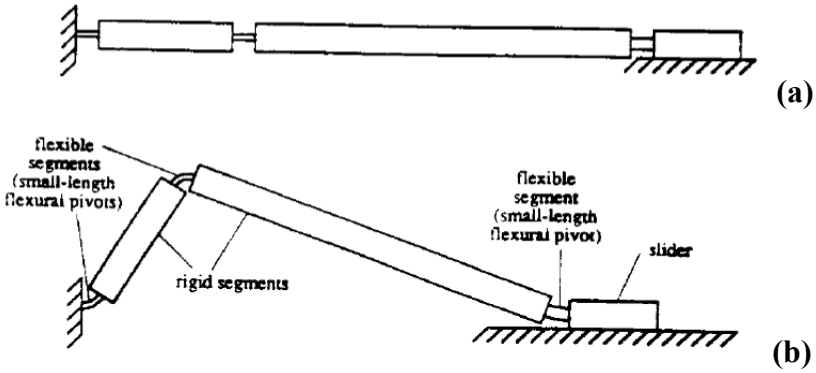

Figure 2-4: The topology of a slider mechanism converted to a compliant mechanism via flexible segments. (a) Un-deformed configuration; (b) deformed configuration (Howell et al., 1994).

Example 2

Pedersen et al. (2006) developed a methodology for designing a compliant mechanism in parallel with an actuator, such that a point on the overall system had a constant output force over a range of output displacements. The resulting designs are not truly nonlinear springs, since an actuator with a negative stiffness is also embedded within the system. However, the design is still optimized for a nonlinear load-displacement relationship at one point on the compliant mechanism, and therefore it is discussed below.

The methodology includes homogenization and two optimization loops. The outer loop maximizes the magnitude of force at the output, while the inner loop optimizes a topology corresponding to that force. Figure 2-5(a) shows one of the resulting topologies. Since the topologies consist of gray elements and hinge points, the designer

converts the topology into beam elements, by substituting hinge areas with slender beams and rigid regions with thick beams. This step is greatly affected by the designer's interpretation of the parent model. Size optimization is then executed on the beam model to achieve the original behavior of the parent continuum topology. Figure 2-5(b) shows the final design consisting of continuum finite elements.

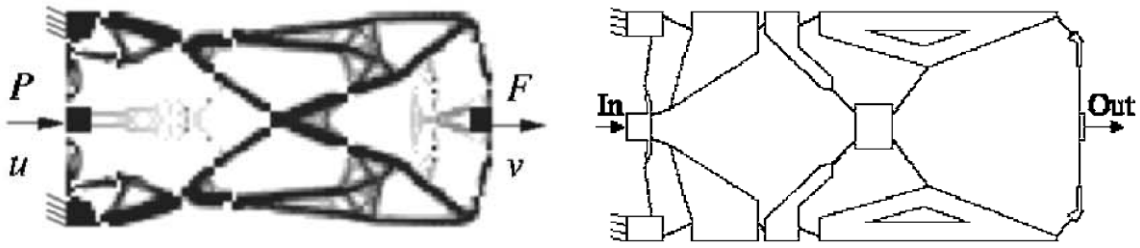

(a) (b)

Figure 2-5: Resulting topologies for a compliant mechanism transmission mechanism with a constant-force response at the output. (a) Parent continuum topology; (b) final design after interpretation and size optimization (Pedersen et al., 2006).

2.4 Closure

Researchers have implemented nonlinear analysis into compliant mechanism synthesis methodologies, but the primary focus has been on large displacement mechanism design not spring design. The spring design problem is more constrained since a spring's load-displacement function defines its strain energy absorption rate. With compliant mechanism design, the strain energy absorption rate is an extra design degree of freedom. In only two cases have these methodologies been used for spring design, but both examples only demonstrated constant-force responses and their designs resulted in lumped compliance (Figure 2-4 and Figure 2-5), making them more difficult to manufacture and prone to stress concentrations. A synthesis methodology is needed which can design nonlinear springs for a *range* of applications. Thus, this dissertation presents a generalized nonlinear spring methodology that (i) synthesizes a spring for *any* prescribed load-displacement function and (ii) generates designs with *distributed compliance*.

Lastly, existing methodologies employ nonlinear analysis to adequately approximate geometric nonlinearities in their designs; however, none of the design

parameterizations have been specifically tailored to *encourage geometric nonlinearities*. Whether continuous or discrete, the majority of the design parameterizations use the *jagged/segmented* homogenization or ground structure approaches, whereas *curvilinear/long* members are more conducive to geometric nonlinearities. To refine jagged/segmented designs, several researchers have developed shape optimization routines using curvilinear members (Xu and Ananthasuresh, 2003; Zhou and Ting, 2006; Lan and Cheng, 2007). These procedures however are refinement steps and do not influence the topology. Two works mentioned in Section 2.3.2 implement curves into their initial topology parameterizations. However, Rai et al.'s (2006) designs are still quite segmented due to the underlying ground structure, and Tai and Akhtar (2005) constrain themselves to a mesh of quadrilateral elements instead of smooth beam elements. This dissertation presents a specific use of curves (splines) making the design parameterization conducive to geometric nonlinearities, offering a degree of nonlinearity that has not yet been explored in the compliant mechanism field.

CHAPTER 3

PROBLEM STATEMENT

3.1 Design Objective

The goal of this work is to develop a generalized methodology for synthesizing nonlinear springs for *any* given load-displacement function. As illustrated in Figure 3-1, three parameters describe a load-displacement function, (A) the shape function, (B) the load-range, and (C) the displacement-range. Of the three, the shape function is the most challenging to match since it encompasses the nonlinearities of the problem. A designer specifies a load-displacement function along with space, material, and stress constraints. Since springs function within their elastic range, the maximum stress never exceeds the material's yield point. The goal is to generate the topology, shape, and size of a spring that meets the designer's specifications. The designs developed in this work are planar, leaving the synthesis of spatial designs as a future extension of this work. To ensure smooth, un-abrupt spring responses, buckling is undesirable. Furthermore, designs that overlap or contact themselves during deformation are more difficult to manufacture and analyze. Therefore, desirable designs are entirely planar, i.e. planar in both their initial configuration and throughout their range of motion.

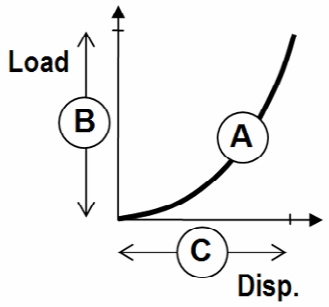

Figure 3-1: A nonlinear spring's load-displacement function with (A) shape function, (B) load-range, and (C) displacement-range.

3.2 Synthesis Methodology Overview

Figure 3-2 illustrates an overview of the nonlinear spring synthesis methodology presented in this work. First, the designer defines the design specifications including a prescribed load-displacement function along with space, material, and stress constraints. These specifications determine (i) the bounds for various design variables and (ii) the objective function, a formulation for evaluating a spring design's performance. If an exact displacement-range is prescribed (C in Figure 3-1), the designer has the option to scale the design specifications in order to improve optimization performance. (The next chapter provides further details about this step.) The optimization (a genetic algorithm) then begins by creating a set of random design variables that represent a group of initial designs. The design variables are then mapped to finite element spring models via a nonlinear spring design parameterization that was developed in this research. Each spring design is analyzed by nonlinear finite element analysis and then evaluated by the objective function. Once all the springs are evaluated, the termination criteria is checked. If the criteria are not met, the design variables are modified, creating new nonlinear spring designs and requiring another iteration of optimization. Otherwise, the best design is retrieved as the optimal design. The designer has the option to scale the optimal design to better match the prescribed load-displacement function. In the end, the final design is determined.

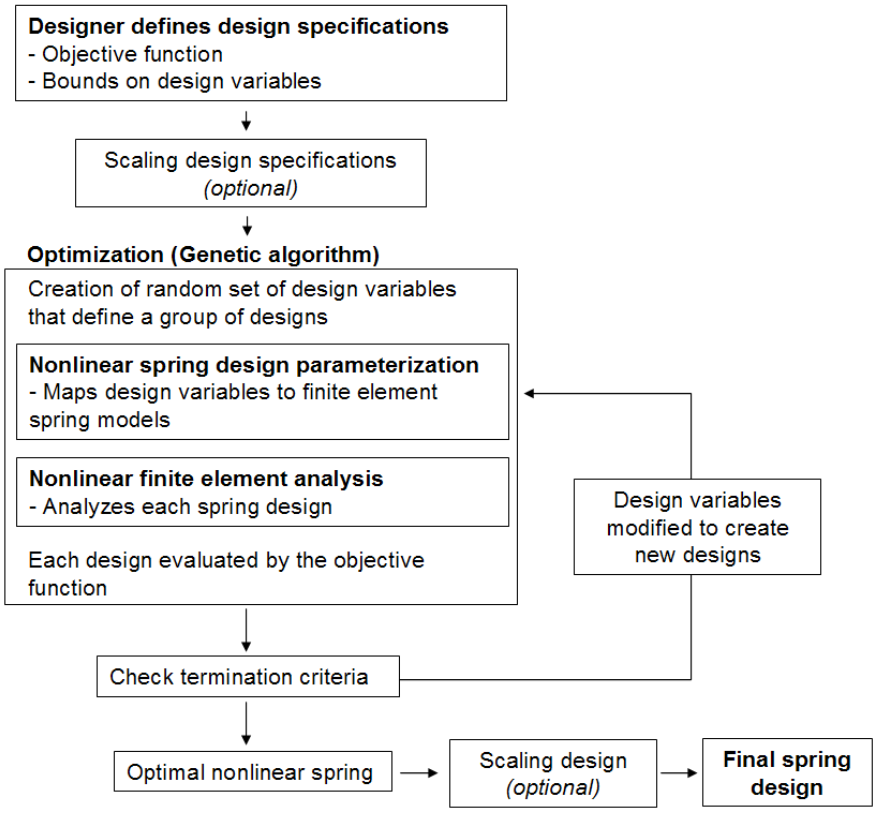

Figure 3-2: Synthesis methodology overview.

3.3 Achieving Nonlinear Responses

The success of the optimization greatly depends on the design parameterization, i.e. the numerical framework that maps design variables to finite element spring models. Since desirable designs have a nonlinear response, it is advantageous to employ a parameterization that is conducive to geometric nonlinearities. Given these considerations, this section introduces the basis for the design parameterization developed in this work.

The parameterization is based upon the simplest 1-D spring model, a cantilevered beam with a transverse load (Figure 3-3). This spring model is fully connected, since one end is grounded and the other end locates the input point, i.e. the point where the load is applied and the output displacement is measured. The beam's response is investigated under two different boundary constraints as shown in Figure 3-3. The beam has a 0.6mm by 4mm cross-section, a 50mm length, and is made of titanium (E=115GPa). When the input point is free (A), the beam is primarily loaded in bending and the resulting load-

displacement curve is fairly linear before it yields. By adding a constraint in the horizontal direction (B), the beam's load-displacement curve has greater nonlinearity as the beam transitions from a primarily bending mode to an axial mode. The constraint at the input induces significant nonlinearity to the design.

To generate spring designs that match *any* prescribed load-displacement function, consider a modification of the cantilever design which is only capable of a stiffening behavior. Instead of using a straight beam to connect the input and ground, a curvilinear beam (spline) adds nonlinear geometry to the model and provides a greater effective length. Longer beams enable greater strain energy absorption within a compact footprint and facilitate larger displacements and rotations, i.e. geometric nonlinearities, with lower stresses. Instead of limiting the design to one spline, the design space can be discretized into a network of splines (for greater strain energy absorption and additional design degrees of freedom) that connect the input and ground. At various ground points, pin joints can provide further rotations while minimizing bending stresses.

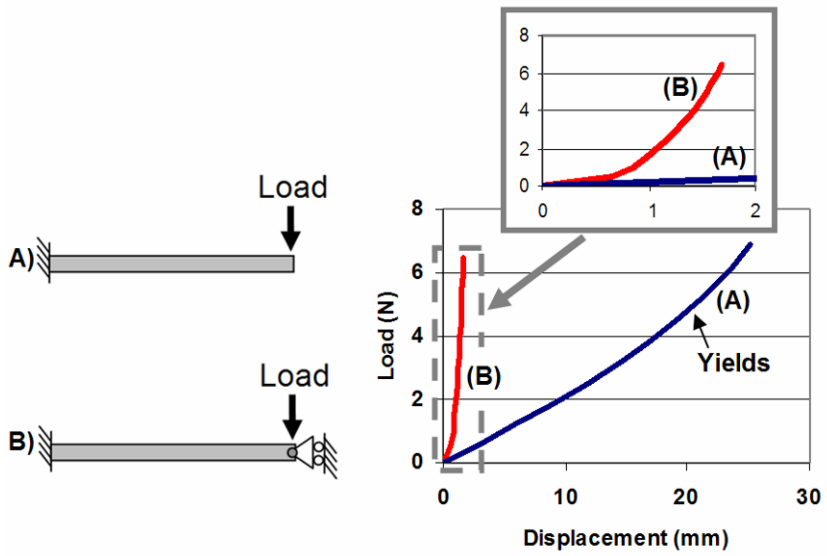

Figure 3-3: Two 1-D spring models (cantilever beams with transverse end loads) and their corresponding load-displacement functions. (A) Model with free end; (B) model with horizontally constrained end. The constraint on (B) induces greater nonlinearities in the response.

Because of these considerations, the design parameterization in this work encompasses a network of curved beams (splines). Figure 3-4 shows an example of a

typical spring generated from the parameterization. Key features of the parameterization include: (i) a branching network of compliant beams used for *topology synthesis*, rather than a ground structure or a homogenization based design parameterization, (ii) curved beams without sudden changes in cross-section, offering a more even stress distribution, and (iii) boundary conditions that impose both axial and bending loads on the compliant members and enable large rotations while minimizing bending stresses. The design parameterization is conducive to geometric nonlinearities, enabling individual beam segments to vary their effective stiffness as the spring deforms, i.e. large rotations and boundary conditions alter each beam segment's resultant forces, making it transition between an axial (stiff) member and a bending (flexible) member.

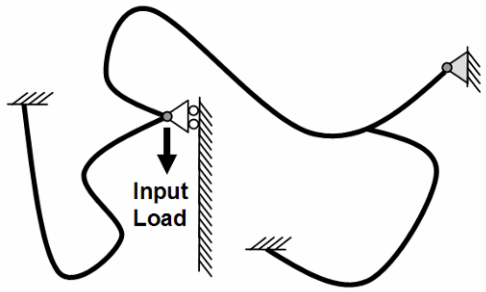

Figure 3-4: A typical spring design generated from the design parameterization used for this nonlinear spring synthesis methodology.

3.4 Design Specifications and Scope

With the nonlinear spring parameterization in mind, the designer defines the problem by the following parameters (most of which are illustrated in Figure 3-5): the prescribed load-displacement function, dimensions of the design space, location of the spring's input, boundary conditions at the input, specified area for the ground points, material property, element size constraints, and stress constraints. To induce axial loads that facilitate nonlinear responses, this work often employs a boundary constraint at the input (as shown in Figure 3-5), as opposed to leaving the input point free. Secondly, to give the optimizer full freedom within the design space, the designated area for ground points is often made equivalent to the entire design space.

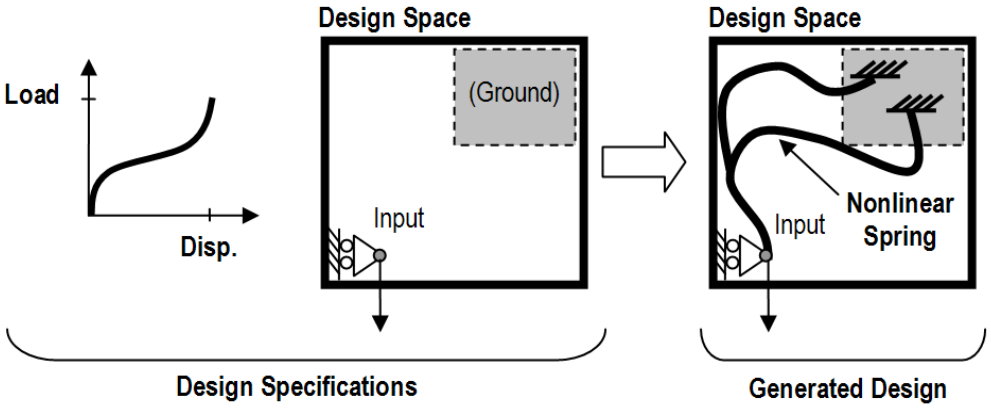

Figure 3-5: An illustration of the design problem, including design specifications and a potential solution.

For simplified and functional nonlinear spring designs, the scope of this work is limited to the following:

1) Planar spring designs: In two-dimensions, a nonlinear spring's primary mode of deformation is bending. Therefore, planar spring designs are simpler to physically analyze and interpret than spatial designs which also include torsional deformation. Planar springs also increase the potential for low-cost manufacturing options, e.g. stamping.
2) Elastic range: A spring always functions within the elastic range, avoiding undesireable plastic deformation (a material nonlinearity).
3) No buckling: Instabilities such as buckling are avoided to ensure smooth, un-abrupt behavior.

3.5 Nonlinear Analysis Issues

Each design generated within the optimization routine is evaluated using nonlinear analysis. Particular considerations have been made in choosing the appropriate planar beam element since the elements in these designs undergo large rotations, sometimes over 90º. In order to evaluate a design's post-buckling response, an arc-length method is employed for the nonlinear finite element analysis (FEA). It is desirable to solve a minimum number of equally distributed equilibrium points along the design's static equilibrium path. This best approximates the solution's load-displacement curve

and avoids unnecessary computations. To achieve this efficiency, the magnitude of the incremental arc-length is constrained to either a constant or maximum value. Using ordinary beam elements, this constraint on the arc-length sometimes causes non-convergence issues (when the arc-length is constrained to a constant value) or requires more equilibrium points to be solved (when the arc-length is constrained by a maximum value). These problems are circumvented with hybrid beam elements that are designed specifically for geometrically nonlinear problems especially those having slender elements and large elemental rotations (Hibbitt et al., 2004). Although hybrid beam elements are more costly than ordinary elements, they are recommended for this type of problem (Hibbitt et al., 2004) and several studies in this research have indicated that their sophistication maintains or decreases the overall convergence time. In particular, this work implements ABAQUS's modified Riks method for the analysis, and two-node hybrid beams (B21H) for the elements (Hibbitt et al., 2004).

CHAPTER 4

GENERALIZED SYNTHESIS METHODOLOGY

Figure 4-1 shows a nonlinear spring's load-displacement function. Three parameters describe a load-displacement function, (A) the shape function, (B) the load-range, and (C) the displacement-range. This chapter presents the generalized synthesis methodology for nonlinear springs and includes (i) a definition of the objective function for matching a prescribed load-displacement function, (ii) a detailed description of the design parameterization, and (iii) the formulation of an optimization scheme (a genetic algorithm (GA)) used to generate feasible designs.

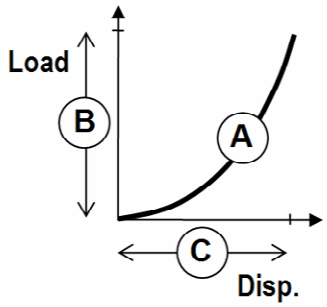

Figure 4-1: A nonlinear spring's load-displacement function with (A) shape function, (B) load-range, and (C) displacement-range.

To implement the methodology, the objective function, design parameterization, and GA were all coded in a Matlab program. The program pre- and post- processed each finite element model and executed ABAQUS, a finite element analysis (FEA) software, for each design's analysis. Specifically, an arc-length method (ABAQUS's modified Riks method) was employed for the nonlinear analysis to evaluate any post-buckling responses that occurred (Hibbitt et al., 2004). Much of the GA code was implemented from a GA toolbox developed at the University of Sheffield (Chipperfield et al., 2002).

4.1 Objective Function

The objective is to design a spring that generates a desired nonlinear load-displacement behavior (depicted as the solid curve in Figure 4-2) without buckling, yielding, or crossing over itself during deformation. The objective function in Equation (4-1) includes metrics to guide the optimizer toward desirable designs. The shape function error (SFE) evaluates a design's load-displacement shape function (A in Figure 4-1) relative to the prescribed shape function and also addresses stress considerations. The other terms represent constraint penalties for displacement (DP), buckling (BP), and crossover (XP) conditions specified by the designer.

.

$$Objective\ Function = min(SFE + DP + BP + XP) \tag{4-1}$$

4.1.1 Shape Function Error

The dashed curve in Figure 4-2 and Figure 4-3 represents the load-displacement function for a nonlinear spring design being evaluated within the optimization scheme. During the optimization, each spring design is subjected to the same applied load, equivalent to the specified load-range (B in Figure 4-1). To match the shape function, the goal is to find a spring with minimum error relative to the prescribed curve. Instead of evaluating the error over the entire load-displacement function, the function is matched at a few discrete points (Points A through D in Figure 4-2). The designer chooses target points to adequately define the curve's nonlinearity. Each of the target points is defined relative to the total load (F_{spring}) and total displacement (d_{spring}), where the F_{spring} is equivalent to either the applied load ($F_{applied}$ in Figure 4-2) or the limit load (F_{limit} in Figure 4-3). The limit load is the load corresponding to the maximum load within the spring's elastic range. To avoid yielding, designs are only evaluated over their elastic range as shown in Figure 4-3. Once optimized, designs can be scaled to meet the prescribed load-range (B in Figure 4-1) by increasing the out-of-plane thickness by a factor of ($F_{applied}$ /F_{limit}). This adjustment does not affect the spring's maximum stress or total displacement.

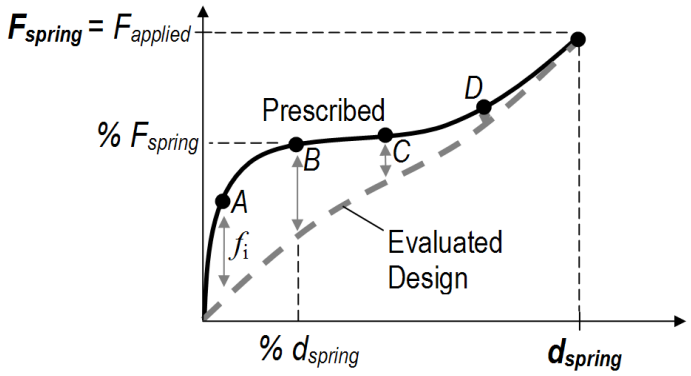

Figure 4-2: A prescribed load-displacement function with target points. The double arrows are the errors which determine the evaluated design's shape function error (SFE).

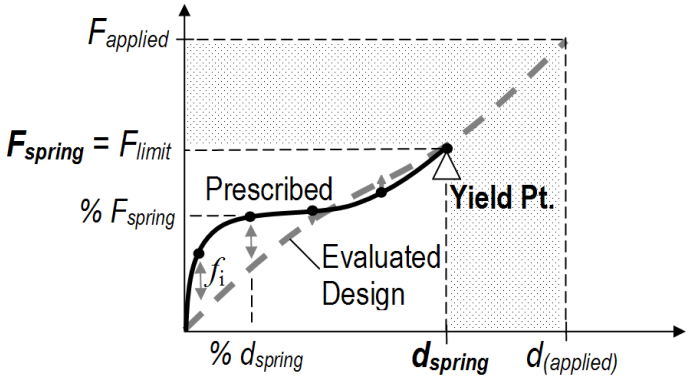

Figure 4-3: When a spring yields before reaching the applied load, the shape function error (SFE) is only evaluated over the spring's elastic range.

Equation (4-2) calculates the shape function error (SFE) by averaging the absolute values of the errors at the N number of target points (double arrows, f_i, in Figure 4-2 and Figure 4-3) and normalizing the errors by the total load (F_{spring}). By converting this value to a percentage, the SFE is an intuitive value for the designer, i.e. a percent error.

$$SFE = \frac{\frac{\sum_{i=1}^{N} |f_i|}{N}}{F_{spring}} * 100\% \tag{4-2}$$

4.1.2 Displacement Penalty

To generate designs that meet a desired total displacement (d_{spring}), a displacement penalty function and its weight factor (W_{Disp}) are included within the objective function. Depending on the displacement-range requirements for a particular spring problem, a designer can choose one of three displacement penalty (DP) formulations provided below. The first is the minimum displacement penalty (DP_{min}). It only penalizes designs when the total displacement is less than the minimum. The designer specifies a minimum displacement value (d_{min}) as a percentage of the spring's footprint, where percentages of 7.5% to 50% have been used in this research. When the total displacement of the spring is less than the minimum displacement, the design is penalized by the minimum displacement penalty (Equation (4-3)).

$$DP_{min} = \begin{cases} 0, & d_{spring} \geq d_{min} \\ \left(1 - \frac{d_{spring}}{d_{min}}\right) * 100\% * W_{Disp}, & d_{spring} < d_{min} \end{cases} \tag{4-3}$$

The last two penalties, the target displacement penalty (DP_{Target}) and the target-scaling displacement penalty ($DP_{Target\text{-}scaling}$), are employed when an exact displacement-range (d_{target}) is desired. The target displacement penalty (DP_{Target}) penalizes designs whose total displacement (d_{spring}) does not match the target displacement (d_{target}), as shown in Equation (4-4). Essentially every design is penalized unless its total displacement exactly matches the target displacement. Thus, the optimizer is continuously minimizing both the SFE and the target displacement penalty. Various studies showed that the inclusion of this penalty slowed the optimizer's ability to minimize the SFE. By reducing the DP_{Target}'s influence on the objective function, i.e. lowering its weight factor, $W_{Disp,}$ from 1 to 0.1, the SFE improved by an average of 35%. This improvement is significant; however, modifying the weight factor (W_{Disp}) does not reduce the number of designs that have a nonzero displacement penalty.

$$DP_{Target} = \left| \frac{d_{spring}}{d_{target}} - 1 \right| * 100\% * W_{Disp} \tag{4-4}$$

Therefore, an alternative penalty, the target-scaling displacement penalty ($DP_{Target\text{-}scaling}$) was formulated to accept (not penalize) a *range* of total displacements by employing scaling rules for nonlinear springs. Chapter 7 provides various scaling rules (equations) for nonlinear springs. This section briefly introduces scalability as it relates to matching a prescribed displacement-range. Using a W_{Disp} value of 0.1 and the target-scaling displacement penalty ($DP_{Target\text{-}scaling}$), parametric studies showed that the SFE was further improved by an average of 9% over the former penalty (DP_{Target}).

When scaling a spring design's footprint (overall size) its displacement-range scales proportionately. Therefore, a design having a good shape function (low SFE) but an undesirable displacement-range can be scaled to match a prescribed displacement-range. This scaling however affects stress. Stresses increase when scaling down and decrease when scaling up. Therefore, as long as a spring is designed within a *smaller* design space and its total displacement is *less than* the prescribed displacement-range, the design can be scaled up to meet exact displacement requirements while maintaining the stress constraints.

To implement scaling into the displacement penalty, the designer first sets a maximum scale factor, N_{up} (where $N_{up}>1$), for which to scale designs to a prescribed displacement-range. A larger N_{up} enables a greater range of acceptable displacements; however, it indirectly places greater stress constraints on the smaller-scaled problem. In this work, N_{up} is specified within a range of 1.2 to 2.0. Once N_{up} is chosen, the design space is scaled down by this amount. Figure 4-4: (a) An original design space (solid line) scaled down to a smaller design space (dashed line). The solution in (a) is then scaled up (b) to meet the prescribed displacement-range.Figure 4-4(a) illustrates how an initial square design space of size L is scaled to L_{small} by a factor of $1/N_{up}$. To scale a design's footprint and maintain the design's shape function, a design's load-range (F_{spring}) and cross-section dimensions (out-of-plane thickness: h_{out_plane} and in-plane thickness: h_{in_plane}) must also scale according to the relationships in Equation (4-5). Therefore, to determine the design specifications for the smaller-scaled problem, the load and cross-section specifications must also scale by $1/N_{up.}$ The design examples in the next chapter will provide further details for setting up a target-scaling problem.

$$
\begin{aligned}
F_{spring}^{(large)} &= F_{spring}^{(small)} * N_{up} \\
h_{out\_plane}^{(large)} &= h_{out\_plane}^{(small)} * N_{up}^{3/4} \\
h_{in\_plane}^{(large)} &= h_{in\_plane}^{(small)} * N_{up}^{3/4}
\end{aligned}
\tag{4-5}
$$

At this point, the setup of the smaller-scaled problem is complete and designs can be generated within the new design space. Figure 4-4(a) shows a resulting spring design within the smaller design space. This design can scale by N_{up} and still fit within the original design space. As shown by the dotted curve in Figure 4-5, any spring design with a total displacement (d_{spring}) between the *scaled* target displacement (d_{target}/N_{up}) and the target displacement (d_{target}) can scale to match the prescribed target displacement (solid curve). This amount of scaling (N_{disp}) equals (d_{target}/d_{spring}), where $N_{disp} \leq N_{up}$. Figure 4-4(b) illustrates the final "scaled-up" spring design. Again, Equation (4-5) must be followed whenever scaling a spring's footprint. Figure 4-5 shows the load-displacement function of the final design versus the smaller scaled design. The total displacement of the final design matches the prescribed displacement-range (d_{target}). The total load of the spring also matches the prescribed load-range (F_{target}). Often times, after the scaling up the footprint, the total load does not match the prescribed load. In these cases, the out-of-plane thickness must be scaled by N_{load} (F_{target}/F_{spring}) in order to meet the prescribed load-range.

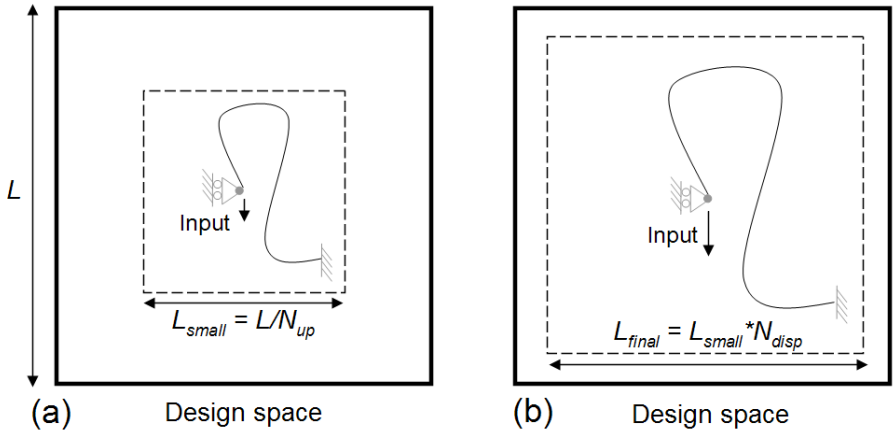

Figure 4-4: (a) An original design space (solid line) scaled down to a smaller design space (dashed line). The solution in (a) is then scaled up (b) to meet the prescribed displacement-range.

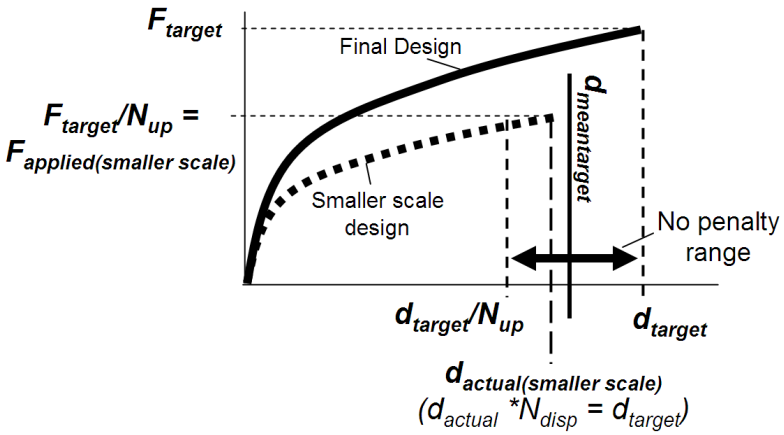

Figure 4-5: A plot illustrating how scaling (i) enables a smaller scaled problem (dotted curve) to have a range of acceptable displacements and (ii) converts the smaller scaled design into a final design (solid line) that meets the required load-range (F_{target}) and displacement-range (d_{target}).

To formulate the target-scaling displacement penalty ($DP_{Target\text{-}scaling}$), a spring design's total displacement (d_{spring}) is compared to the mean target displacement represented in Equation (4-6) and noted as a vertical line in Figure 4-5. The difference between these two values is calculated as an error (ε) in Equation (4-7). Since a range of displacements is acceptable, the allowable error (ε_{allow}) is determined by Equation (4-8). Finally, if the error is greater than the allowable error, a penalty value that is proportional to the error is assigned to the design as the $DP_{Target\text{-}scaling}$ value (Equation (4-9)).

$$d_{meantarget} = \left(\frac{d_{target}}{N_{up}} + d_{target} \right) / 2 \tag{4-6}$$

$$\varepsilon = \left| \frac{d_{spring} - d_{meantarget}}{d_{meantarget}} \right| * 100\% \tag{4-7}$$

$$\varepsilon_{allow} = \frac{d_{target} - d_{meantarget}}{d_{meantarget}} * 100\% \tag{4-8}$$

$$DP_{Target\text{-}scaling} = \begin{cases} 0, & \varepsilon \le \varepsilon_{allow} \\ \varepsilon * W_{Disp}, & \varepsilon > \varepsilon_{allow} \end{cases} \quad (4\text{-}9)$$

When design space specifications permit, scaling is a powerful tool to meet *exact* displacement-ranges. Otherwise, the target displacement penalty (DP_{Target}) is a suitable alternative, as long as an appropriate W_{Disp} is chosen. As a side note, when employing the target-scaling displacement penalty ($DP_{Target\text{-}scaling}$), if the lower bound on a design's in-plane thickness is determined by a manufacturing constraint, scaling the design's in-plane thickness may make the final design's in-plane thickness fall lower than the original specified range. For this case, it is recommended to use a lower N_{up}, such as 1.2, and not scale down the in-plane thickness range for the smaller-scaled problem.

4.1.3 Buckling Penalty

Buckling is avoided by employing a buckling penalty function and its weight factor (W_{Buck}) within the objective function. Negative stiffness, represented as a negative slope in Figure 4-6, signifies instabilities in the structure which usually leads to abrupt, snap-through buckling. Using finite element analysis, buckling is also signified by negative eigenvalues in a design's system matrix. Therefore, two buckling penalties have been employed. When the minimum slope ($slope_{min}$) of the load-displacement function is negative, the design is penalized by the slope buckling penalty (BP_{slope}, Equation (4-10)). The greater the slope's magnitude, the more the design will be penalized. In some cases, spring designs have passed the slope buckling penalty but still had negative eigenvalues in the system matrix. One way this can occur is when an insufficient resolution of equilibrium points is solved along a design's load-displacement function, making negative slopes undetectable. Therefore, the negative eigenvalue buckling penalty (BP_{-EV}, Equation (4-11)) adds an extra check to the slope buckling penalty, BP_{slope}. If a design is found to be free of negative slopes, it checks whether the system matrix has any negative eigenvalues. If it does, the design is penalized by a value, W_{-EV}, where W_{-EV} =10 in this work. Otherwise, the design is not penalized for buckling. If using the slope buckling penalty (BP_{slope}), it is recommended to double check final designs for negative eigenvalues.

$$BP_{slope} = \begin{cases} 0, & slope_{min} \geq 0 \\ -slope_{min} * W_{Buck}, & slope_{min} < 0 \end{cases} \quad (4\text{-}10)$$

$$BP_{-EV} = \begin{cases} 0, & slope_{min} \geq 0 \;\&\; No\text{-}EV \\ W_{-EV}, & slope_{min} \geq 0 \;\&\; -EV \\ -slope_{min} * W_{Buck}, & slope_{min} < 0 \end{cases} \quad (4\text{-}11)$$

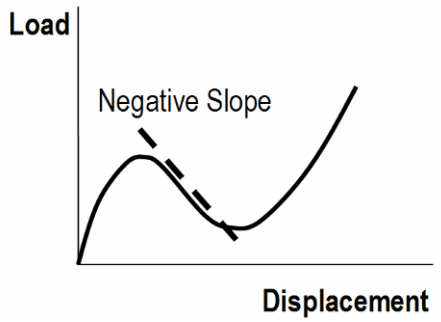

Figure 4-6: A negative slope in the load-displacement function indicates instability.

4.1.4 Crossover Penalty

Finally, designs that overlap or crossover themselves during deformation are more difficult to manufacture. By including the deformed-crossover penalty (XP), designs are checked for spline crossover in their final deformed configuration, rather than during their entire range of motion. This condition has proven to identify almost all cases of crossover. If a crossover is found, the design is penalized by XP, a finite value specified by the user. In this work, a value of 5 was chosen for XP.

4.2 Design Parameterization

The design space is parameterized by variables depicting a design's topology, shape, and size. These design variables determine boundary conditions, the presence or absence of elements, element interconnectivity, element locations, and the elements' in-plane thickness.

4.2.1 Topology

The design space is discretized using nine splines. Figure 4-7 shows the parameterized topology located within the design space. The circle in the middle is the input point. The black filled circles are the end points which are either fixed or pinned to ground. The input, end points, and gray points are all control points and connect to one another as indicated in the figure. Cubic B-spline functions are fit to each set of five control points, where one set of points is boxed in Figure 4-7. As illustrated in Figure 4-8, the five control points determine a spline's control polygon, dictating the shape of the spline. Overall, the topology is a network of splines connecting the input and end points.

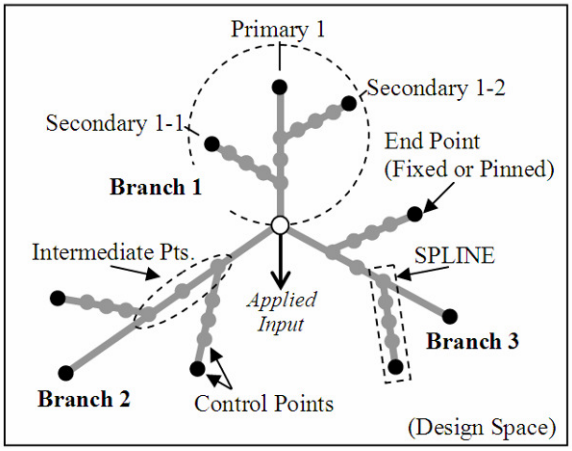

Figure 4-7: The topology is parameterized using a branching network of nine compliant beams (splines) that connect the input to various ground points.

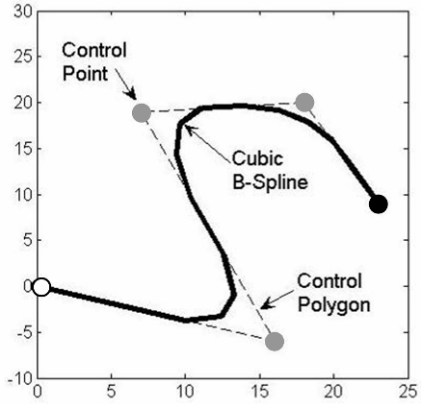

Figure 4-8: Each spline is represented as a cubic B-spline whose shape is controlled with 5 control points.

The topology has three branches of splines; Branch 1 is circled in Figure 4-7. Each branch has one *primary spline* and two *secondary splines*. Primary splines are the only splines that are connected to the input point. The secondary splines are connected to the primary splines near the intermediate control points shown in the figure. For each topology, certain splines are present within the design while others are hidden or absent. Secondary splines can only be present if the primary splines that they are connected to are also present. Different topologies are generated by controlling a combination of the following: (i) the boundary conditions at the end points (either fixed or pinned to ground), (ii) the connection locations between the primary and secondary splines, and (iii) the splines' status as either present (on) or absent (off) in the design.

4.2.2 Shape

Figure 4-8 shows how the control points give shape to each spline. As the control points move around the design space, the splines are continuously adjusted to the new control polygons. Therefore, relocation of a control point modifies the spline geometry and hence the spring's stiffness.

4.2.3 Elimination of Loops, Cusps, and Overlapping

To generate topologies that simplify manufacturing, single-plane spring designs are created by avoiding (i) splines from looping over themselves and (ii) overlapping between separate splines. Also, cusps are avoided in order to minimize stress concentrations. Instead of actively prohibiting each spline from looping over itself, the optimizer first determines each spline's configuration and then removes loops as needed. Figure 4-9 shows how a spline's control points are reordered when a spline's control polygon crossover itself, thereby eliminating loops.

A spline is simultaneously checked for cusps by calculating the three angle sizes within a spline's control polygon, as pointed out in Figure 4-9. Small angles indicate the presence of cusps within a spline. If any angle is less than a minimum angle set by the user, the control points are reordered until a design is free of loops and cusps. A minimum angle of 15° is recommended. In some cases, control points are arranged such

that cusps are unavoidable. To address this, cusps are permitted within a spline after K number of unsuccessful reordering attempts; K equaled five in this work.

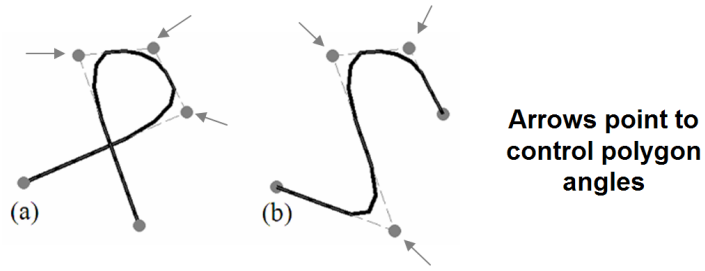

Figure 4-9: (a) A looped B-spline; (b) a reordering of the control points to avoid loops.

Once loops are absent from the design, the overlapping of multiple splines is eliminated by turning off one of every two splines that overlap. Instead of checking every combination of two splines, a sequence of checks (3 steps) was developed to minimize the number of overlap checks required to produce a planar design. The sequence is based upon the hierarchy between the primary and secondary splines, where a secondary spline can only exist when its primary spline is "on". The first step checks for overlapping between the primary splines. With the remaining splines, the second step checks for overlapping within individual branches. If two or more branches remain, the third step checks for overlapping among the remaining splines, otherwise this step is omitted. Using this approach, each spline is able to use the entire design space (versus actively constraining a spline's placement and geometry to avoid other splines).

4.2.4 Size

Finally, the size of each spline is defined by its in-plane thickness, which is a continuous variable that assumes a value between the lower and upper bounds specified by the designer. The size variations also affect the spring's overall stiffness.

4.3 Genetic Algorithm

A genetic algorithm is used to generate multiple initial designs, which are refined each subsequent design iteration until a termination requirement is met. Genetic

algorithms (GAs) are heuristic optimization schemes modeled after nature's biological selection and adaptation process (Goldberg, 1989; Eiben and Smith, 2003). Compared to gradient based algorithms, GAs more thoroughly explore a design space by beginning with multiple initial designs. Compliant mechanism solution spaces are noisy and non-convex, making GAs suitable candidates for optimization (Lu, 2004). GAs typically require more computational time than gradient based methods; however, they have worked well in compliant mechanism design problems (Lu and Kota, 2006). A GA is employed to take advantage of this research's discrete design parameterization for nonlinear springs.

A GA begins by randomly creating an initial population of designs. Each design is coded in a numerical string called a chromosome. Over the course of iterations (generations), the population is refined through selection, cross-over, and mutation processes. The following subsections will elaborate on each of these parts relative to nonlinear spring synthesis.

4.3.1 Chromosomes

A nonlinear spring design is represented by a chromosome which is a string of variables depicting its topology, size, and shape. These variables indicate the following: a spline being present or absent in a design, degrees of freedom of the spline end points, locations for spline branching, the coordinates of spline control points, and the splines' in-plane thickness. As listed in Table 4-1, the chromosome has a total of 114 variables. Each of the nine splines is represented by a set of variables that determine its topology and shape. The final variable, number 114, defines the uniform in-plane thicknesses of the splines. The bounds on this variable are defined by user input. The out-of-plane element thickness is not contained within the chromosome because it is a constant defined by the user prior to the optimization.

Table 4-1: Variable locations within the chromosome.

Variable #'s	Variables Defining:	Variable Types
1-11	Primary spline 1 (P1)	Topology and Shape
12-24	Secondary spline 1 (P1-S1)	
25-37	***Secondary spline 2 (P1-S2)***	
38-49	Primary spline 2 (P2)	
50-62	Secondary spline 1 (P2-S1)	
63-75	Secondary spline 2 (P2-S2)	
76-87	Primary spline 3 (P3)	
88-100	Secondary spline 1 (P3-S1)	
101-113	Secondary spline 2 (P3-S2)	
114	Uniform in-plane thickness	Size

Taking a closer look at the variables, Table 4-2 and Figure 4-10 delineate the variables representing the second secondary spline in Branch 1, (P1-S2). The spline's variables are located in the chromosome as variable numbers 25-37 out of 114 as seen in Table 4-1. In this work, a constraint was always placed on the X and Y degrees of freedom for each of the spline's endpoints, ensuring that each endpoint was either fixed or pinned to ground. Since two variables of each of the nine splines were held constant, only ninety-six variables were used, (96 = 114 – (9 splines) x (2 variables)).

Table 4-2: Variables 25-37 of the secondary spline (P1-S2).

#	Variable Description	Variable Values	Variable Types
25	Spline on or off	On or Off	Topology
26	*X- DOF constraint (Pt. E)*	*Always On*	
27	*Y- DOF constraint (Pt. E)*	*Always On*	
28	Z-rot. DOF constraint (Pt.E)	On or Off	
29	Pt. A connected to Pt. 2,3,or 4	Pt. 2, 3, or 4	
30	Pt. B's X-coordinate	Locations within the user defined design space	Shape
31	Pt. B's Y-coordinate		
32	Pt. C's X-coordinate		
33	Pt. C's Y-coordinate		
34	Pt. D's X-coordinate		
35	Pt. D's Y-coordinate		
36	Pt. E's X-coordinate		
37	Pt. E's Y-coordinate		

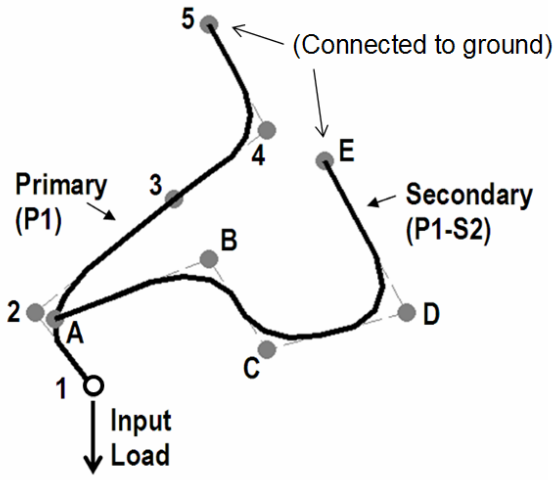

Figure 4-10: Splines P1 and P1-S2.

4.3.2 Initialization

The genetic algorithm begins by creating a population of random designs. For the examples in this paper, the number of individuals in the population was specified as equal to the number of variables, 96. When an initial design is generated, variable values within the chromosome are created at random, defining the design's topology, shape, and size. Before a design is evaluated, it is converted to a planar design by the loop and overlap checks. Cusps are also minimized.

4.3.3 Crossover and Mutation

After all the designs are evaluated, a new population is created from the old population and placed in the next generation. Each generation employs an elitist strategy by placing the best 10% of the designs into the next generation. The remaining designs are created through a selection, crossover, and mutation process. The selection process chooses designs for the next generation by biasing towards designs with low (good) objective function values. The crossover process selects two designs and swaps variables between the chromosomes, thus creating new designs. Finally, the mutation process modifies variable values within a chromosome. The population is updated each generation. Upon termination, the best design is retrieved.

In the examples in the next chapter, crossover occurred between *groups* of variables. The groups were specified as variables defining individual splines. The probability of crossover was set to 70% (the default for the GA toolbox (Chipperfield et al., 2002)). For mutation, all variables were enabled to mutate at a rate of one variable per branch (approximately a 3% mutation rate).

4.4 Local Search

A genetic algorithm works well in locating a *region* containing a local or global optimum; however, it can be inefficient in finding an *exact* optimum. Therefore, it is beneficial to employ a local search algorithm to further refine a design obtained from a genetic algorithm. Pattern search algorithms (a.k.a. direct search algorithms) do not require gradient information from the objective function and include a local search algorithm referred to as polling. Polling begins with an initial design, which is represented as a point in the solution space. For each iteration, a mesh is created around the point in order generate a set of neighboring designs to evaluate. The algorithm then evaluates (polls) neighboring designs looking for a design with a lower objective function value than the current point. If a better design is found, the algorithm re-centers itself at the new point, and begins a new iteration.

For this work, a Matlab-based pattern search algorithm, NOMADm (Abramson, 2006), was implemented to apply the polling search method. The initial design was always the final design retrieved from the genetic algorithm. By only optimizing the size and shape variables, the design was refined while maintaining the original topology.

CHAPTER 5

DESIGN EXAMPLES

Three nonlinear spring example problems are presented to demonstrate the performance of the generalized synthesis methodology introduced in the previous chapter. Each problem specifies a unique shape function (J-shaped, S-shaped, or constant-force) and a prescribed load- and displacement-range. Table 5-1 delineates the remaining design specifications for the three nonlinear springs. Notice that the size of the design space, material, maximum stresses, and cross-section dimensions all vary from one spring to another. Figure 5-1 represents the general design space for each example problem. The input point is located in the center and constrained in the horizontal direction. For each spring's objective function, the displacement penalty weight is 0.1, and the buckling penalty weight is 1000. The presence of slight negative slopes in the load-displacement functions, sometimes on the order of 10^{-3}, calls for the large buckling penalty weight. As mentioned in the previous chapter, each example problem employed a genetic algorithm with a population of 96 individuals, a crossover rate of 70%, and a mutation rate of approximately 3%.

As a final example, a large displacement *linear* spring is presented to illustrate the methodology's ability to control a constant stiffness over a large range of motion. The problem specifications are given later in the chapter.

Table 5-1: Design specifications for three nonlinear spring examples.

Shape-function	J-curve	S-curve	Constant-force
Load-range	10N	75N	150N
Displacement-range	20mm	80mm	150mm
N_{up} (Scaling)	1.2	1.5	2.0
Square design space size (L)	100mm (10cm)	500mm (0.5m)	1000mm (1m)
Material modulus (material)	115MPa (Titanium)	115MPa (Titanium)	70MPa (Aluminum)
Maximum stress (safety factor)	830MPa (1)	415MPa (2)	275MPa (1)
Out-of-plane thickness	4mm	20mm	60mm
In-plane thickness	0.4-0.7mm	1-3mm	2-5mm

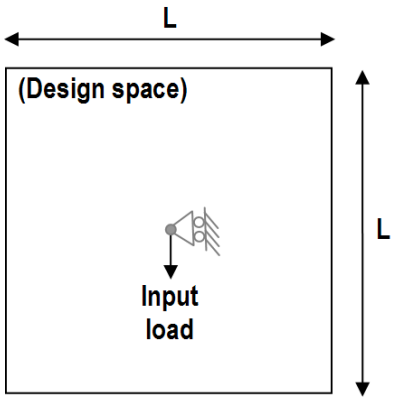

Figure 5-1: Design space specifications.

5.1 J-curve Spring

Although designers usually employ linear elastic materials, such as steel, aluminum, and plastics, biologist Steven Vogel (1998) notes that most biological materials have a nonlinear stiffness. Specifically, many biological tissues, such as skin, cartilage, and ligaments, have upwardly curved stiffness plots resembling a J-shape. Therefore, this example synthesizes a spring made of linear material but having a J-shaped load-displacement function due to its topology, shape, size, and boundary conditions.

Chapter 3 showed how a cantilever beam whose endpoint is constrained in the horizontal direction produces a J-shaped load-displacement curve. A straight cantilever beam may not always fit within a desired design space. Therefore, this example illustrates a new spring design that produces a *prescribed* J-shaped shape function (Figure 5-2) and

fits within a specified area. The chosen shape function was based on the mechanical response of myocardium, a heart tissue (Humphrey et al., 1990). Three target points (A, B, and C) were chosen to define the J-curve, with A at (25% Displacement, 4% Load), B at (50% Displacement, 17% Load), and C at (75% Displacement, 48% Load). Additionally, the prescribed load- and displacement-ranges are 10N and 20mm, respectively. The remainder of the design specifications include: Design space size: 100mm, Material: titanium (E=115GPa), Maximum stress: 830MPa (yield), Out-of-plane thickness: 4mm, and In-plane thickness range: 0.4-0.7mm.

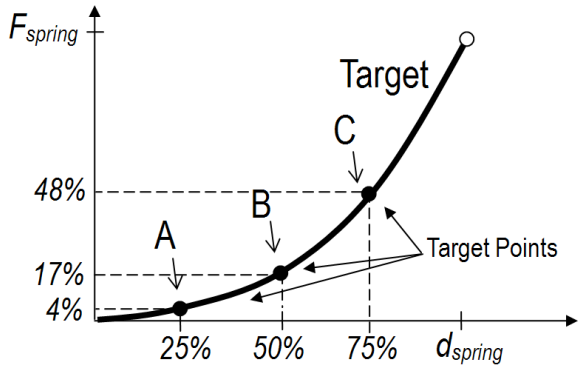

Figure 5-2: The prescribed J-curve shape function with three target points (A, B, and C).

$$Objective\ Function = min(SFE + DP_{Target\text{-}scaling} + BP_{Slope}) \tag{5-1}$$

The objective function formulation (Equation (4-2)) includes the target-scaling displacement penalty and the slope bulking penalty. For the displacement penalty, N_{up} is 1.2. Table 5-2 compares the problem design specifications to those calculated for the smaller-scaled problem. The in-plane thickness range is left unmodified assuming that the original specification of 0.4mm is a *minimum* manufacturing constraint.

Design optimization was executed for the smaller-scaled problem via a genetic algorithm. First, an initial population of 96 designs (chromosomes) was randomly created. Each chromosome contained information about a design's topology, shape, and size. The genetic algorithm then began to evaluate and create refined designs based on the objective function values. After 40 generations, the final design was retrieved for the smaller-scaled problem. Its load-displacement function (dashed line in Figure 5-3) confirms its J-curve behavior, which closely follows the prescribed target values. The

shape function error is 0.69% with neither the displacement nor buckling constraints violated. The design's system matrix is also free of negative eigenvalues, reconfirming stability over the spring's range of motion.

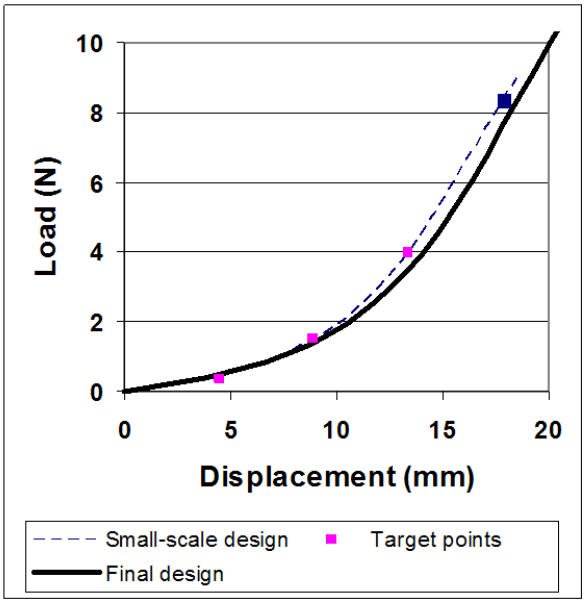

Figure 5-3: Load-displacement function for the generated J-curve design (small-scale) and its final scaled design. The final design meets the shape function (J-curve), load-range (10N), and displacement-range (20mm) specifications.

At this point, the load- and displacement-ranges of 8.33N and 17.8mm do not match the prescribed ranges of 10N and 20mm, respectively. However, the satisfied displacement penalty indicates that scaling can eliminate this discrepancy. The resulting design parameters for the smaller-scales problem are given in Table 5-3 column (a). To meet the target displacement-range of 20mm, the design's footprint was scaled by 1.12 (N_{disp} = 20mm/17.8mm), modifying the design parameter/variable values to those shown in Table 5-3 column (b). Since the scaled total load is 9.33N and the prescribed load is 10N, the spring's out-of-plane thickness was scaled by a factor of 1.07 (N_{load} = 10N/9.33N) as shown in Table 5-3 column (c). This column contains the final design's parameters and variables and the resulting displacement-range and stress determined by FEA.

The final design's load-displacement function is compared to the smaller-scaled function in Figure 5-3. Under a 10N load, the J-curve spring displaces 20.1mm. The 0.5% error is likely due to rounding either the N_{disp} or N_{load} values while scaling. The design's maximum von Mises stress is 720MPa, well below titanium's yield point and slightly lower than the stresses in the small-scaled spring. Figure 5-4 shows the final design in both un-deformed and deformed configuration. The topology has one spline with a fixed endpoint. Interestingly, no well-defined curves exist in the design since three of the five spline control points ended up near one another and formed a corner-like geometry. Although the stress constraint is already met by this design, local search results in the next section reveal that stresses are indeed lowered by smoothing the "corner" in the final design.

Figure 5-5 illustrates a contour plot of the von Mises stress at the beams' edges. The distributed compliance of the elements enables the spring to achieve a displacement-range that is 37% of its largest footprint dimension. Using an Intel Pentium 4-CPU 2.26GHz (512MB RAM), the evaluation time for this example was 10.7 hours (real time).

Table 5-2: Design specifications for J-curve spring.

Design parameters	Original	Smaller-scaled
Load-range	10N	8.33N (10N/ N_{up})
Design space (square)	100mm	83.3mm (100mm/ N_{up})
Out-of-plane thickness	4mm	3.49mm (4mm/ $N_{up}^{0.75}$)
In-plane thickness	0.4 – 0.7mm	0.4 – 0.7mm

Table 5-3: Optimization and scaling results for J-curve spring. Bold values indicate the parameters that were scaled.

Design parameters, values, and responses	Smaller-scaled design	Disp. scaling (N_{disp} = 1.12)	Load scaling (N_{load}= 1.07) FINAL DESIGN
	(a)	(b)	(c)
Total load	8.33N	**9.33N**	**10N**
Total displacement	17.8mm (FEA)	-	20.1mm (FEA)
Out-of-plane thickness	3.49mm	**3.80mm**	**4.07mm**
In-plane thickness	0.47	**0.51**	0.51
Footprint	36.0 x 48.0mm	**40.3 x 53.8mm**	40.3 x 53.8mm
Stress (Max = 830MPa)	723MPa (FEA)	-	720MPa (FEA)

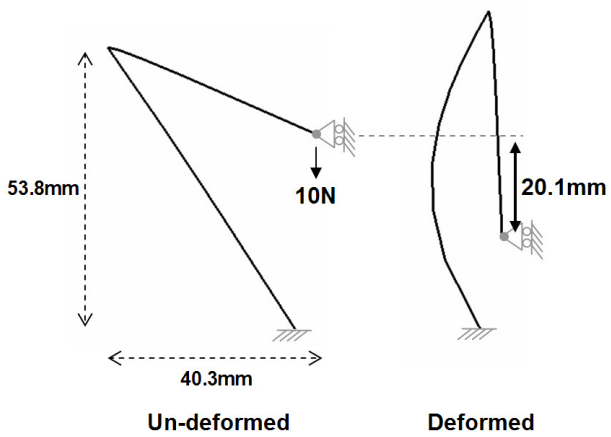

Figure 5-4: Final J-curve design in its un-deformed and deformed configurations.

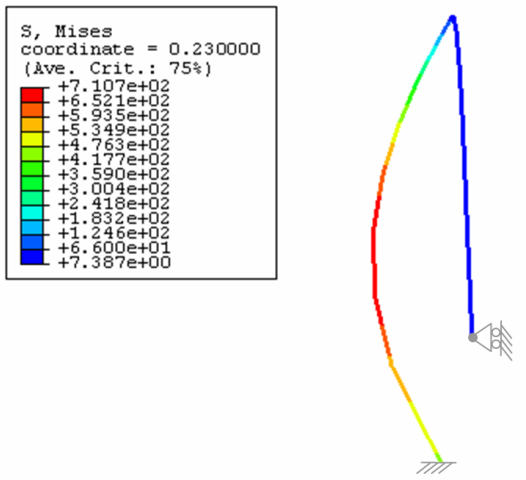

Figure 5-5: FEA stress contours for J-curve spring.

5.1.1 Refining the Final Design with a Local Search

The final J-curve spring design met the specified design requirements, therefore no further design refinement is necessary. This section however employs the J-curve design to illustrate a design's refinement using a local search method. Here, the goal is to increase the stress distribution within the design found in the previous section.

To measure stress distribution along a spring's length, a study was first conducted to compare four stress distribution metrics, including a design's mean, median, and maximum stress and also the coefficient of variation (c_v) of stress, which is a direct measure of distribution (c_v = standard deviation / mean). A particular spring design was

optimized for each of the four objectives: minimize the (i) maximum stress, (ii) mean stress, (iii) median stress, and (iv) variance of stress. Twenty-three variables were simultaneously optimized. Fifteen of the variables represented the in-plane thicknesses of individual elements (size variables), while the remainder of the variables represented the spline's control point locations (shape variables). Each shape variable was given a local rectangular area in which to roam, thus maintaining the general shape of the initial design.

Table 5-4 shows the results of this study. The underlined quantities indicate the best value in each row. The coefficient of variance is clearly a comprehensive metric. By minimizing the variance, it found a design with the lowest maximum, mean, standard deviation, variance, and stress range (= max stress – min stress). However, it also takes a least three times as long to find an optimal solution compared to the other metrics. If computational time is an issue, the maximum stress is the next best metric to optimize. It performs better than the mean and median and takes one-third the time of the variance metric.

Table 5-4: Comparison of four different objective functions used to optimize stress distribution. The stress results for the resulting respective designs are listed in each column. The best values per row are underlined.

Objective function MINIMIZE:	(1) Maximum stress	(2) Mean stress	(3) Median stress	(4) Variance of stress
Maximum (MPa)	654	739	825	**598**
Mean (MPa)	366	324	360	**319**
Median (MPa)	300	213	**174**	356
Stress range (MPa)	625	692	819	**549**
Std. Dev. (MPa)	231	246	288	**124**
Variance	0.63	0.76	0.80	**0.39**
Hours	8.6	4.7	5.0	26.4

To further distribute the stresses within the J-curve design, the coefficient of variance was included in the objective function used during the local search (Equation (5-2)). Note the asterisk after the SFE. Since the SFE of the final design was already acceptable at 0.69%, no further minimization was necessary. In fact, a slightly larger SFE would still provide a good J-curve response. Therefore, the SFE formulation was modified such that designs with an SFE below 0.90% were given an SFE* value of zero.

To enable an allowable range of acceptable displacements, the local optimization was conducted on the smaller-scaled design using the same N_{up} value, 1.2. Twenty-three variables were simultaneously optimized. Fifteen of the variables represented the in-plane thicknesses of individual elements (size variables), while the remaining variables represented the spline's control point locations (shape variables). Again, each shape variable was given a local rectangular area in which to roam, thus maintaining the general shape of the initial design.

Table 5-5 compares the stress variance and maximum stress of the initial design (optimized by only a GA) and the refined design (optimized by both a GA and polling search method). The variance was lowered from 1.02 to 0.49 and indirectly the maximum stress was lowered from 723MPa to 611MPa. Figure 5-6 shows the refined design and its stress distribution in the final deformed configuration. Using an Intel Pentium 4-CPU 2.26GHz (512MB RAM), the local search optimization took 7.5 hours (real time). This refined design can now be scaled to match the prescribed load- and displacement-ranges.

$$Objective\ Function = min(SFE^{*} + DP_{Target\text{-}scaling} + BP_{Slope} + c_v) \tag{5-2}$$

Table 5-5: The stress variance and maximum stress of the initial design (optimized by only a GA), the refined design (optimized by both a GA and polling search method), and the refined design with a constant in-plane thickness.

Design	Optimization	Variance	Maximum Stress (MPa)
Original small-scaled	GA	1.02	723
Refined	GA + Local search (size and shape variables)	0.49	611
Refined shape with constant in-plane thickness of original design	n/a	0.56	607

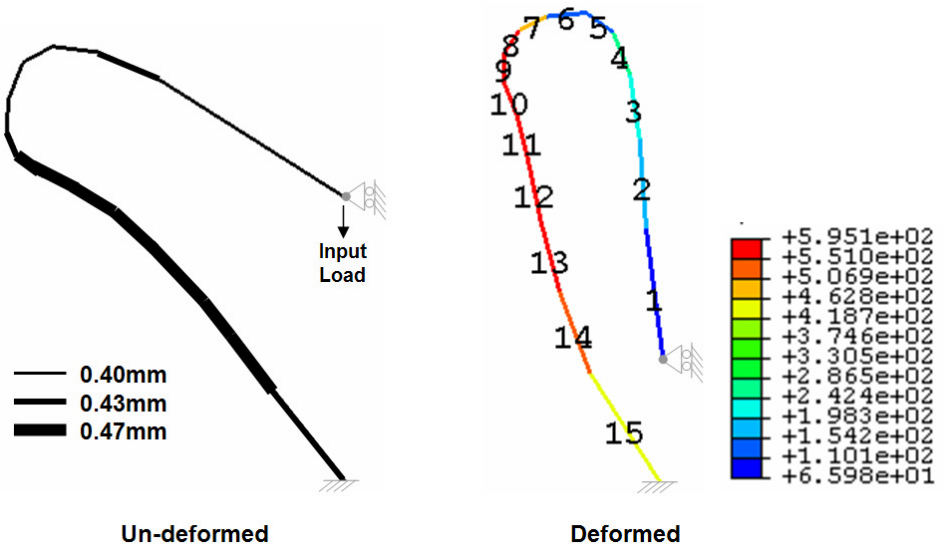

Figure 5-6: The J-curve design optimized for stress distribution by a local search. The un-deformed configuration shows the relative element sizes. The deformed configuration illustrates the FEA stress contour with the elements numbered.

By reducing the number of design variables in the local search, the computational time can be decreased. Fifteen of the twenty-three variables in this example represented the individual in-plane thicknesses of the elements (size variables). To determine the influence of the size variables on the final design, the refined design was analyzed in its new shape (represented as the un-deformed shape in Figure 5-6) but with constant thickness, where $h_{in\text{-}plane}$ equaled the thickness found from the GA, 0.47mm. Table 5-5 shows that the stress variance within the design increases from 0.49 to 0.56; however, the maximum stress is lower than both the previous design iterations. Note that the original design had a sharp corner and that the refined shape has a gradual curve. Therefore, refining a design by only its shape variables can significantly distribute the stresses and indirectly lower the maximum stress. Furthermore, by not optimizing the elemental thicknesses, these designs have a uniform thickness making them easier to manufacture.

5.2 S-curve Spring

The goal is to design a nonlinear spring that most closely matches the arbitrary nonlinear load-displacement function shown in Figure 5-7. This function is labeled an "S"-curve since it has an inflection point (near pt. B); the other two nonlinear spring examples do not have this characteristic. This function defines a spring whose stiffness is

relatively stiff during the initial loading, but then becomes more compliant and then stiffens as the load increases. Three target points (A, B, and C) were chosen to define an arbitrary J-curve, with A at (25% Displacement, 58% Load), B at (50% Displacement, 66% Load), and C at (79% Displacement, 75% Load). Additionally, the prescribed load- and displacement-ranges are 75N and 80mm, respectively. The remainder of the design specifications include: Design space size: 500mm, Material: titanium (E=115GPa), Maximum stress: 415MPa (safety factor of 2), Out-of-plane thickness: 20mm, and In-plane thickness range: 1-3mm.

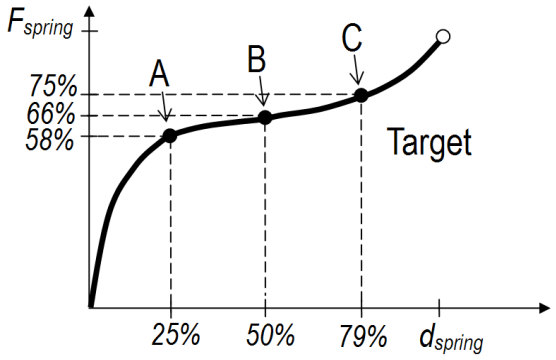

Figure 5-7: The prescribed S-curve shape function with three target points (A, B, and C).

$$Objective\ Function = min(SFE + DP_{Target\text{-}scaling} + BP_{\text{-}EV} + XP) \tag{5-3}$$

The objective function formulation (Equation (5-3)) includes the target-scaling displacement penalty, the negative eigenvalue bulking penalty, and the deformed-crossover penalty. For the displacement penalty, N_{up} is 1.5. Table 5-6 compares the problem design specifications to those calculated for the smaller-scaled problem.

Design optimization was executed for the smaller-scaled problem via a genetic algorithm. Once again, an initial population of 96 designs (chromosomes) was created. The genetic algorithm was terminated once the SFE was below 5% (22 generations). (SFE cut-off values are addressed in the final section of this chapter.) A subsequent local search was performed on the resulting topology's shape variables (control points) and the *uniform* in-plane thickness variable. The smaller-scaled design's load-displacement function (dashed line in Figure 5-8(a and b)) confirms its S-curve behavior, which closely

follows the prescribed target values. The shape function error is 0.74% with neither the displacement, buckling, nor crossover constraints violated.

At this point, the load- and displacement-ranges of 8.72N and 77.0mm do not match the prescribed ranges of 75N and 80mm, respectively. However, the satisfied displacement penalty indicates that scaling can eliminate this discrepancy. The resulting design parameters for the small scale problem are given in Table 5-7 column (a). To meet the target displacement-range of 80mm, the design's footprint was scaled by 1.04 (N_{disp} = 80mm/77.0mm), modifying the design parameter/variable values to those shown in Table 5-7 column (b). Since the scaled total load is 9.07N and the prescribed load is 75N, the spring's out-of-plane thickness was scaled by a factor of 8.27 (N_{load} = 75N/9.07N) as shown in Table 5-7 column (c). This column contains the final design's parameters and variables and the resulting displacement-range and stress determined by FEA.

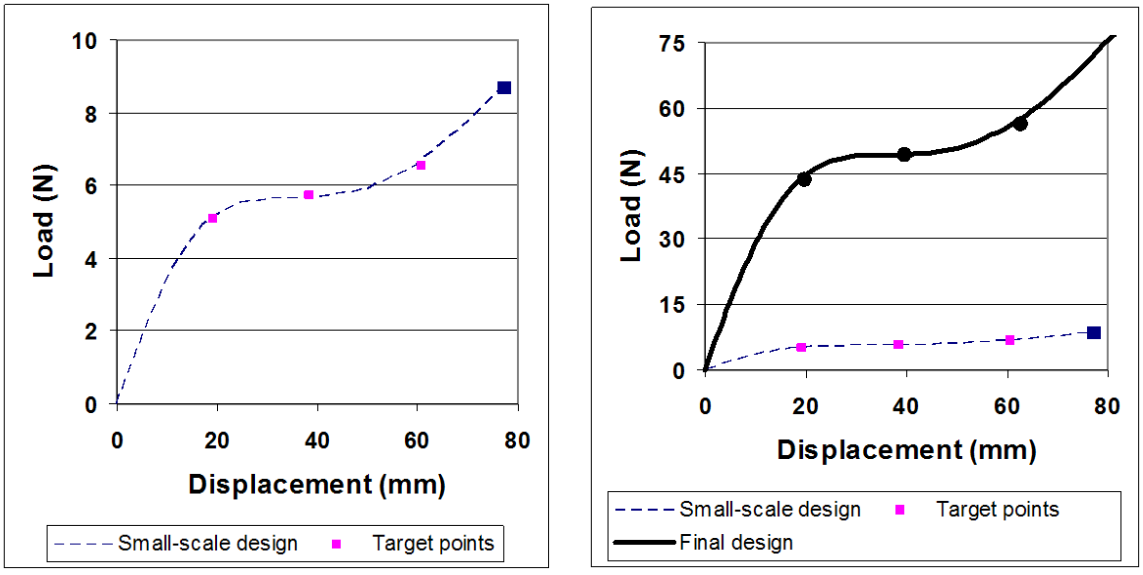

(a) (b)

Figure 5-8: Load-displacement functions for the generated S-curve design (small-scale) and its final scaled design. The final design meets the shape function (S-curve), load-range (75N), and displacement-range (80mm) specifications.

The final design's load-displacement function is compared to the smaller-scaled function in Figure 5-8(b). Under a 75N load, the S-curve spring displaces 80.2mm. The

design's maximum von Mises stress is 410MPa, meeting a safety factor of 2. Figure 5-9 shows the final design in both un-deformed and deformed configuration. The topology has one spline with a fixed endpoint.

Figure 5-10 illustrates a contour plot of the von Mises stress at the beams' edges. The distributed compliance of the elements enables the spring to achieve a displacement-range that is 33% of its largest footprint dimension. Using an Intel Pentium 4-CPU 2.26GHz (512MB RAM), the evaluation time for this example was 10.5 hours (real time), where the GA lasted 8.3 hours and the local search 2.2 hours.

Table 5-6: Design specifications for S-curve spring.

Design parameters	Original	Smaller-scaled
Load-range	75N	50N (75N/ N_{up})
Design space (square)	500mm	333mm (500mm/ N_{up})
Out-of-plane thickness	20mm	14.76mm (20mm/ $N_{up}^{0.75}$)
In-plane thickness	1-3mm	0.74– 2.21mm (1-3mm/ $N_{up}^{0.75}$)

Table 5-7: Optimization and scaling results for S-curve spring. Bold values indicate the parameters that were scaled.

Design parameters, variables, and responses	Smaller-scaled design	Disp. scaling (N_{disp} = 1.04)	Load scaling (N_{load}= 8.27) FINAL DESIGN
	(a)	(b)	(c)
Total load	8.72N (LimitLoad)	**9.07N**	**75N**
Total displacement	77.0mm (FEA)	-	80.2mm (FEA)
Out-of-plane thickness	14.76mm	**15.2mm**	**125.7mm**
In-plane thickness	1.25mm	**1.29mm**	1.29mm
Footprint	237.1 x 108.1mm	**246.3 x 112.3mm**	246.3 x 112.3mm
Stress (Max = 415MPa)	415MPa (FEA)	-	410MPa (FEA)

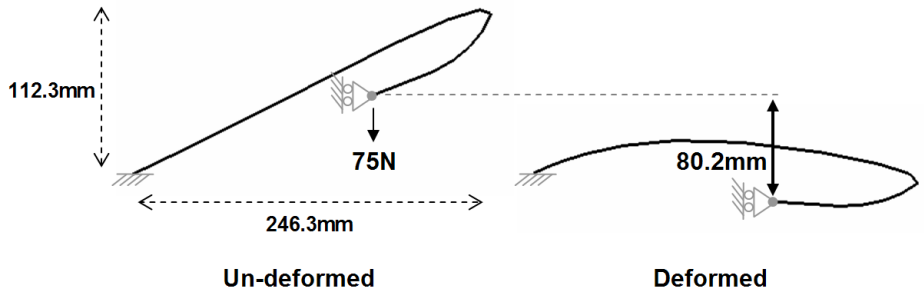

Figure 5-9: Final S-curve design in its un-deformed and deformed configurations.

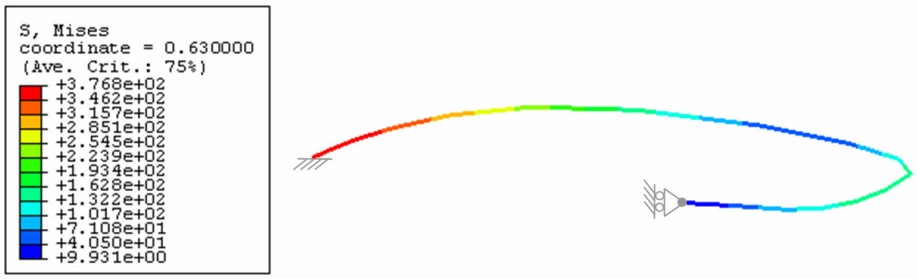

Figure 5-10: FEA stress contours for S-curve spring.

5.3 Constant-force Spring

The goal is to design a constant-force spring that most closely matches the nonlinear load-displacement function shown in Figure 5-11. This function defines a spring whose stiffness is relatively high during the initial loading, but then whose load remains constant. Three target points (A, B, and C) were chosen to define an arbitrary constant-force spring, with A at (25% Displacement, 100% Load), B at (50% Displacement, 100% Load), and C at (75% Displacement, 100% Load). The remaining design specifications include: Design space size: 1000mm, Material: aluminum (E=70GPa), Maximum stress: 275MPa (yield), Out-of-plane thickness: 60mm, and In-plane thickness range: 2-5mm.

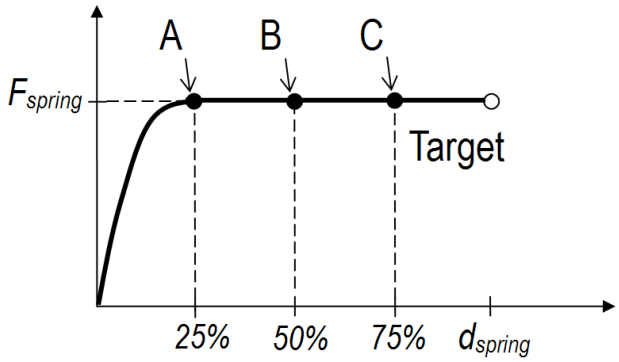

Figure 5-11: The prescribed constant-force shape function with three target points (A, B, and C).

$$Objective\ Function = min(SFE + DP_{Target\text{-}scaling} + BP_{\text{-}EV} + XP) \quad (5\text{-}4)$$

The objective function formulation (Equation (5-4)) includes the target-scaling displacement penalty, the negative eigenvalue bulking penalty, and the deformed-crossover penalty. For the displacement penalty, N_{up} is 2.0. Table 5-8 compares the problem design specifications to those calculated for the smaller-scaled problem.

Design optimization was executed for the smaller-scaled problem via a genetic algorithm. Again, an initial population of 96 designs (chromosomes) was created. After 60 generations, the best design was retrieved. Its load-displacement function (dashed line in Figure 5-12) confirms its constant-force behavior, which closely follows the prescribed target values. The shape function error is 3.35% with neither the displacement, buckling, nor crossover constraints violated.

At this point, the load- and displacement-ranges of 37.33N and 94.3mm do not match the prescribed ranges of 150N and 150mm, respectively. The satisfied displacement penalty indicates that scaling can eliminate this discrepancy. The resulting design parameters for the small scale problem are given in Table 5-9 column (a). To meet the target displacement-range of 150mm, the design's footprint was scaled by 1.59 (N_{disp} = 150mm/94.3mm), modifying the design parameter/variable values as shown in Table 5-9 column (b). Since the scaled total load is 59.36N and the prescribed load is 150N, the spring's out-of-plane thickness was scaled by a factor of 2.53 (N_{load} = 150N/59.36N) as shown in Table 5-9 column (c). This column contains the final design's parameters and variables and the resulting displacement-range and stress determined by FEA.

The final design's load-displacement function is compared to the smaller-scaled function in Figure 5-12. Under a 150N load, the constant-force spring displaces 160mm (10mm more than prescribed), while under a 149N load (just 1N lower) the spring displaces 144mm (6mm less than prescribed). This sensitivity is a result of the constant-force characteristic of the nonlinear spring (a small load-displacement slope), making it more difficult to match an exact displacement-range. The design's maximum von Mises stress is 255MPa, which is below the yield point. Figure 5-13 shows the final design in both un-deformed and deformed configuration. The topology has two splines with one end fixed and the other pinned to ground.

Figure 5-14 illustrates a contour plot of the von Mises stress at the beams' edges. The distributed compliance of the elements enables the spring to achieve a displacement-range that is 20% of its largest footprint dimension. Using an Intel Pentium 4-CPU 2.26GHz (512MB RAM), the evaluation time for this example was 22.4 hours (real time). This time may have been reduced had a local search been employed earlier in the GA.

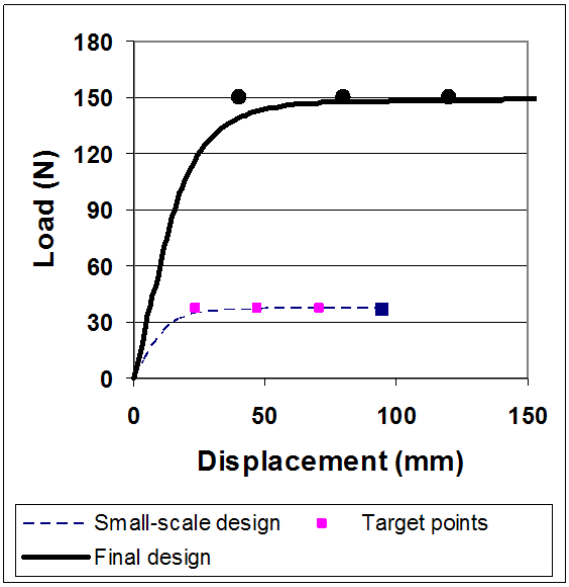

Figure 5-12: Load-displacement functions for the generated constant-force design (small-scale) and its final scaled design. The final design meets the shape function (constant-force), load-range (150N), and displacement-range (150mm) specifications.

Table 5-8: Design specifications for constant-force spring.

Design parameters	Original	Smaller-scaled
Load-range	150N	75N (150N/ N_{up})
Design space (square)	150mm	75mm (150mm/ N_{up})
Out-of-plane thickness	60mm	35.68mm (60mm/ $N_{up}^{0.75}$)
In-plane thickness	2-5mm	1.19– 2.97mm (2-5mm/ $N_{up}^{0.75}$)

Table 5-9: Optimization and scaling results for constant-force spring. Bold values indicate the parameters that were scaled.

Design parameters, variables, and responses	Smaller-scaled design	Disp. scaling (N_{disp} = 1.59)	Load scaling (N_{load}= 2.53) FINAL DESIGN
Total load	37.33N (Limit load)	**59.36N**	**150N**
Total displacement	94.3mm (FEA)	-	160mm (FEA)
Out-of-plane thickness	35.68mm	**50.52mm**	**127.7mm**
In-plane thickness	1.62mm	**2.29mm**	2.29mm
Footprint	430.8 x 462.8mm	**684.9 x 735.8mm**	684.9 x 735.8mm
Stress (Max = 275MPa)	275MPa (FEA)	-	255MPa (FEA)

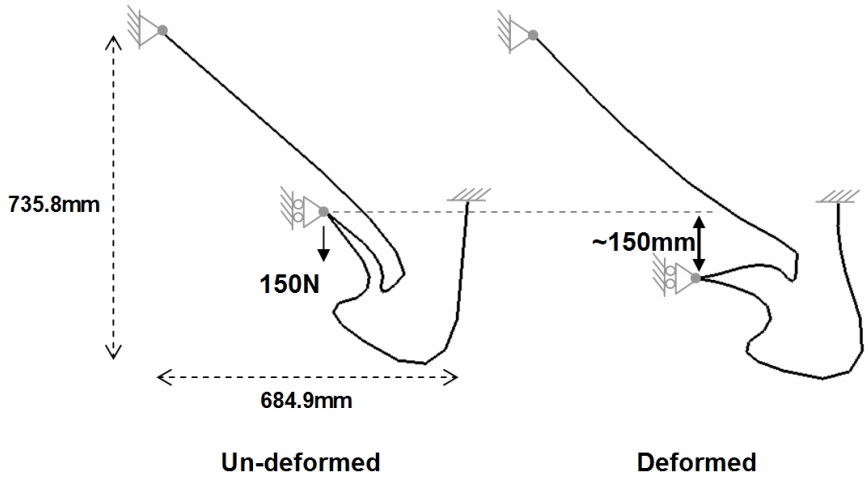

Figure 5-13: Final constant-force design in its un-deformed and deformed configurations.

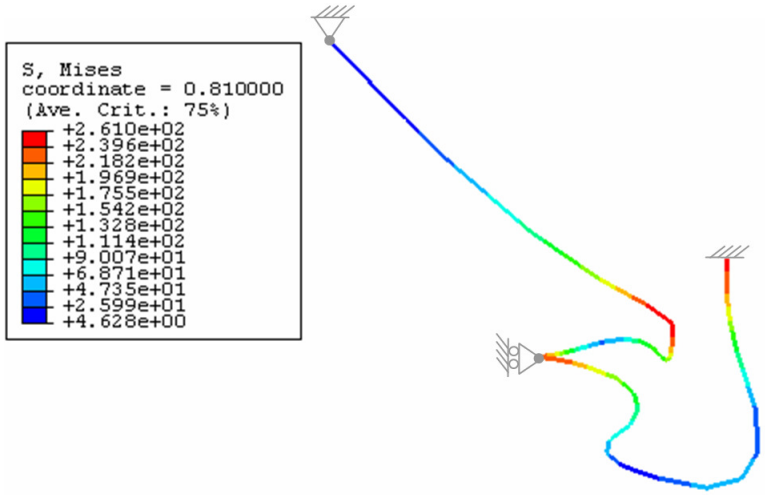

Figure 5-14: FEA stress contours for constant-force spring.

The resulting design utilized much of the specified design space. For a more compact design, the constant-force spring was trimmed as shown in Figure 5-15. The

shape function error increases from 3.35% to 8.79%; however, a subsequent local search on the spring's shape variables can potentially decrease the error. In general, if a spring's compactness is a desirable characteristic, then this should be reflected in the specified design space before the genetic algorithm is executed.

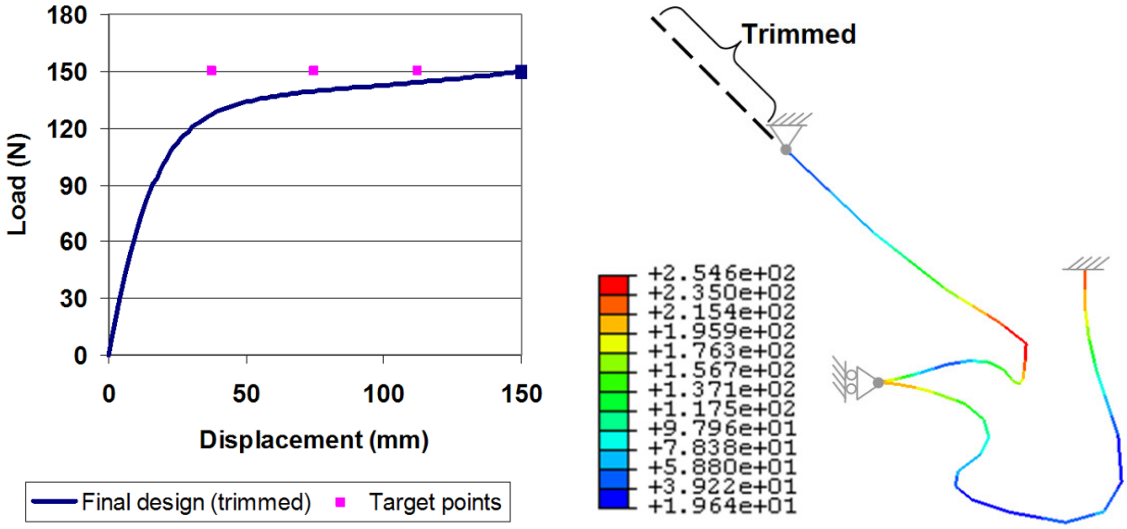

(a) (b)

Figure 5-15: Trimmed constant-force design, (a) load-displacement function (SFE = 8.79%), (b) FEA stress plot.

5.4 Large Displacement Linear Spring

For the final example, a linear spring is prescribed using nine equally spaced target points. This example illustrates that the methodology is able to control a constant stiffness over a large range of motion. The design specifications include: Design space size: 90mm, Material: titanium (E=115GPa), Maximum stress: 830MPa (yield), Out-of-plane thickness: 4mm, and In-plane thickness range: 0.4 to 0.7mm. Since the spring has a constant stiffness, it is not necessary to prescribe an exact displacement-range. The objective function formulation (Equation (5-5)) includes the minimum displacement penalty and the slope bulking penalty. The minimum displacement percentage was 50% of the spring's footprint, the displacement penalty weight was 1, and the buckling penalty weight was 1000.

$$Objective\ Function = min(SFE + DP_{min} + BP_{slope}) \tag{5-5}$$

The resulting spring design was the best design after 20 generations using a genetic algorithm. The spring's resulting displacement is 48.9mm, 78% of the spring's footprint. Figure 5-16 and Figure 5-17 show the resulting spring design and load-displacement function, respectively. The shape function error is 0.15% with neither the buckling nor displacement constraints violated. The design's system matrix is also free of negative eigenvalues, reconfirming stability over the spring's range of motion. Like the J-curve and S-curve designs, this topology has one primary spline whose end is fixed to ground. The spline is sized with a 0.60mm in-plane thickness, and the footprint of the spring is 62.9mm by 54.7mm. The maximum von Mises stress is 825MPa, which is below the yield stress. Figure 5-18 illustrates the stress distribution. Using an Intel Pentium 4-CPU 2.26GHz (512MB RAM), the evaluation time for this example was 5.2 hours (real time).

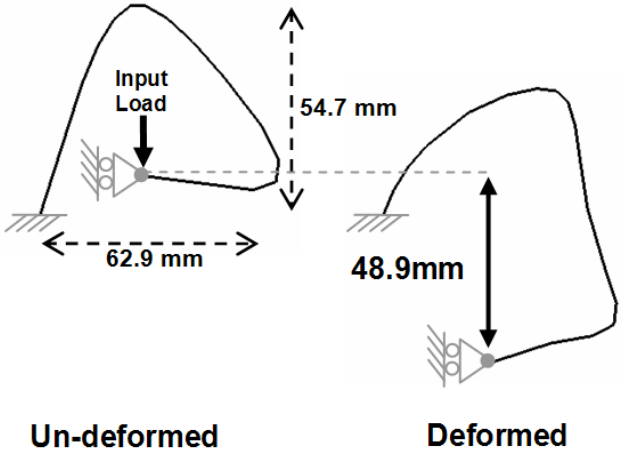

Figure 5-16: Final linear spring design in its un-deformed and deformed configurations.

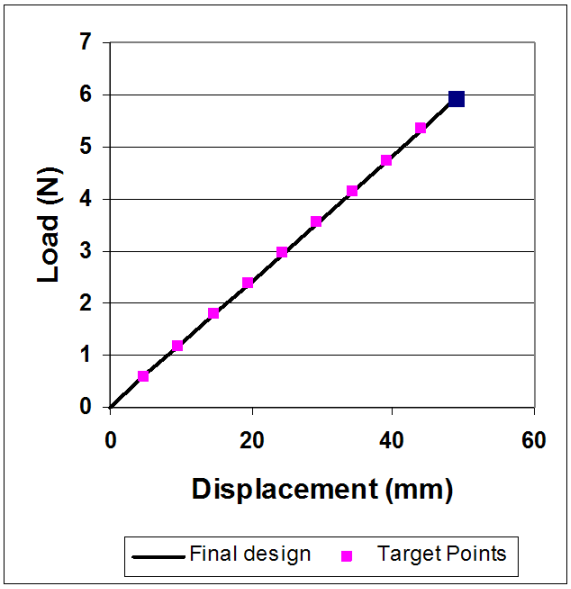

Figure 5-17: Load-displacement function for the resulting large displacement linear spring with nine target points.

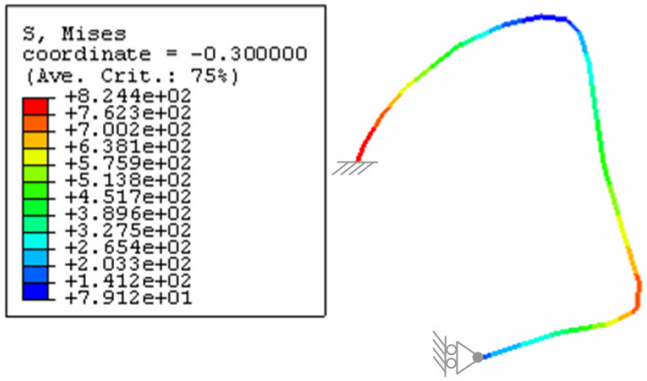

Figure 5-18: FEA stress contours for large-displacement linear spring.

5.5 Discussion

The discrete design parameterization of a network of curved beams, optimized by a GA and analyzed by a commercial FEA software, has enabled the generation of nonlinear spring designs that match prescribed load-displacement functions. The distributed compliance within the designs enabled large displacements (20 - 78% of footprint) within specified stress constraints. The specified displacement-ranges in the nonlinear spring examples limited the springs to a certain range of motion. The next chapter includes a J-curve, S-curve, and constant-force spring each optimized with a minimum displacement penalty and having relative displacements of 39%, 126%, and

47%, respectively. The loop and overlap checks combined with the uniform size variable generates planar spring designs of constant thickness which are easier to manufacture. Applicable primary manufacturing methods include stamping (when the out-of-plane thickness is small), forming/bending strips of material (when the out-of-plane thickness is large), injection molding, and die casting.

The discrete design parameterization enables the generalized synthesis methodology to be implemented into any nonlinear FEA routine whether contained within commercial software or coded separately. In particular, an arc-length method is recommended in order to evaluate any post-buckling (instability) responses that arise. Using commercial software, ABAQUS, and an Intel Pentium 4-CPU 2.26GHz (512MB RAM), the evaluation time for each example was between 5-23 hours (real time). Using an Intel Core 2-CPU 2.39GHz (2GB RAM), the evaluation time is reduced by approximately one-third.

If the designer knows when the GA is near a local or global optimum, the designer can terminate the GA and execute a local search for faster convergence to the optimum. For the S-curve spring example, the GA was terminated when the constraint penalties were satisfied and the SFE value was lower than 5%. Determining an SFE cut-off point is subjective and greatly depends on the prescribed load-displacement function. For example, during this research, none of the generated constant-force spring designs have ever achieved an SFE lower than 2%, because its first target point (A in Figure 5-11) has been unachievable thus far. Therefore, a cut-off point at 2% or lower would be ineffective for that set of target points. However, if the designer chooses too high of a cut-off point, the GA will terminate too soon and the local search will only find a suboptimal design. Therefore, the value of the cut-off point is left to the designer's intuition.

CHAPTER 6

PHYSICAL INTERPRETATION

This chapter investigates spring designs generated from the nonlinear spring synthesis methodology to offer a physical interpretation of (i) how springs generate nonlinear responses and (ii) which spline shapes are most beneficial for a given spring type. Four different spring designs are employed for this study, including a J-curve, S-curve, constant-force, and linear spring. Each spring investigated in this chapter has only one spline in its topology to avoid confusion in assessing the contributions of multiple splines.

6.1 Generating Nonlinear Responses

The design parameterization for nonlinear springs is conducive to geometric nonlinearities, enabling individual beam segments to vary their effective stiffness as the spring deforms, i.e. large rotations and boundary conditions alter each beam segment's resultant forces, making it transition between an axial (stiff) member and a bending (flexible) member. Using the four spring designs in Figure 6-1, the axial and bending tradeoffs within each spring are investigated. The stresses within an FEA spring model are used to observe the resultant loads along a spring's length. Figure 6-2 shows how each element's axial stress is represented by the stress located at its neutral axis. The bending stress is represented by the difference in the element's maximum positive stress and its axial stress. Thus, each element's bending stress is positive (tension), while its axial stress is either positive (tension) or negative (compression).

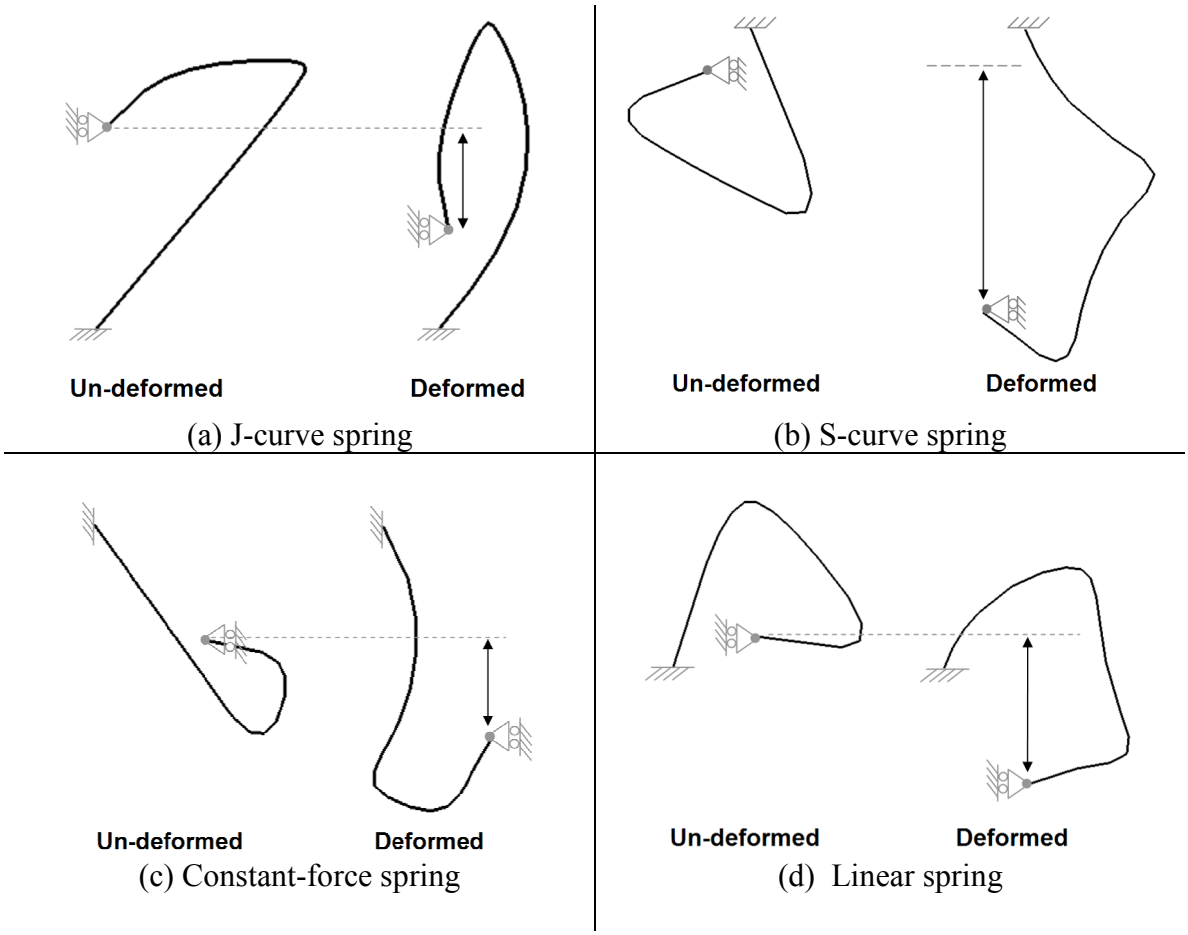

Figure 6-1: Four nonlinear springs each with one spline in its topology.

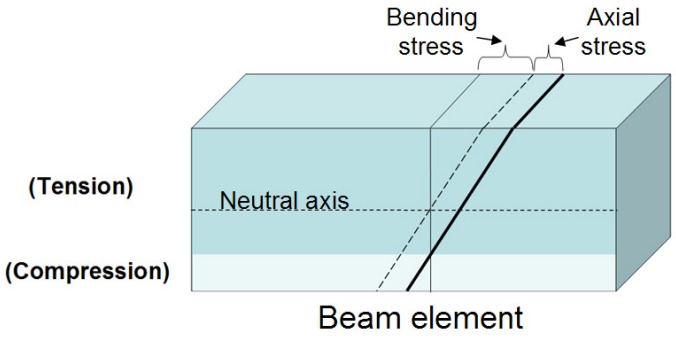

Figure 6-2: Determining bending and axial stresses within a beam element.

6.1.1 Studies on Four Different Spring Types

In this study, each spring's load-displacement shape function is compared to its average (i) bending stress and (ii) axial stress profile to determine whether any correlations exist over the spring's range of motion. Table 6-1 show plots for each of the

four nonlinear springs investigated in this study. The spring's displacement is plotted along the x-axis in each plot. In each row, the y-axis plots either the load, average bending stress, average axial stress, or the average *absolute value* of the axial stress. The final value is considered since an axial (stiff) member should contribute stiffness to a spring whether in tension or compression; therefore, the sign of the axial stress is disregarded.

Table 6-1: Comparison of average stresses for four different springs.

	J-curve	S-curve	Constant-force	Linear
Load (N)	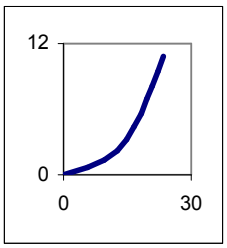	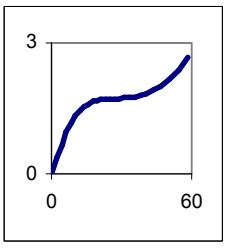	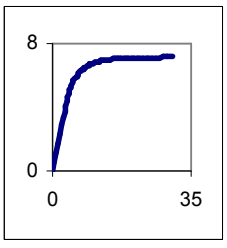	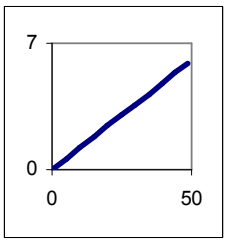
Average Bending Stress (MPa)	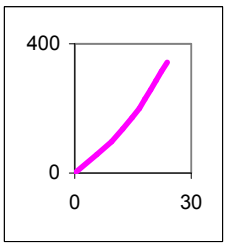	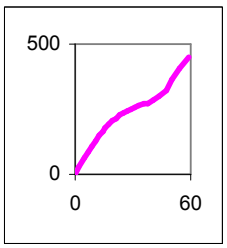	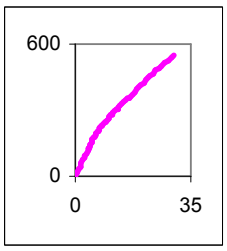	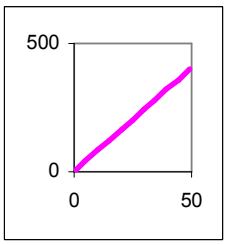
Average Axial Stress (MPa)	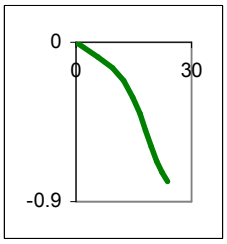	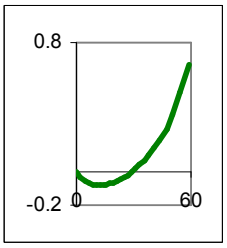	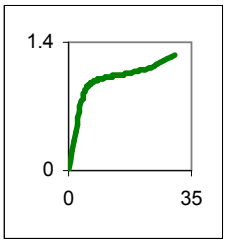	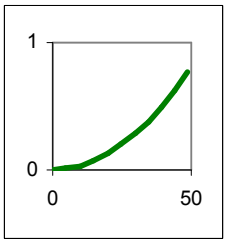
Average |Axial Stress| (MPa)	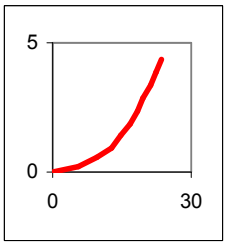	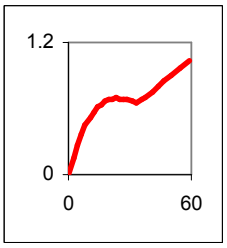	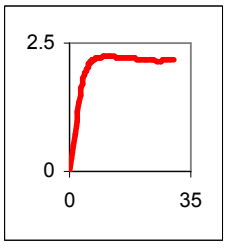	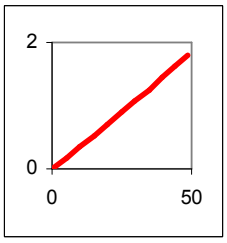
	Displacement (mm)			

Comparing the shape functions in the top row (load) to the second row (bending stress), there is a very little correlation with the J-curve and S-curve springs, none with

the constant-force spring, and a strong correlation with the linear spring, since both plots are linear. Comparing the shape functions in the top row (load) to the third row (axial stress), there is a slight inverse correlation with the J-curve spring and a stronger correlation with the constant-force spring. The linear spring actually has a nonlinear axial stress plot. Interestingly, the inflection point in the S-curve spring's load-displacement function occurs about mid-range in the displacement, near the same displacement that the average axial stress switches from negative to positive. Next, comparing the shape functions in the top row (load) to the fourth row (absolute value of axial stress), all four springs have a strong correlation, supporting the hypothesis an axial (stiff) member contributes stiffness to a spring whether in tension or compression. In general, the axial stresses have a stronger correlation than the bending stresses. Interestingly though, the magnitude of the axial stresses is much lower than the bending stresses (on an order of 10^{-2}). The resulting dominance of the axial stress is likely due to a beam's axial stiffness being significantly higher than its bending stiffness.

To observe the fluctuations of axial and bending stresses within an *individual* element, Figure 6-3 to Figure 6-6 plot the stresses within each element over the spring's range of motion, i.e. displacement. For each of the four spring designs, Figure (a) represents the spring's FEA stress contour in the final deformed configuration. The node numbers are labeled to identify the location of each element, where element 1 is between nodes 1 and 2, and so forth. The stress contour corresponds with the bending stresses (z-axis) in Figure (b), plotted against the displacement (x-axis) and the element number (y-axis). Figure (c) and (d) plot the axial stresses and the absolute value of the axial stresses, respectively, along the z-axis.

Observations are made about each of the four spring designs. In the bending stress plot for the J-curve design (Figure 6-3(b)), all the elements have J-shaped profile, except for elements near 3-13 which increase in bending stress and then decrease. In the axial stress plot (Figure 6-3(c)), the elements 1-8 are in tension while elements 11-21 are in compression. The elements in between form the bend in the spring and act as a transitioning point between the opposing axial stresses. Except for these transitioning elements, Figure 6-3(d) shows that the absolute value of the axial stress is almost uniform along the spring and has a J-shaped profile. Comparing Figure 6-3(b) and Figure 6-3(d), the J-shaped response is clearly more influenced by the axial stresses.

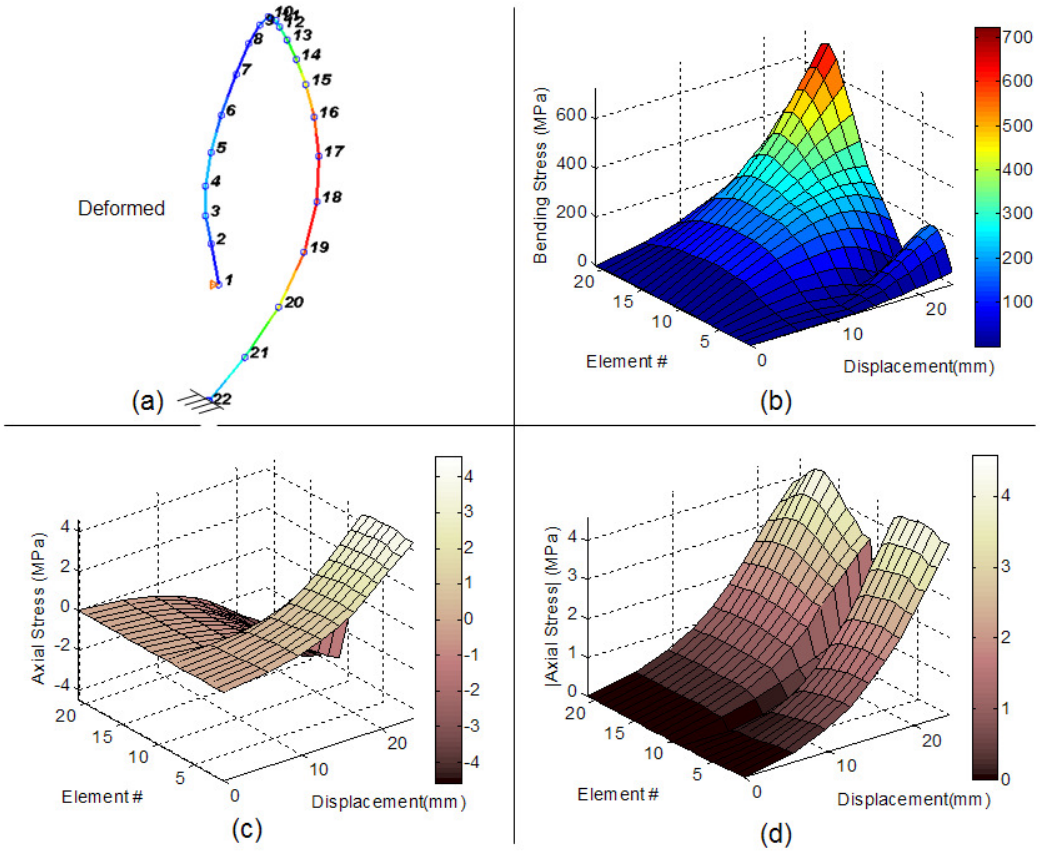

Figure 6-3: J-curve spring, (a) FEA stress contour in deformed configuration, (b) bending stresses, (c) axial stresses, (d) absolute value of axial stresses.

The plots for the S-curve spring are much more complex. In the bending stress plot (Figure 6-4(b)), none of the elements show a true S-shaped profile. In the axial stress plot (Figure 6-4(c)), elements 1-15 are mostly in compression and follow a generally convex profile. Elements 15-19 however follow an S-shaped profile. These elements are located near the fixed point of the spring. The absolute value of the axial stresses (Figure 6-4(d)), more clearly show the S-shaped profile of the elements near the spring's fixed end. Comparing the fluctuation of bending (Figure 6-4(b)) and axial (Figure 6-4(c)) stresses *along the length* of the spring at 40mm displacement the bending stresses change more gradually than the constantly fluctuating axial stresses. Overall, the S-shaped load-displacement function more closely correlates with the axial stresses; however, unlike the J-curve design, the axial stresses are not uniform along the spring's length.

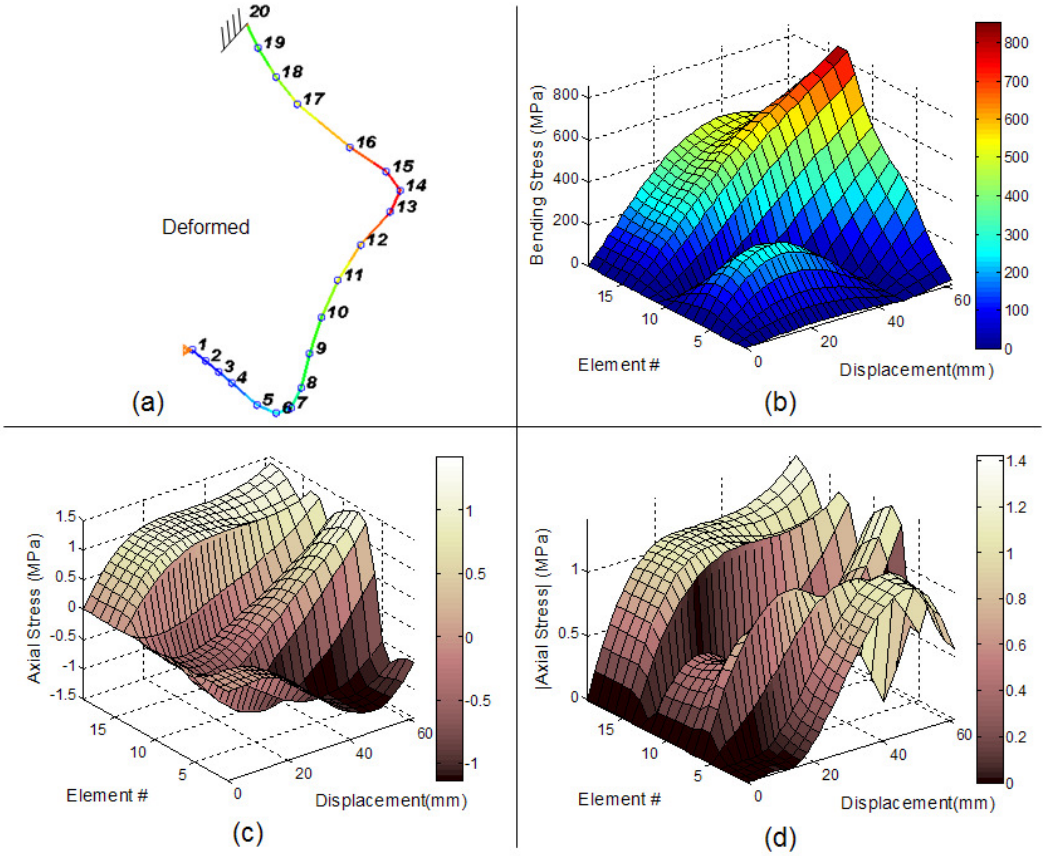

Figure 6-4: S-curve spring, (a) FEA stress contour in deformed configuration, (b) bending stresses, (c) axial stresses, (d) absolute value of axial stresses.

The plots for the constant-force spring are shown in Figure 6-5. In the bending stress plot (Figure 6-5(b)), none of the elements show a true constant-force profile, although many of the elements show a gradual softening behavior. In the axial stress plot (Figure 6-5(c)), the first six elements are in compression, while elements 7-17 are in tension. Except for the transition point that occurs between these groups of elements, all the elements have a constant-force profile. This can also be seen in Figure 6-5(d). At 20mm displacement, the bending stresses seem to fluctuate more than the axial stresses along the length of the spring. This is opposite of what was observed for the S-curve spring. Once again though, the axial stresses seem to greatly influence the spring's constant-force response.

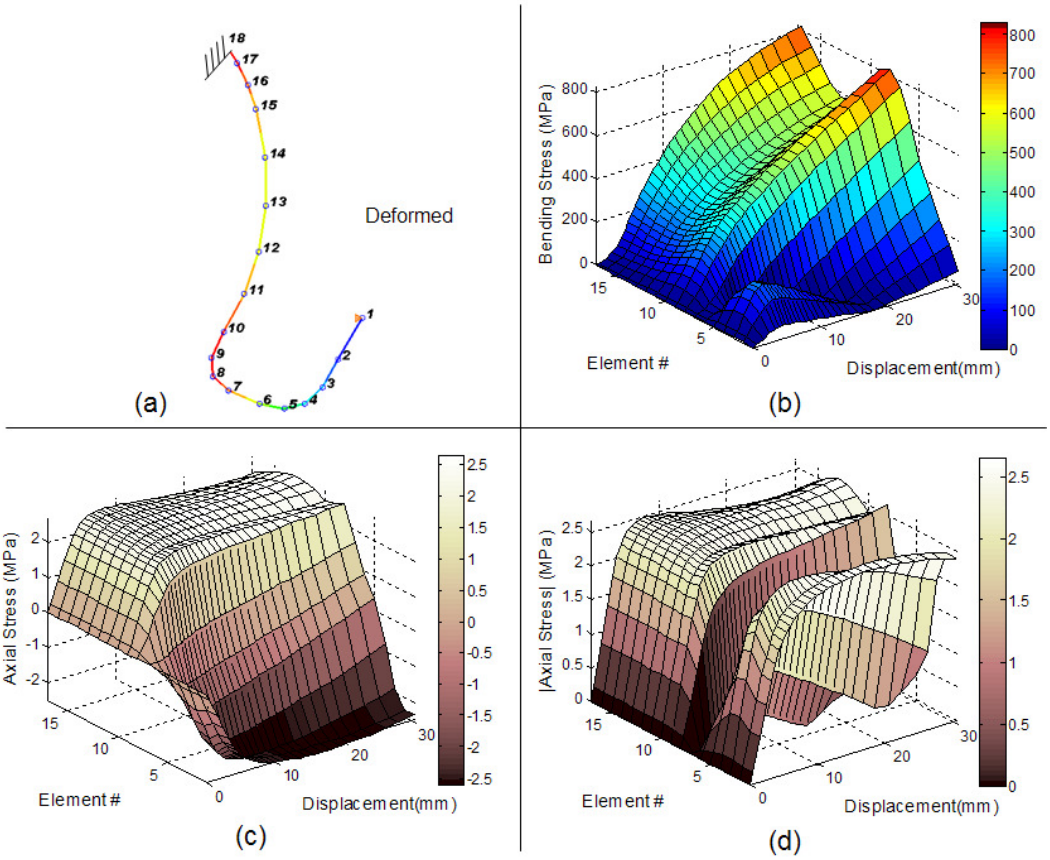

Figure 6-5: Constant-force spring, (a) FEA stress contour in deformed configuration, (b) bending stresses, (c) axial stresses, (d) absolute value of axial stresses.

Finally, the plots for the linear spring are shown in Figure 6-6. In the bending stress plot (Figure 6-6(b)), the elements seem to increase their bending stress at a fairly linear rate, although the elements between 2-7 and 15-17 have a higher magnitude of bending stress. In the axial stress plot (Figure 6-6(c)), elements 1-10 are for the most part are in tension, while the remaining elements are in compression. Figure 6-6(d) shows that the magnitude of the axial stress in each beam element generally increases at a linear rate. At a 30mm displacement, both the bending and axial stresses have comparable fluctuations along the spring's length. Overall, it is difficult to tell whether the bending or axial stresses have a more dominate influence on the spring's linear response.

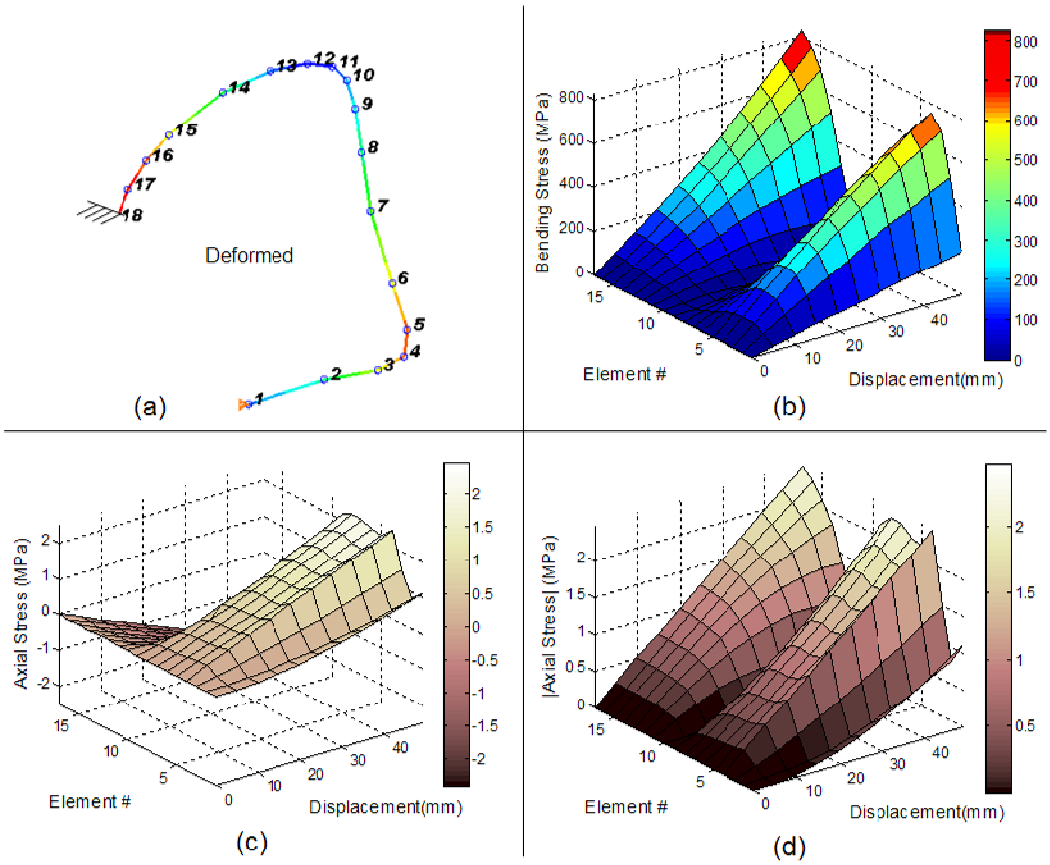

Figure 6-6: Linear spring, (a) FEA stress contour in deformed configuration, (b) bending stresses, (c) axial stresses, (d) absolute value of axial stresses.

6.1.2 Discussion

Based on these four spring designs, the J-curve, S-curve, constant-force, and linear spring, several generalizations can be made about the influence of bending and axial stresses on a spring's nonlinear response.

1) The *magnitude* (absolute value) of *axial* stresses within a spring has a substantial influence on a spring's response (shape function).
2) The *bending* stresses within a spring may have a slight influence on a spring's response, since both the J-curve and linear springs had a few beam elements whose bending stress profile generally matched the spring's response (shape function).
3) The fluctuation of *axial* stresses both along a spring's length and over its range of motion (refer to Figure 6-4(c)) may enable greater nonlinearities, since the S-curve design had this fluctuation and was the only nonlinear spring with an inflection point in its shape function. The J-curve and constant-force spring designs had fairly uniform magnitudes of axial forces over the spring's length. The linear spring had more fluctuation along the spring's length, but unlike the S-curve spring, this fluctuation remained constant over the spring's range of motion (refer to Figure 6-6(d)).

Overall, this study suggests that *geometric nonlinearities and boundary conditions enable spring segments (beam elements) to vary the contribution of their axial stiffness over the spring's range of motion. When the magnitude of a spring's axial stiffness response is nonlinear, springs are likely to have a correlating nonlinear load-displacement response.* One may expect bending stresses to decline as axial stresses increase, resulting in a beam element "trading-off" between bending and axial stresses. However, the stress results for the four springs show that the majority of the beam elements have an increasing bending stress. For example, element 15 in the constant force spring (Figure 6-5) has an axial stress profile resembling a constant-force shape function, while its bending stress profile is continuously increasing, not decreasing. Therefore, the influence that axial stresses have on a spring's response seem independent of the fluctuation of bending stresses. More springs would need to be studied to confirm these generalizations.

6.2 General Shape of Nonlinear Springs

This section presents several single spline topologies of each of the four spring types (J-curve, S-curve, constant-force, and linear). The goal is to find correlations between a spring design's shape and its corresponding response (shape function). This provides general guidelines for designers wishing to eliminate topology synthesis and instead make an initial guess for a single spline topology. Subsequently, size and shape optimization would determine the final design.

For clarity in the figures, the boundary condition at the input of the springs is not shown; however, like all previous designs, the input has a translational constraint in the horizontal direction. Figure 6-7 shows four springs that each have a J-shaped load-displacement shape function. Each of these springs fold in on themselves, suggesting that "folding" causes a stiffening behavior as represented by the J-shaped shape function. Figure 6-8 shows four springs that each have an S-shaped shape function. Three out of the four designs "unfold" as shown in Figure 6-8(b), (c), and (d). As a whole, Figure 6-8(a) folds in on itself, however the hairpin-shaped bend unfolds slightly during deformation. Since an S-curve begins its shape function with a softening behavior, these designs suggest that "unfolding" enables a spring to soften. The next group of designs is constant-force springs which have a softening effect and then remain near a constant stiffness. Given the observations from the J- and S-curve springs, the designs are expected to primarily unfold, while folding may also be necessary to control a constant stiffness. As expected, the four designs in Figure 6-9 either (i) only unfold or (ii) both fold and unfold. Following the same generalizations, the linear springs are expected to balance both folding and unfolding in order to remain at a constant stiffness over the spring's range of motion. Figure 6-10 confirms this hypothesis; all four linear spring designs have sections that unfold and sections that fold.

Thus, the following generalizations can be made for single spline topologies with a translational constraint at the input:

1) For a stiffening response, shape a spring such that it folds on itself under the applied load.

2) For a softening response, shape a spring such that it unfolds under the applied load.
3) For constant stiffness, shape a spring such that one section unfolds and another section folds under the applied load.

Given the observations made in the previous section, one can generalize that folding increases the rate of change in the axial stresses for a hardening effect, while unfolding decreases the rate of change in axial stresses for a softening effect. At the least, these guidelines provide the designer some intuition on nonlinear spring design.

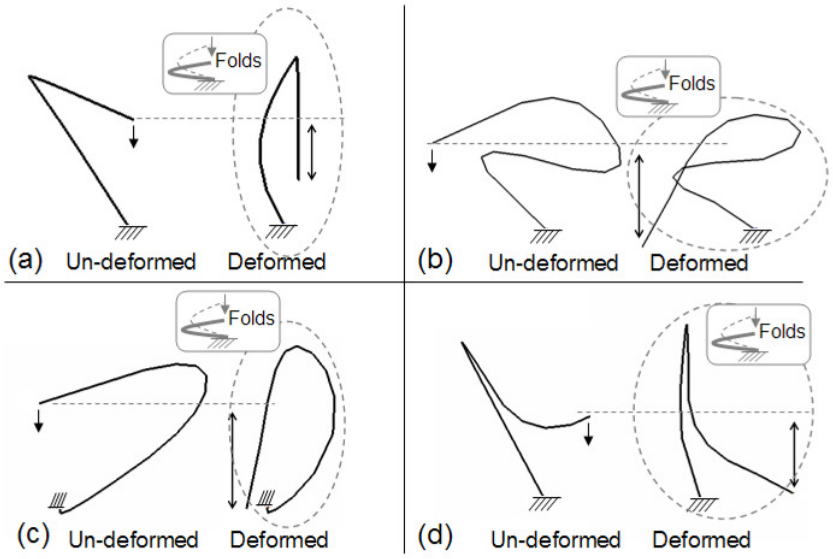

Figure 6-7: Single spline J-curve spring topologies and their deformations.

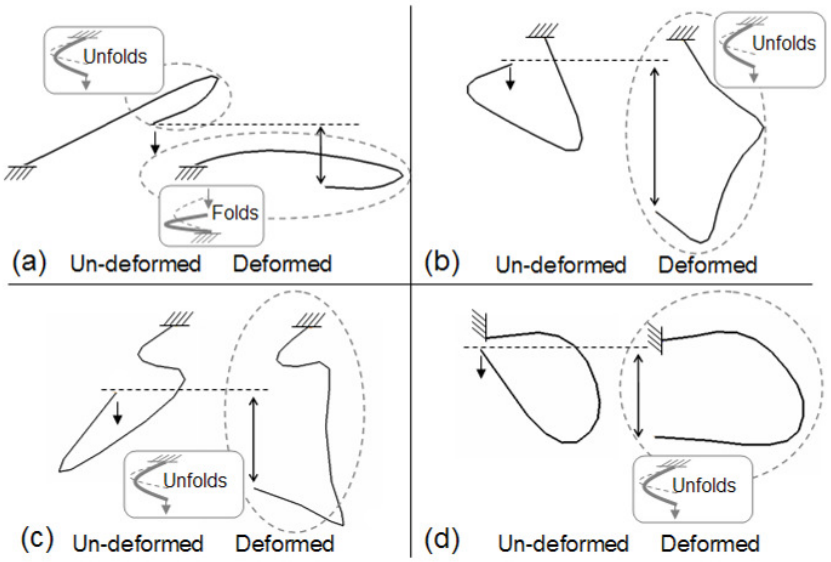

Figure 6-8: Single spline S-curve spring topologies and their deformations.

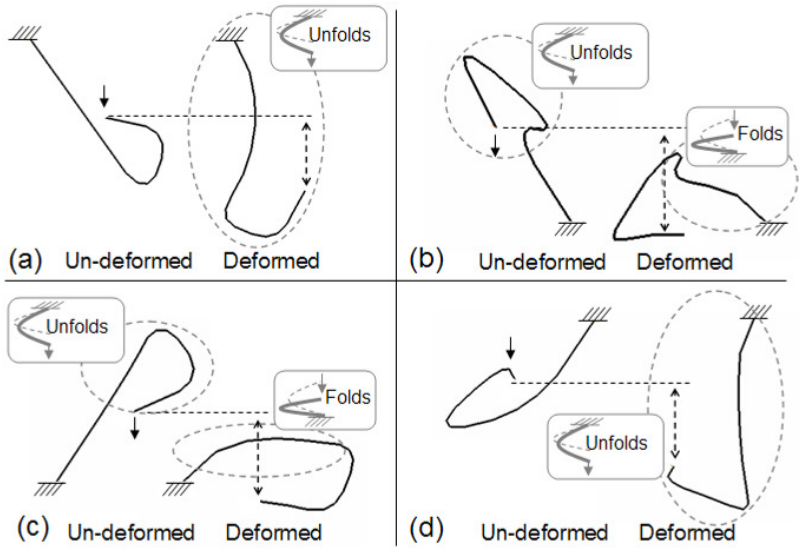

Figure 6-9: Single spline constant-force spring topologies and their deformations.

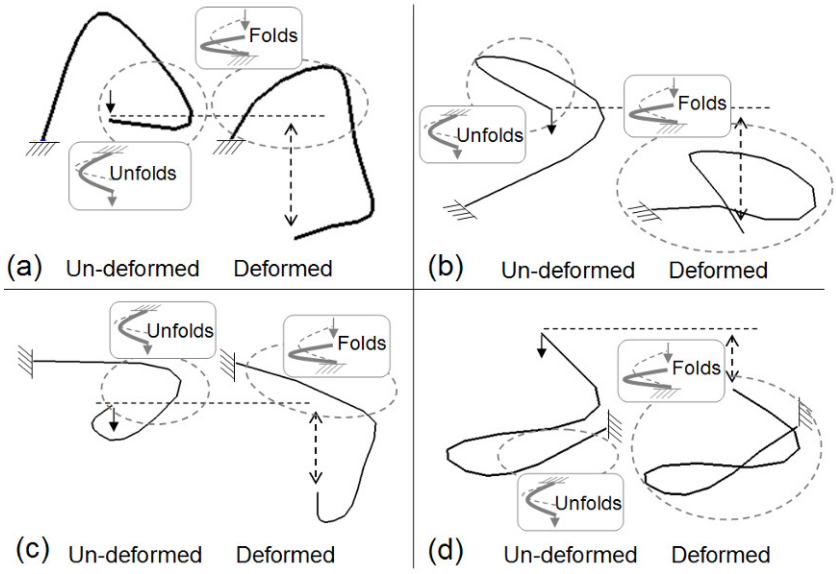

Figure 6-10: Single spline linear spring topologies and their deformations.

CHAPTER 7

TIERED STRUCTURES AND SCALABILITY

This chapter provides guidelines for configuring an existing nonlinear spring design in new ways to meet different design specifications. The first section considers nonlinear springs in tiered arrangements, i.e. in series and parallel, while the second section provides scaling rules for nonlinear springs.

7.1 Tiered Structures

Figure 7-1 illustrates how one nonlinear spring, defined as a unit cell, can be placed in a tiered arrangement to offer new design options and applications for nonlinear springs. The figure shows a two dimensional array or sheet of nonlinear springs. These arrays can be fabricated to match prescribed uniaxial elasticities. In addition, their porous structure offers potential to house other materials, such as a damping material or regenerative cells and proteins for tissue engineering purposes.

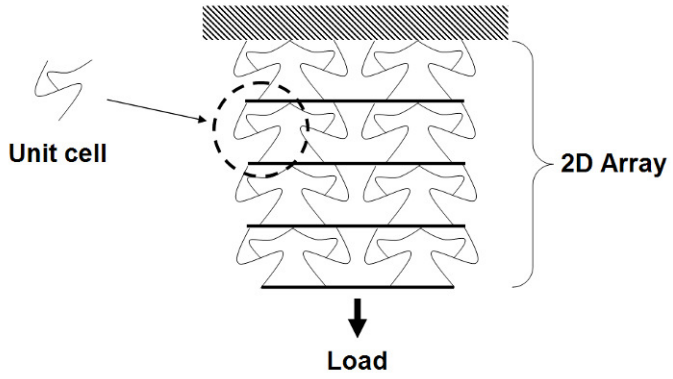

Figure 7-1: A nonlinear spring (unit cell) arranged in a two dimensional array.

Consider tiered arrangements of linear springs, where each spring has a stiffness of K. Figure 7-2(b) shows that a linear spring in parallel has double the stiffness of a single spring. In series, the equivalent stiffness is half (Figure 7-2(c)). When placing

four linear springs in a series-parallel arrangement (Figure 7-2(d)), the effective stiffness is equivalent to a single spring.

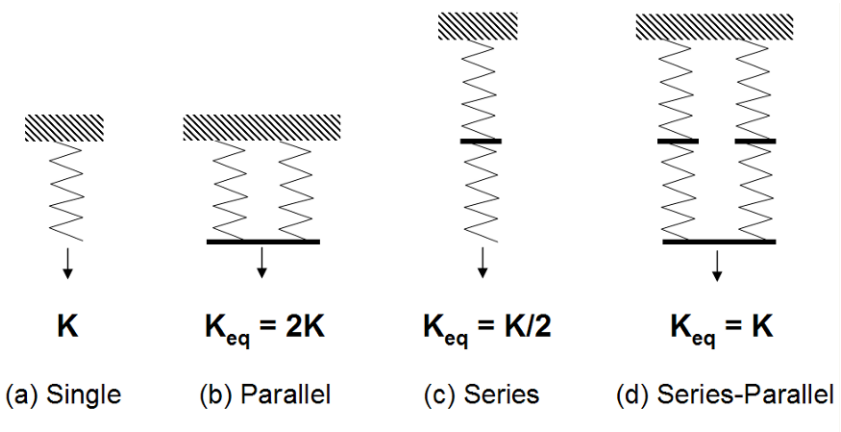

Figure 7-2: Tiered arrangements of linear springs (K = stiffness).

With nonlinear springs, the stiffness is not constant over the springs' range of motion, i.e. it cannot be represented with a single stiffness value K. Therefore, this section explores the response of nonlinear springs in parallel, series, and series-parallel arrangements and provides guidelines for maintaining a spring's nonlinearity (its shape function) within a tiered arrangement.

7.1.1 Nonlinear Springs in Series and Parallel

Table 7-1 delineates the load- and displacement-ranges required to maintain the shape function of a nonlinear spring (the unit cell) when placed in a tiered arrangement. When X number of springs are in parallel, the load-range increases by a factor of X but the displacement-range remains unaltered. When Y number of springs are in series, the load-range is unaltered but the displacement range increases by a factor of Y. This section provides four FEA examples to validate these guidelines.

The first three examples analyze a J-curve spring in parallel, series, and series-parallel arrangements. Figure 7-3 and Figure 7-4 show the unit cell's topology/shape and load-displacement function, respectively. The overlapping in the spring's deformed configuration is disregarded, since the following three examples are only intended for analysis purposes. The unit cell has the following properties: Material: titanium (E = 115GPa), Out-of-plane thickness: 4mm, In-plane thickness: 0.53mm, and Footprint:

41.0mm by 15.1mm. Over a 10N load-range, the spring displaces 11.5mm, and the shape function error is less than 1%. The two target points are located at (25% Displacement, 4% Load) and (50% Displacement, 17% Load), and the resulting maximum stress is 674MPa.

Table 7-1: Load- and displacement-ranges for tiered arrangements having equivalent shape functions as the unit cell.

	Tiered load-range	Tiered displacement-range
Parallel (X springs)	(Xx) unit cell load-range	(1x) unit cell displacement-range
Series (Y springs)	(1x) unit cell load-range	(Yx) unit cell displacement-range
Series-parallel (X by Y springs)	(Xx) unit cell load-range	(Yx) unit cell displacement-range

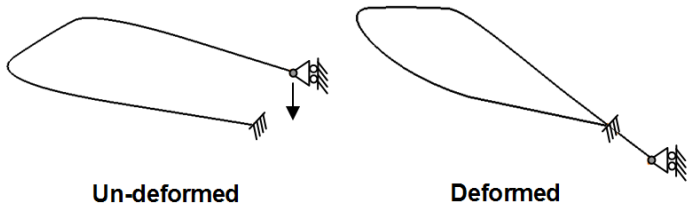

Figure 7-3: Un-deformed and deformed configuration of J-curve unit cell.

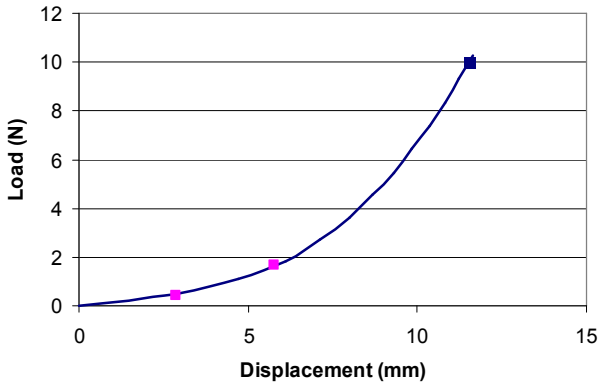

Figure 7-4: Load-displacement function for the J-curve unit cell, (SFE < 1%).

When placing springs in a tiered arrangement the boundary conditions on each unit cell must match the boundary conditions of the original unit cell. For example, Figure 7-5 shows the boundary conditions between two J-curve springs in series. Both springs' endpoints must be constrained in the horizontal direction; however, at the junction between the two springs, the top spring's rotational degree of freedom must be fixed (since it is the fixed point of the top unit cell), while the bottom spring's rotational degree of freedom must be free (since it is the input point to the bottom unit cell).

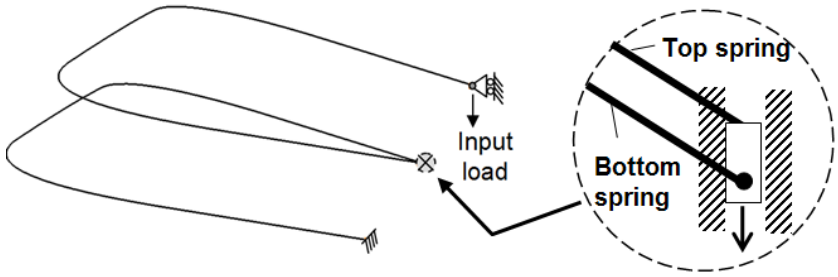

Figure 7-5: Boundary conditions between the two J-curve springs in series.

The following three figures show the FEA results for a J-curve spring in parallel (Figure 7-6), series (Figure 7-7), and series-parallel (Figure 7-8). By following the load- and displacement-range guidelines in Table 7-1, each of the three spring arrangements have the same nonlinearity (SFE < 1%) and maximum stress (674MPa) of a single spring. For the parallel arrangement (Figure 7-6), the load-range was doubled to 20N (as specified for two springs in parallel), and the resulting displacement-range remained the same at 11.5mm. For the series arrangement, Figure 7-7 shows that the load-range was maintained at 10N, but the resulting displacement-range doubled to 23mm. Finally, for the series-parallel arrangement, Figure 7-8 shows that the load-range was doubled to 20N, and that the resulting displacement-range was also doubled to 23mm.

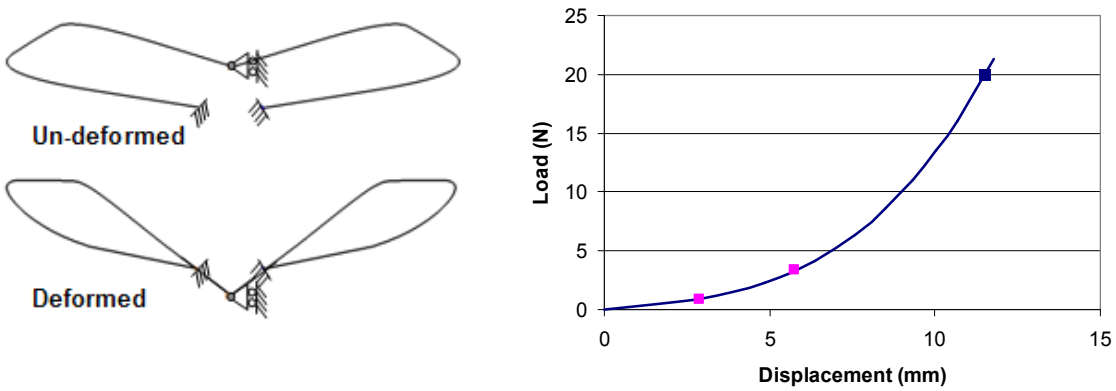

(a) (b)

Figure 7-6: J-curve spring in parallel (Load = 20N (doubled), Displacement = 11.5mm, Stress = 674MPa), (a) un-deformed and deformed configuration, (b) load-displacement function.

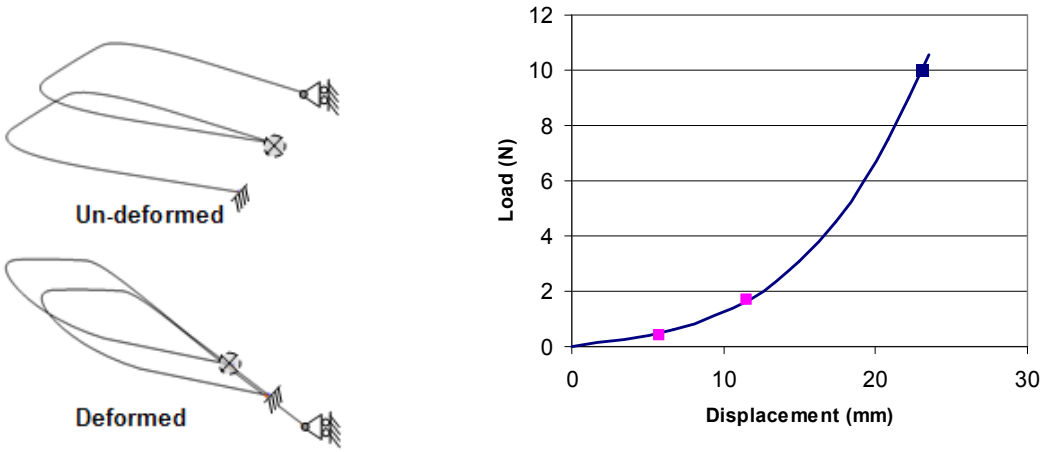

(a) (b)

Figure 7-7: J-curve spring in series (Load = 10N, Displacement = 23.0mm (doubled), Stress = 674MPa), (a) un-deformed and deformed configuration, (b) load-displacement function.

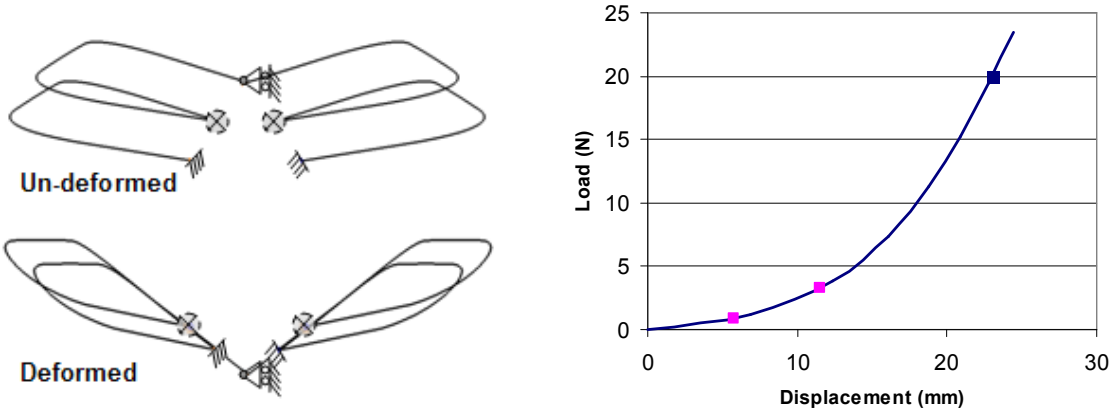

(a) (b)

Figure 7-8: J-curve spring in series-parallel (Load = 20N (doubled), Displacement = 23.0mm (doubled), Stress = 674MPa), (a) un-deformed and deformed configuration, (b) load-displacement function.

A fourth example analyzes a different unit cell, an S-curve spring, in a series of five. Figure 7-9 shows the unit cell's design and load-displacement function, respectively. The unit cell has the following properties: Material: titanium (E = 115GPa), Out-of-plane thickness: 4mm, In-plane thickness: 0.43mm, and Footprint: 45.8mm by 46.4mm. Over a 2.7N load-range, the spring displaces 58.7mm, and the shape function error is less than 1%. The three target points are located at (25% Displacement, 58% Load), (50% Displacement, 66% Load), and (79% Displacement, 75% Load), and the resulting maximum stress is 820MPa.

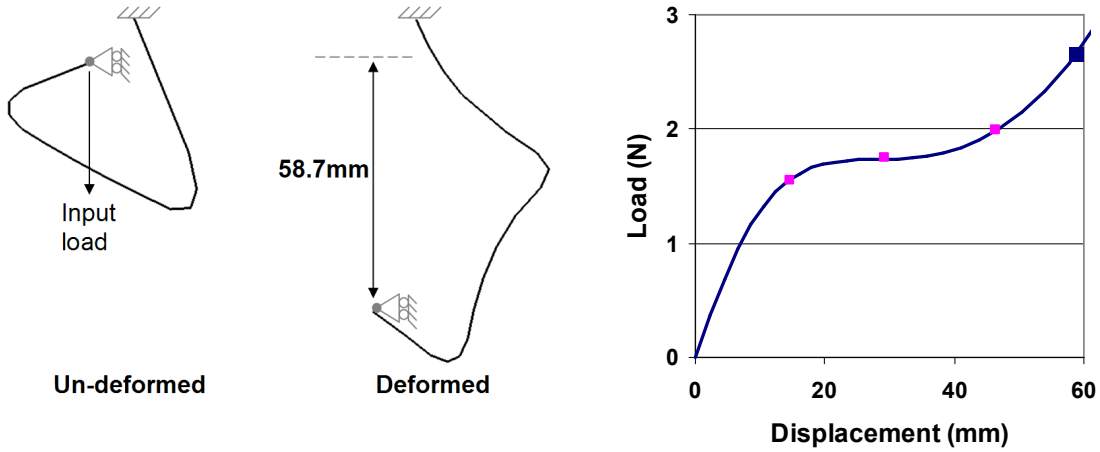

Figure 7-9: S-curve unit cell: (a) un-deformed and deformed configuration and (b) load-displacement function, (SFE < 1%).

Figure 7-10 shows the FEA results for a series of five S-curve springs. Boundary conditions between the individual unit cells match the boundary conditions illustrated in Figure 7-5. The load-displacement function in Figure 7-10(b) shows that the load-range was maintained at 2.7N, but that the resulting displacement-range increased to 294mm (=58.7mm x 5 springs). The spring arrangement maintains the nonlinearity of the single S-curve spring (SFE < 1%) and the maximum stress of 820MPa.

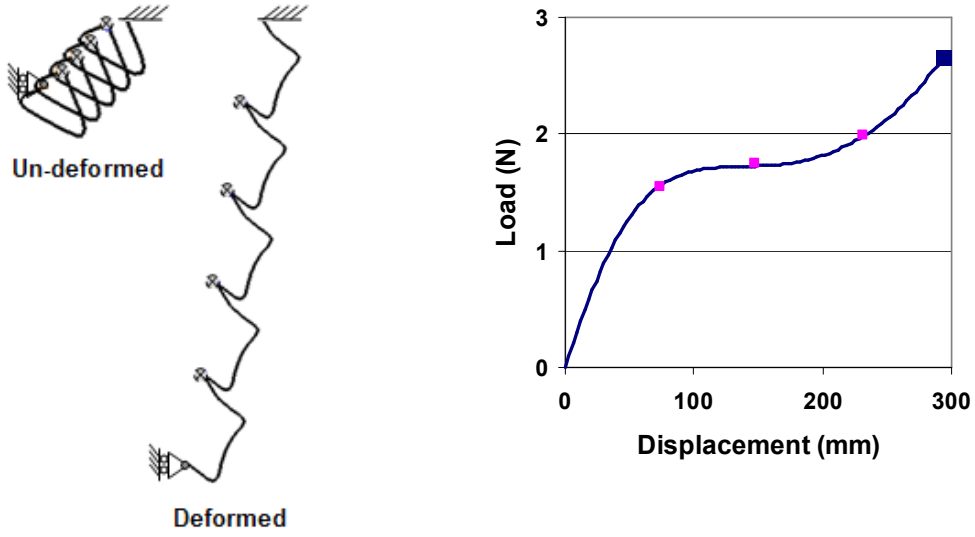

(a) (b)

Figure 7-10: S-curve spring in series (Load = 2.7N, Displacement = 294mm (x5 of original displacement), Stress = 820MPa), (a) un-deformed and deformed configuration, (b) load-displacement function.

7.1.2 Discussion

The examples illustrate that superposition holds for nonlinear springs as long as the guidelines in Table 7-1 are followed. For practical utilization of tiered arrangements, a few points are noted. First, unit cells must be spaced to avoid contact with adjacent springs during deformation. Second, unit cells with rotational boundary conditions require relative rotation at their end points. Therefore, a 2-D array of springs requires an assembly of separate unit cells. Monolithic arrays are possible as long as the unit cell is free of pinned end conditions at the input and ground points. To exploit geometric nonlinearities in the absence of pinned boundary conditions, these unit cells are likely to have more slender splines or a larger footprint, enabling sufficient elemental rotations within specified stress constraints. Finally, as shown in Figure 7-1, symmetric arrangements of springs can eliminate the need for vertical slides that restrain a spring's endpoint from translating in the horizontal direction.

7.2 Scalability of Nonlinear Springs

By understanding nonlinear spring scaling rules, a designer can check whether an existing nonlinear spring design is scalable to meet new design requirements, thus eliminating the need to generate a new spring topology. The goal is to maintain an existing spring's topology, shape, load-displacement shape function, and satisfied stress constraints, while adjusting the (i) load-range, (ii) displacement-range, (iii) in-plane thickness, (iv) out-of-plane thickness, (v) footprint, and/or (iv) material.

Two relations, the (i) elastic flexure formula and the (i) beam deflection formula, are used to guide the scalability rules presented in this section (Beer and Johnston, 1992). The elastic flexure formula holds for beams bending within the elastic range and is given by the following relationship,

$$\sigma = \frac{Mc}{I}, \tag{7-1}$$

where M is the moment, c is the distance from the neutral axis, and I is the moment of inertia. The beam deflection formula is represented for various boundary conditions in the second column of Table 7-2, where P is the point force, L is the length, E is the material's modulus, y is the beam's end point deflection, and I is the moment of inertia. A beam with a rectangular cross-section has three geometric parameters: length (L), in-plane thickness (h), and out-of-plane thickness (b). The two latter parameters are related to the moment of inertia by $I=bh^3/12$. The third column in Table 7-2 rearranges the equations in the second column such that the beam's stiffness (P/y) is isolated on the left side of the equation. Notice that independent of the boundary conditions the right hand side of all three beam deflection equations has a constant, an elastic modulus, and a geometric ratio of I/L^3. By maintaining this ratio, the beam's geometric parameters can be modified without affecting the beam's stiffness.

Table 7-2: The beam deflection formula for various boundary conditions (Beer and Johnston, 1992).

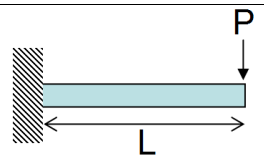	$y = -\frac{PL^3}{3EI}$	$\frac{P}{y} = -\frac{3EI}{L^3}$
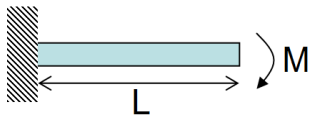	$y = -\frac{ML^2}{2EI}\left(= -\frac{(PL)L^2}{2EI} = -\frac{PL^3}{2EI}\right)$	$\frac{P}{y} = -\frac{2EI}{L^3}$
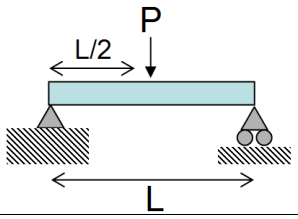	$y = -\frac{PL^3}{48EI}$	$\frac{P}{y} = -\frac{48EI}{L^3}$

Equation (7-2) represents the geometric ratio (with the constants left out). To scale the beam and maintain the cross-section's aspect ratio, both of the cross-sectional thicknesses are scaled by n while the length is scaled by N. By inserting these values into Equation (7-2), the geometric ratio remains unchanged when the cross-sectional scaling factor, n, and length scaling factor, N, satisfy Equation (7-3). For instance, if a beam's length (L) is doubled ($N = 2$) and the cross-sectional dimensions (b and h) are increased by a factor of 1.68 ($n = 2^{3/4}$), the beam's overall stiffness (P/y) will remain unchanged. Thus, by scaling a beam's geometry according to these relationships, the beam's stiffness is unaltered.

$$\frac{I}{L^3} = \frac{b*h^3}{L^3} = \frac{(b*n)(h*n)^3}{(L*N)^3} = \frac{b*h^3(n^4)}{L^3(N^3)} = \frac{I(n^4)}{L^3(N^3)} \tag{7-2}$$

$$n = N^{3/4} \tag{7-3}$$

Since the spring deflections in this work are primarily due to bending deflection and not axial, these straight beam scaling relationships are utilized. The examples below verify that these relationships hold for nonlinear springs.

7.2.1 Load-range

A nonlinear spring's load-range scales linearly with its out-of-plane thickness as shown in Table 7-3. This follows the rules for parallel springs, where a spring in parallel with itself has essentially twice the out-of-plane thickness of a single spring and exactly twice the load-range. Since the stresses and displacement range are unaffected, *it is recommended that a spring's load-range is scaled by its out-of-plane thickness and not its in-plane thickness* as will be described below.

Table 7-3: Load-range scaling rules when altering the out-of-plane thickness.

Parameter	**Modification**
Load-range	Multiply by factor N
Out-of-plane thickness	Multiply by factor N
Response/Stresses	**Effect**
Displacement-range	Unaffected
Shape function	Unaffected
Stresses	Unaffected

A spring's load-range can also be scaled by modifying the spring's material or its in-plane thickness, but these alterations change the stresses. The next section explains the load-range/material scaling problem. Noting the beam defection equations in Table 7-2, the load (P) is proportional to in-plane thickness (h), since $I = bh^3/12$. Therefore, Table 7-4 provides the modifications necessary to change a spring's load-range by modifying its in-plane thickness. The parameters scale nonlinearly due to the relationship between the moment of inertia and the in-plane thickness in $I=bh^3/12$, and the modifications of the in-plane thickness affect the stresses based on Equation (7-1).

Table 7-4: Load-range scaling rules when altering the in-plane thickness.

Parameter	**Modification**
Load-range	Multiply by factor N
In-plane thickness	Multiply by factor $N^{1/3}$
Response/Stresses	**Effect**
Displacement-range	Unaffected
Shape function	Unaffected
Stresses	(Based on Equation (7-1)) Original stress*($N^{1/3}$)

7.2.2 Material

A nonlinear spring's material modulus scales linearly with its load-range and out-of-plane thickness. Noting the beam defection equations in Table 7-2, the load (P) is proportional to the material modulus (E) whereas the out-of-plane thickness (b) is inversely proportional to the material (E), since $I = bh^3/12$. Therefore, Table 7-5 summarizes the modifications necessary to change a spring's material while maintaining its displacement-range and shape function. The scaling alters the stresses according to the elastic flexure formula in Equation (7-1).

Table 7-5: Material scaling rules for nonlinear springs.

Parameter	**Modification**
Material modulus (E)	Multiply by factor N
Load-range or (*out-of-plane thickness*)	Multiply (*Divide*) by factor N
Response/Stresses	**Effect**
Displacement-range	Unaffected
Shape function	Unaffected
Stresses	(Based on Equation (7-1)) Original stresses*N

Two examples are presented to verify the relationships in Table 7-5. Table 7-6 compares the initial spring's load-range, out-of-plane thickness, and maximum stress to the two example problems, each made of aluminum (E=70GPa). Therefore, the scaling factor N equals 0.61 (70GPa/115GPa). The first example scales the material modulus by modifying the load-range (third column) and the second by the out-of-plane thickness (fourth column). The initial spring design is a titanium S-curve spring (E=115GPa) whose topology/shape and load-displacement function are depicted in Figure 7-11. Using FEA, Table 7-6 shows that the maximum stress results for the aluminum springs are 501MPa, equal to N times the original stress, 822MPa. Figure 7-12 shows the resulting load-displacement functions of the two examples. In both cases, the shape function and displacement-range are maintained over the load-ranges specified in Table 7-6.

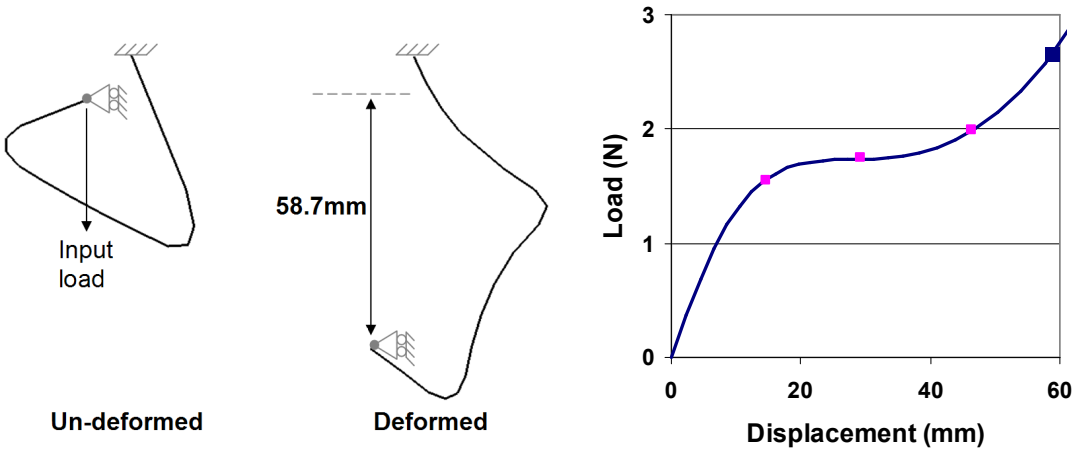

(a) (b)

Figure 7-11: Initial titanium S-curve design before scaling.

Table 7-6: Scaled parameters (in bold) and FEA results for the two aluminum spring examples, (N=0.61).

	Parameters			FEA	
	Material	Load-range (Newtons)	Out-of-plane thickness (mm)	Max stress (MPa)	Disp-range (mm)
Original	Titanium	2.66	4	822	58.7
Ex. 1	Aluminum	(**1.62**) =2.66*N	4	501	58.8
Ex. 2	Aluminum	2.66	(**6.57**) = 4/N	501	58.8

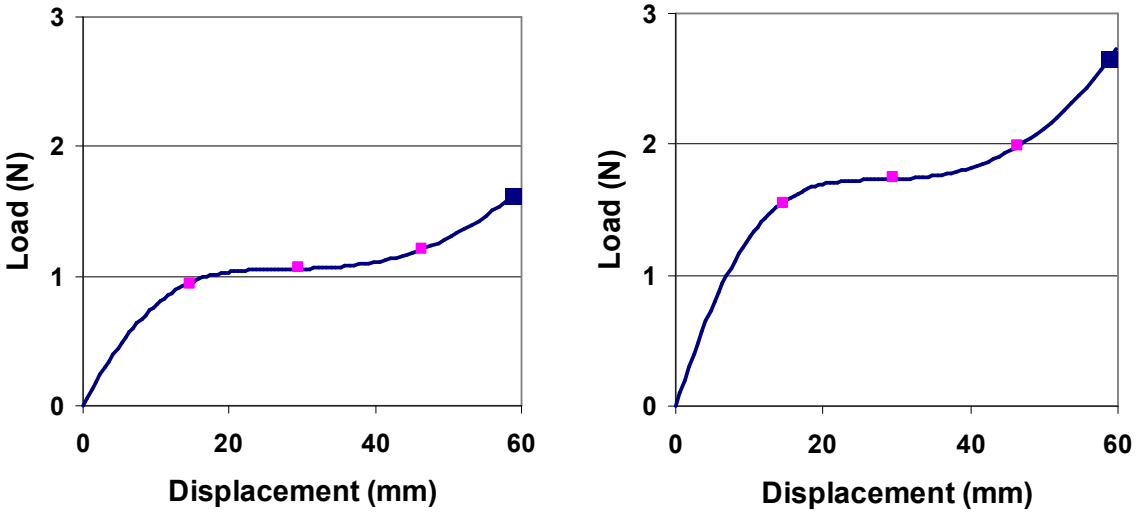

(a) (b)

Figure 7-12: Load-displacement functions for material scaling examples, (a) Ex. 1, (b) Ex. 2.

7.2.3 Footprint of Spring

A nonlinear spring's footprint scales linearly with its load-range and displacement-range, as long as the beam's cross-section (in-plane and out-of-plane thicknesses) is scaled appropriately. Table 7-7 summarizes the modifications necessary to maintain a spring's shape function, based on the beam deflection equations in Table 7-2Table 7-2 and Equation (7-3). Since many parameters are modified when scaling the footprint, the resulting stresses are best determined from FEA.

Table 7-7: Footprint scaling rules for nonlinear springs.

Parameter	**Modification**
Footprint	Multiply each x and y coordinate by N
Load-range	Multiply by N
In-plane and out-of-plane thicknesses	Multiply by factor $N^{3/4}$
Response/Stresses	**Effect**
Displacement-range	Original displacement-range*N
Shape function	Unaffected
Stresses	Lower when N>1 Higher when N<1 Stresses determined by FEA

A final example verifies the relationships in Table 7-7 by scaling a nonlinear spring's footprint by a factor of five, (N=5). The initial spring design is the same S-curve spring used in the previous example. Table 7-8 compares the initial spring's footprint scale, load-range, out-of-plane thickness, in-plane thickness, maximum stress, and displacement-range to that of the scaled spring design. The load-range increases by a factor of N, while the cross-sectional thicknesses increase by a factor of $N^{3/4}$. The resulting stress for the scaled spring is 539MPa, which is lower than the initial spring's stress. This was predicted in Table 7-7 since N>1. Figure 7-13 shows the scaled design's load-displacement function. As predicted, the shape function is maintained over the applied load, 13.3N (=5*2.66N) and a new displacement-range, 293.5mm, which is five times as large as the original spring's displacement-range of 58.7mm.

Table 7-8: Scaled parameters and FEA results for the scaled S-curve footprint example.

	Parameters				FEA	
	Footprint scale, N	Load-range (Newtons)	Out-of-plane thickness (mm)	In-plane thickness (mm)	Max stress (MPa)	Disp-range (mm)
Original	1	2.66	4	0.49	822	58.7
Example 3	5	13.3	13.37	1.64	539	293.5

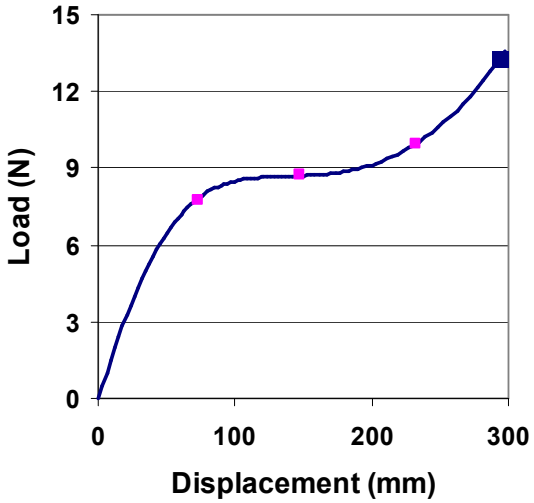

Figure 7-13: Load-displacement function for the scaled S-curve footprint example.

7.2.4 Discussion

These scalability rules are powerful tools when modifying existing springs designs for new design requirements. This has already been demonstrated to a large extent in the example problems of Chapter 5, where springs were scaled to improve optimization performance and meet specified load- and displacement-ranges.

Since the elastic flexure formula (stress equation) and the beam deflection formulas are based on linear beam theories, it may not seem intuitive that each can be employed in nonlinear spring design. One must remember though that these relationships are not being used for analysis purposes, only for scaling purposes. In this way, nonlinear FEA first determines a spring's response. Afterwards, both formulas provide insight as to whether a change in a design parameter will alter the spring's load-displacement function or stresses, and if so, by how much.

CHAPTER 8

APPLICATIONS

This chapter presents two fabricated nonlinear spring designs, both of which are tested for their nonlinear response. The first design is implemented into an automotive seat assembly as a cost-saving alternative to a current design. The second design is a constant-force spring which has multiple applications. This chapter also addresses relevant manufacturing issues for the two spring designs.

8.1 Automotive Seat Cushion Spring

An automotive company asked a University of Michigan senior design team to reduce the manufacturing and logistics costs of an automobile passenger seat assembly. Figure 8-1(a) shows the current seat assembly for the vehicle's back, middle seat. Since the seat's pan is rigid (Figure 8-1(b)), the current design employs a 4 inch thick foam cushion that lays upon the pan in order to provide the passenger sufficient comfort. The volume of the 4-inch seat cushion results in high storage and transportation costs for the automotive company. Therefore, the primary goal of the new seat design was to reduce the cushion's thickness by half (2 inches), while not compromising the passenger's comfort. Furthermore, the design should reduce or maintain the assembly's current weight and costs.

(a)

(b)

(Knauf et al., 2006)

Figure 8-1: (a) Back, middle passenger's seat, (b) Seat pan without foam.

To match the overall comfort of the original design, the automotive company provided the load-displacement data measured at the center of the current seat cushion assembly. The data's plot in Figure 8-2 depicts a nonlinear response.

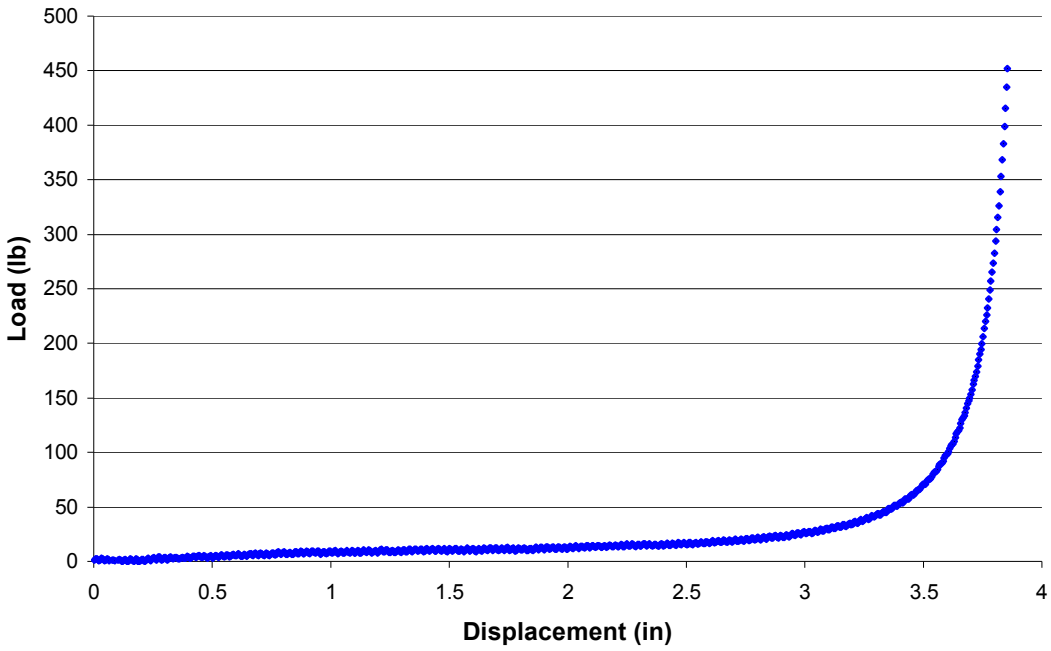

(Knauf et al., 2006)

Figure 8-2: Automotive company's load-displacement data measured at the center of the original 4-inch seat cushion.

8.1.1 Problem Set-Up

The team's faculty advisor, Dr. Sridhar Kota, proposed using a compliant mechanism in place of the rigid seat pan in order to compensate for the 2-inch reduction of foam. Since the foam functions as a nonlinear spring, Dr. Kota challenged the senior design team to employ nonlinear springs within the new seat assembly to create equivalent comfort using half the foam (Figure 8-3).

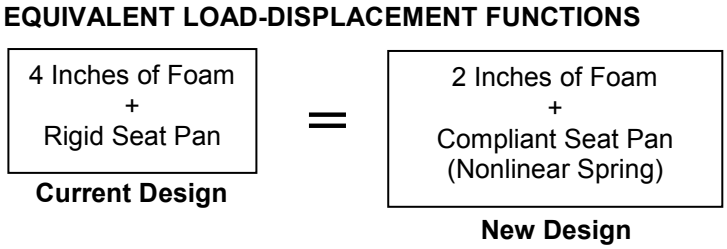

Figure 8-3: Design model for seat assembly.

Using the algorithm (code) generated in this dissertation, I designed a nonlinear spring to meet the design requirements. Figure 8-4 illustrates the senior design team's final design concept from a side, section view of the seat. The profile represents the design space specified by the automotive company and is defined by the seat frame dimensions. The anti-submarine feature in the front of the seat protects the passenger from sliding under the seatbelt during a frontal collision. This feature was a requirement of the automotive company and already a part of the current seat design. The connecting plate is the interface between the nonlinear springs and the 2-inch foam cushion. The cushion rests on top of the connecting plate, while 2 parallel nonlinear springs (not illustrated in Figure 8-4) connect the bottom legs of the connecting plate to the frame via the support cross bars (Knauf et al., 2006). The challenge was to design parallel nonlinear springs that fit within the design space and whose load-displacement function matched that of a 2 inch foam cushion.

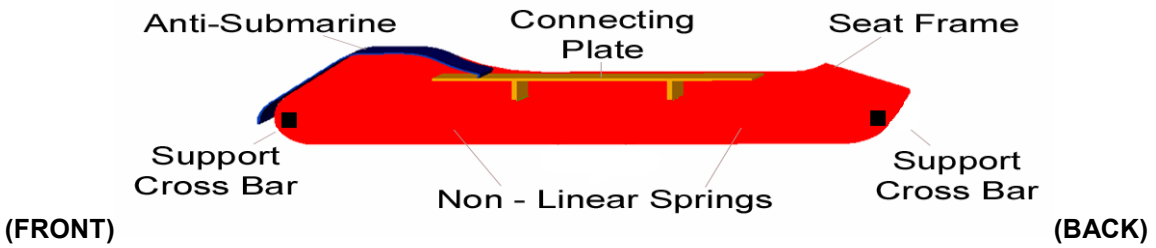

(Knauf et al., 2006)

Figure 8-4: Final design concept. A side, section view of the seat.

Prescribed Load-Displacement Function

The nonlinear springs function to support the load of the passenger while providing the same comfort and response as a 2-inch foam cushion. Table 8-1 depicts the eleven load-displacement target points chosen by the team to represent the automotive company's data. These target points represent the prescribed response for *one* spring. Therefore, the maximum load of 200lbs (890N) is half of the automotive company's prescribed maximum load of 400lbs since the springs are in parallel. In addition, the springs are designed to produce half of the prescribed total displacement of 3.84in, while the remaining 2-inch foam cushion accounts for the other half, 1.92in (48.8mm).

Table 8-1: Target load-displacement points for one nonlinear spring.

Load		**Displacement**	
(lbf)	(N)	**(in)**	(mm)
1.6	7	**0.20**	5
3.8	17	**0.39**	10
4.9	22	**0.59**	15
5.4	24	**0.79**	20
6.3	28	**0.98**	25
7.9	35	**1.18**	30
9.9	44	**1.38**	35
16.2	72	**1.57**	40
39.3	175	**1.77**	45
116.9	520	**1.89**	48
200.0	890	**1.92**	48.8

Space and Material Constraints

Since the springs are located within the seat frame and under the remaining 2-inch foam cushion, the team specified space constraints for the planar spring design. The specified out-of-plane thickness was 12in (304.8mm). The in-plane thickness constraints were 0.02 - 0.069in (0.5 - 1.75mm). The prescribed material was spring steel (E=200GPa) with a yield point of 800MPa. Figure 8-5 illustrates the design space for one of the two nonlinear spring in parallel. The load transferred through the connecting plate and applied onto the spring is located at the upper-right corner of the design space. This point is constrained in the horizontal direction. The grounded end of the spring may connect to the frame at any point within the design space shown.

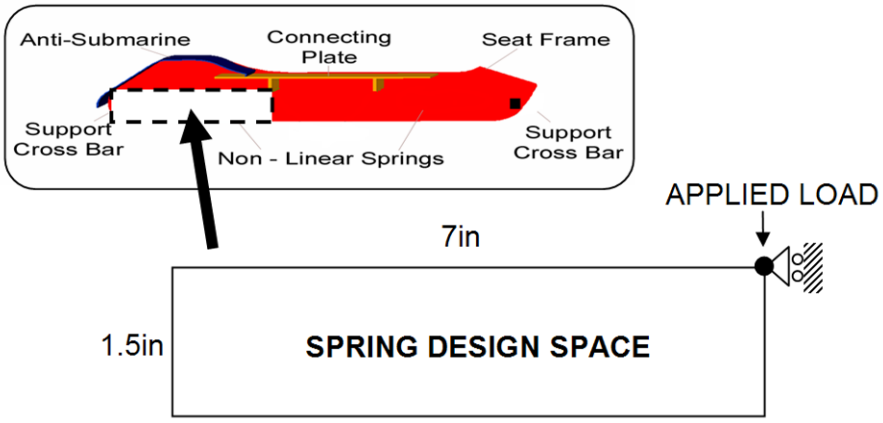

Figure 8-5: Design space specifications for one nonlinear spring.

8.1.2 Procedure

Due to cost and manufacturing constraints, the simplest spring topology, one spline, was chosen. Therefore, only size and shape optimization had to be performed. The objective function formulation (Equation (4-2)) included the shape function error (SFE) to evaluate the spring's nonlinear response, the target displacement penalty (DP_{Target}) since an exact displacement-range was required, the slope bulking penalty (BP_{Slope}) which checks for negative stiffness, and a stress penalty (SP). During the optimization, each spring design was subjected to the same applied load, 200lbs (890N). Since the out-of-plane thickness was prescribed at 12in (304.8mm), load-range scaling was not an option. Therefore, each spring design was analyzed over the entire load-

range, whether the spring yielded or not. If the spring did yield, the design was penalized based on the stress penalty (SP) in Equation (8-2).

$$Objective\ Function = min(SFE + DP_{Target} + BP_{Slope} + SP) \tag{8-1}$$

$$SP = \begin{cases} 0, & \sigma_{spring} < \sigma_{max} \\ \left(\dfrac{\sigma_{spring}}{\sigma_{max}} - 1 \right) * 100\% * W_{Stress}, & \sigma_{spring} > \sigma_{max} \end{cases} \tag{8-2}$$

For the objective function, the displacement penalty weight was 1, the buckling penalty weight was 50, and the stress penalty weight was 1. The GA was executed for 40 generations with a population size of 114 individuals. The best 10% of each population was transferred to the next generation. Each shape variable was enabled to crossover independently, and the crossover and mutation rates were 70% and 9%, respectively.

8.1.3 Nonlinear Spring Design

Using the nonlinear spring synthesis methodology, Figure 8-6 shows the generated spring design in its un-deformed and deformed shape. This design meets the space and stress constraints. The spring's in-plane thickness is 0.027in (0.69mm) and the maximum stress is 605MPa, well below the yield point. The combined shape function error and target displacement error is 0.98%. The slope buckling penalty was satisfied for a fixed incremental arc-length of 0.06. The incremental arc-length controls the resolution of solved equilibrium points along a design's load-displacement curve. A fixed arc-length of 0.06 had been sufficient for many other spring analyses. Figure 8-7 shows the spring's load-displacement function with markers indicating the location of solved equilibrium points. At this point in the research, the negative eigenvalues were not checked.

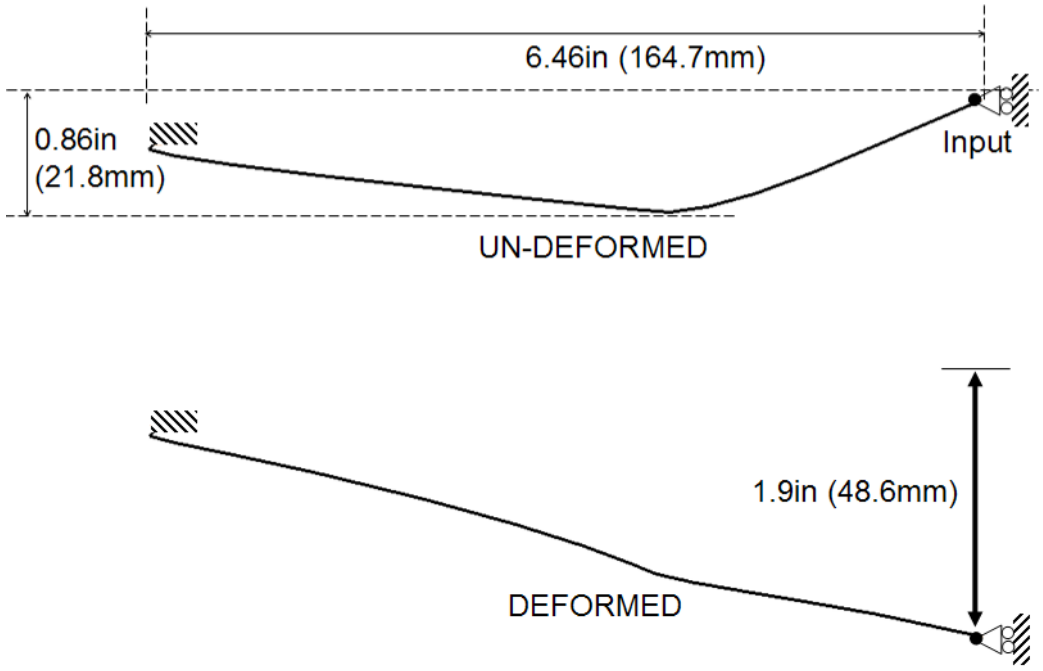

Figure 8-6: Generated nonlinear spring design in its un-deformed and deformed configuration.

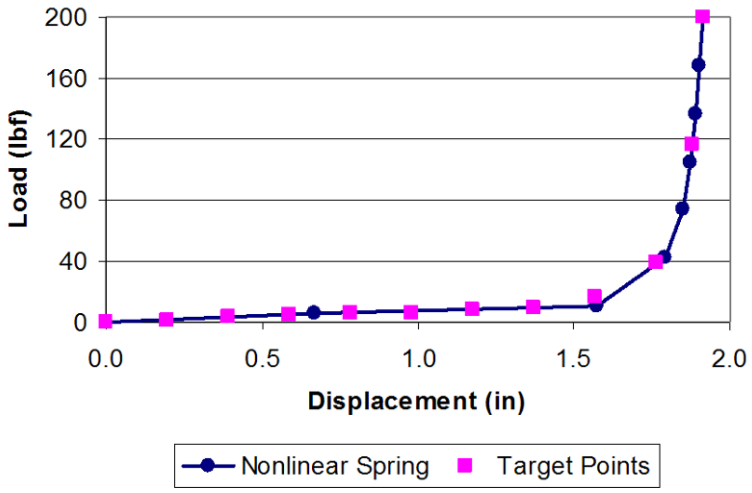

Figure 8-7: Load-displacement function for the generated spring design, (fixed arc-length = 0.06).

Prototype

The senior design team used the nonlinear spring design for their final prototype. Before fabricating the spring, the automotive company asked that the sharp bend near the fixed end of the spring be removed (see Figure 8-6). Using FEA, the senior design team determined that the removal of the bend, essentially 2 beam elements from the design, did not significantly affect the spring's overall performance or maximum stress. The spring's

final material was chosen as MartINsite M130 having a yield point of 135 ksi (930 MPa), resulting in a safety factor of approximately 1.5.

Figure 8-8 shows the final assembly. The connecting plate and anti-submarine feature was fabricated from 7-gauge and 20-gauge steel plates, respectively. The connecting plate and nonlinear springs were hinged together using piano hinges. The support cross bars were fabricated from 1 inch square, 11-gauge steel tubing. The nonlinear springs were fabricated by an outside source using a temporary dye. Figure 8-9 shows the final prototype without the foam cushion (Knauf et al., 2006).

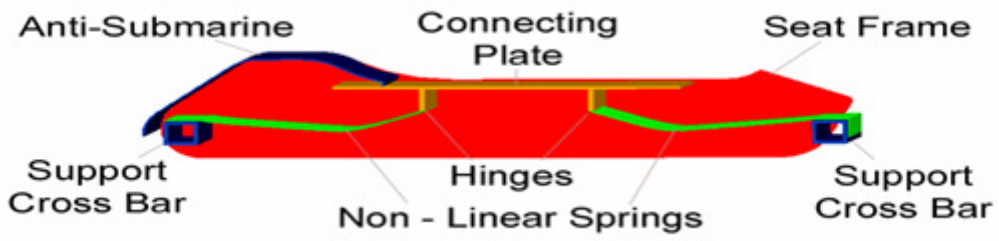

(Knauf et al., 2006)

Figure 8-8: Final design assembly without the foam cushion. A side, section view of the seat.

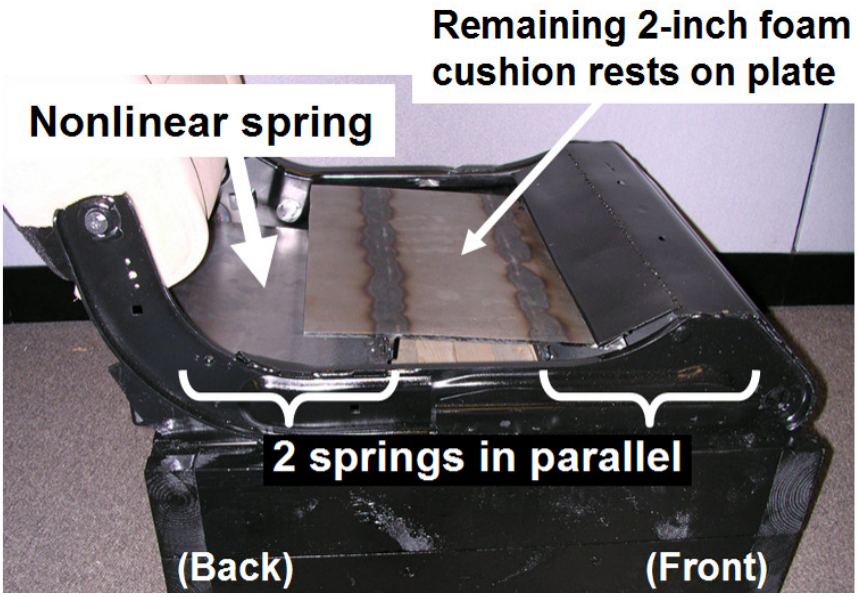

Figure 8-9: Final prototype without the foam seat cushion and covering.

Validation

To validate the prototype's load-displacement response, the team loaded the nonlinear spring assembly using an Instron 8516. Figure 8-10 shows the results of two tests. Both tests closely matched the automotive company's prescribed nonlinear data. Discrepancies between the empirical data and theoretical data are discussed in the next section. To validate the response of the entire assembly, the team added the 2-inch foam cushion and ran another test. The results in Figure 8-11 show that the total assembly matches the prescribed data even better (Knauf et al., 2006). Originally, the team assumed the 2-inch foam cushion and the nonlinear spring assembly would displace the same amount under the applied load. However, the results in Figure 8-11 suggest that the cushion is slightly more compliant than the nonlinear spring assembly since the cushion's addition decreased the error between the empirical data and the automotive company's data.

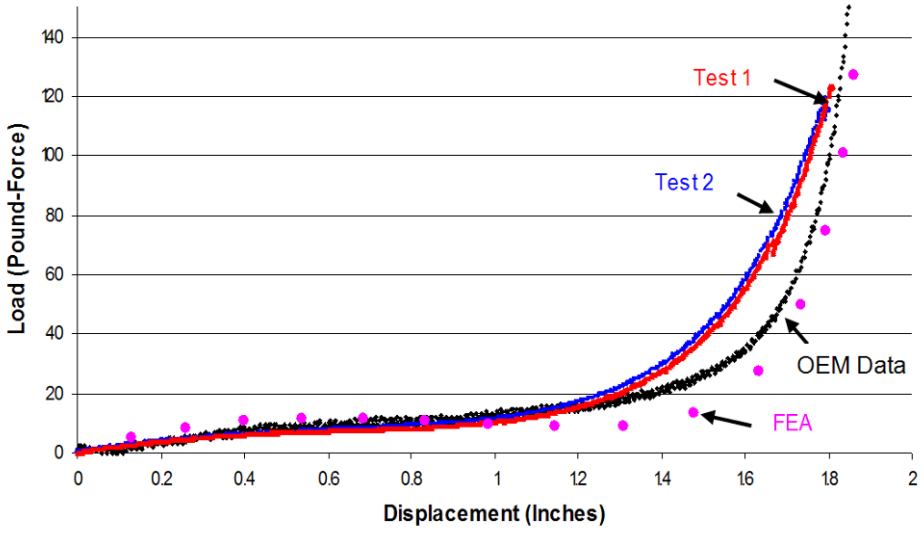

(Knauf et al., 2006)

Figure 8-10: Instron 8516 test data of the seat assembly without the foam.

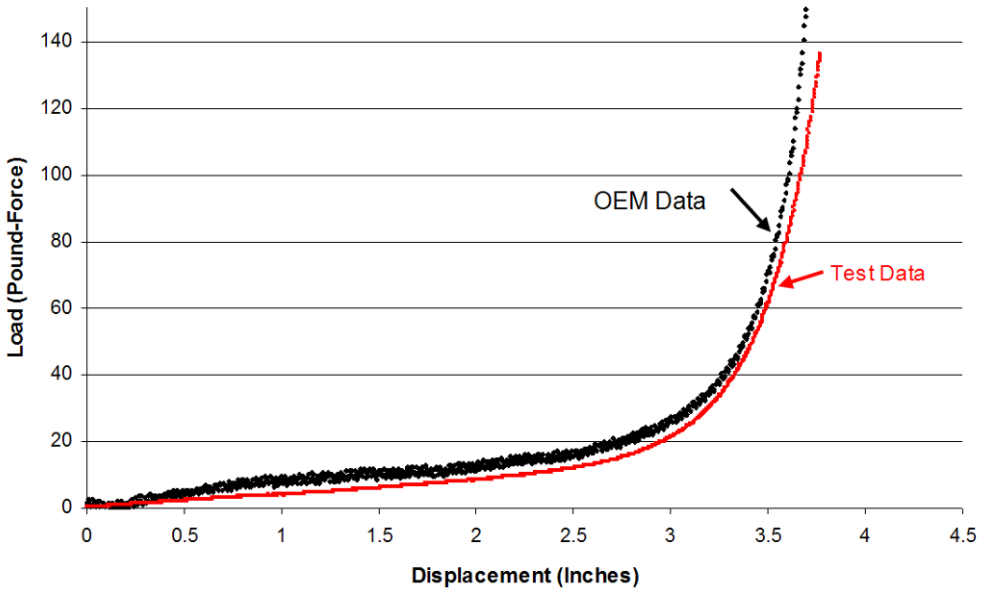

(Knauf et al., 2006)

Figure 8-11: Instron 8516 test data of the seat assembly with the foam.

Discussion of Results

When reviewing the team's semester report, I noticed that their FEA data in Figure 8-10 had a slight negative slope. The team was not aware that negative slopes signified buckling; however, this data compelled me to reexamine the original spring for buckling. I found that the original design's system matrix indeed had negative eigenvalues, even though the slope buckling constraint was satisfied. Wondering whether the analysis "missed" a negative slope, I refined the fixed incremental arc-length to 0.04 from 0.06. This way, the FEA solved for more points along the spring's load-displacement curve. Figure 8-12 reveals that the refined load-displacement function indeed has a slight negative slope. The markers along the load-displacement curve depict the solved equilibrium points. A fixed incremental arc-length of 0.06 was originally chosen because it had been sufficient for many other spring analyzes. However, it proved to be insufficient in this case. This example emphasizes the importance of verifying whether a design has negative eigenvalues in its system matrix. A smaller arc-length value also increases the chances for detecting negative slopes; however, it adds computational time to the analysis since more equilibrium points need to be solved.

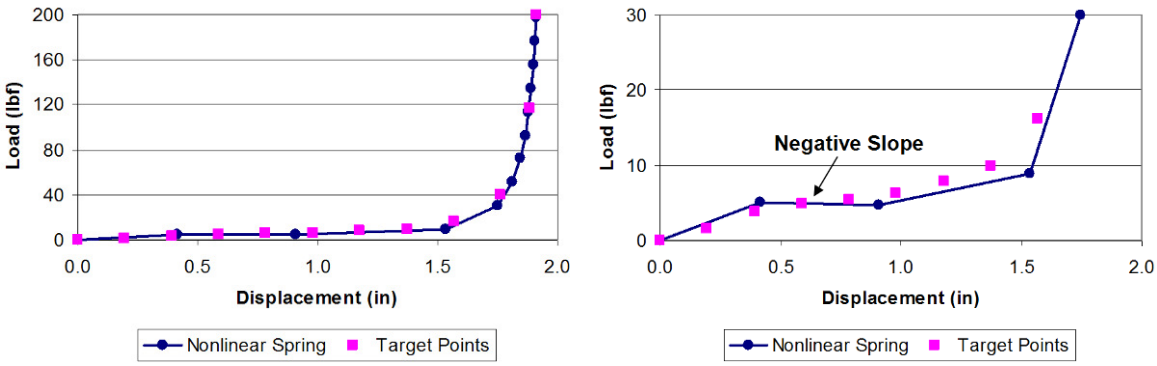

(a) (b)

Figure 8-12: (a) Load-displacement function of the final spring design, (fixed arc-length = 0.04). (b) Same as (a) only closer view.

Despite the negative slope in the team's analysis of the final spring design, the experimental results do not indicate buckling in Figure 8-10. Therefore, I further investigated the final design to determine whether fabrication inconsistencies led to the experimental response. Notice that in Figure 8-10 the experimental response not only depicts a continuous positive slope, but it also displaces less than predicted.

Figure 8-13 illustrates various modifications made to the finite element model. In Figure 8-13(a), the spring's fixed end point was changed to a pin joint, assuming the fabricated boundary conditions did not perfectly fix the ends. In Figure 8-13(b) and Figure 8-13(c), the spring's length was essentially shortened assuming that the spring would be less likely to buckle having less material to compress between the input and fixed point. In Figure 8-13(b), the spring's span in the y-direction was decreased by 10% keeping the same distance between the input and fixed point. In Figure 8-13(c), the bend was modified to make it less pronounced. In all three cases, the modifications to the finite element model did not match the experimental response.

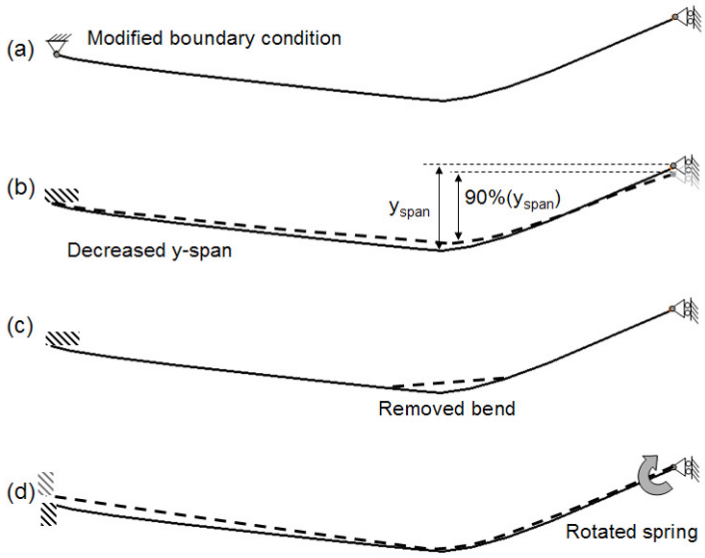

Figure 8-13: Possible fabrication errors that were analyzed using nonlinear finite element analysis.

Next, assuming that the spring was formed correctly and that the boundary conditions matched those in the finite element model, alignment flaws were checked. After various studies, it was discovered that a two degree rotation of the spring in the clockwise direction eliminated buckling (no negative eigenvalues) and also decreased the spring's total displacement. The resulting load-displacement function for the model in Figure 8-13(d) is shown in Figure 8-14. It is not a perfect match with the experimental results in Figure 8-10; however, it does imply that the buckling within the final spring design is so slight, that small inconsistencies within the fabricated design can remove the buckling. Other possible fabrication flaws, not analyzed by FEA, include (i) a tilting of the connecting plate, such that the horizontal distance between the springs' is decreased, creating tension in the spring designs or (ii) friction within the rotational joint at the input inducing unexpected moments on the spring.

As a final note, any nonlinear spring designed to match the automotive company's load-displacement function will be sensitive to buckling. As illustrated in Figure 8-2, the slight slope requires the nonlinear spring to remain on the verge of buckling for over two-thirds of the total displacement. Fortunately, foam does not buckle; however, when designing and manufacturing an *equivalent* spring, extra precaution must to be made to ensure stability.

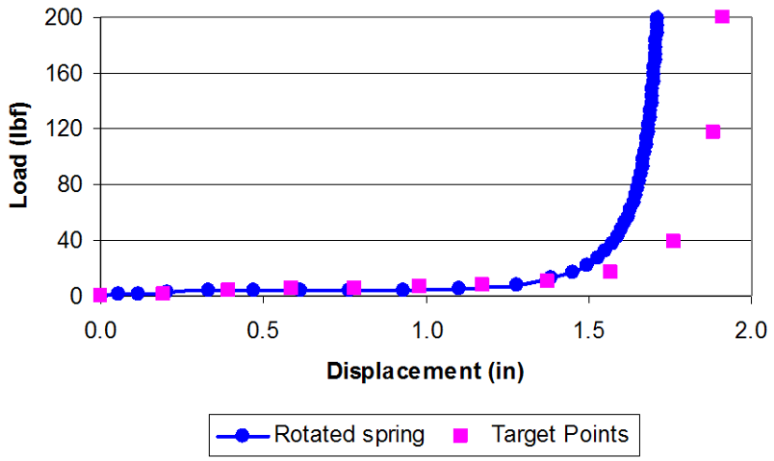

Figure 8-14: Load-displacement function of the final spring design rotated two degrees clockwise.

8.1.4 Closure

By employing nonlinear springs, the automotive company's seat cushion specifications were met by only using 2-inches of foam. Although the prescribed load-displacement function was sensitive to buckling, the design and testing of the seat cushion's nonlinear spring affirms the effectiveness of the nonlinear spring synthesis methodology in closely matching a prescribed nonlinear response. For designs on the verge of buckling, the system matrix must be checked for negative eigenvalues and manufactured springs must be verified for stability.

To further simplify the design and mass-produce the assembly, the senior design team made the following recommendations:

1) Stamp the nonlinear springs using a permanent dye
2) Change the connecting plate's material to a lightweight, high-strength composite
3) Integrate the hinges into the connecting plate's design
4) Integrate the support bars into either (i) the seat frame or (ii) the nonlinear spring via a modified stamping process. (Knaft et al., 2006)

8.2 Constant-force Spring

A constant-force spring design was fabricated and tested for its nonlinear response. Unlike the previous seat cushion spring which has a hardening behavior, a constant-force spring has a *softening* behavior. Figure 8-15 shows the spring design chosen for this test. It is a scaled version of an existing constant-force spring design generated within this work. The design was scaled to enlarge the in-plane thickness for manufacturing purposes. The following lists the properties of the spring: Material: Titanium alloy, Ti-6Al-4V (E=115GPa), Load-range: 10.2N (2.29lbf), Displacement-range: 57.7mm (2.27in), In-plane thickness: 1.14mm (0.045in), and Out-of-plane thickness: 4.76mm (3/16in). The maximum stress found by the FEA was 683MPa, well below the yield point of 830MPa. The spring was cut out of a 4.76mm (3/16in) titanium sheet using wire electrical discharge machining.

The simplicity of this spring design makes it versatile to a wide variety of constant-force spring applications. For example, Figure 8-16 and Figure 8-17 utilize springs in parallel to create two different constant-force connectors. The first arrangement applies to connectors under tension loads, while the second applies to connectors under compression loads. The latter design is employable as a coupling device between a machine and its end-effector. It applies a constant-force over varying displacements and is relevant to wear testing and glass pane scoring (Howell, 2001).

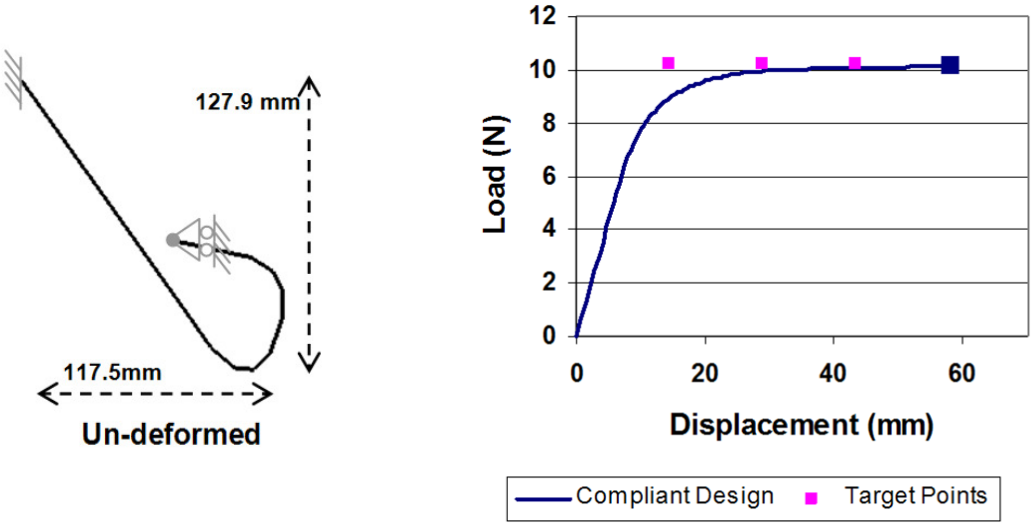

(a) (b)

Figure 8-15: (a) Constant-force spring design, (b) Load-displacement function determined by FEA.

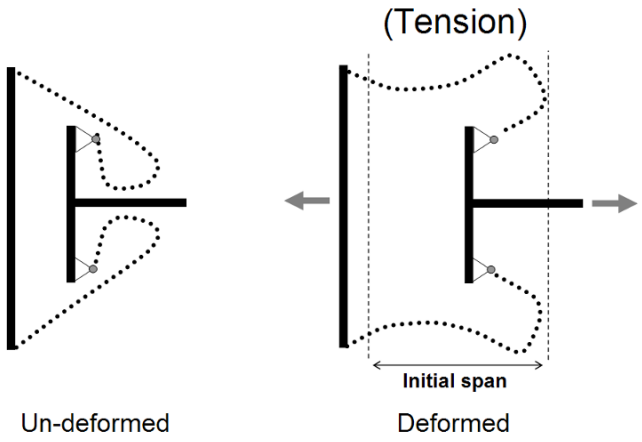

Figure 8-16: Constant-force connector for tension loads. (Springs are dotted.)

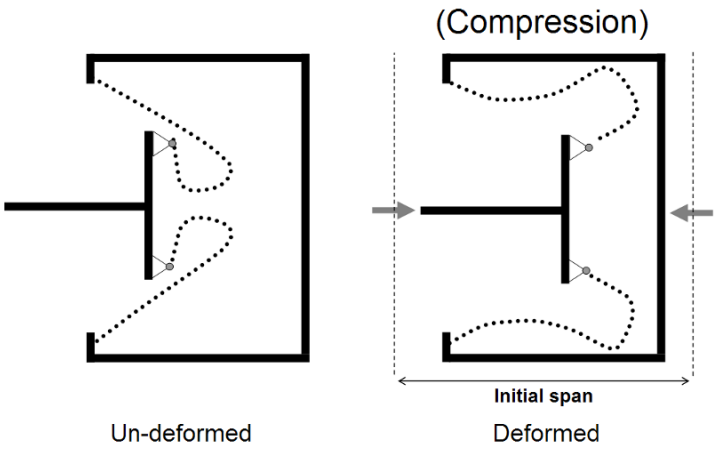

Figure 8-17: Constant-force connector for compression loads. (Springs are dotted.)

8.2.1 Test Assembly

Figure 8-18 illustrates the test assembly for the constant-force spring. The spring's fixed end was fastened with two bolts (Figure 8-19(a)). The spring's input was constrained along a single line of translation using a slider and rail assembly. To allow free rotation at the input, a shoulder bolt was passed though the spring's input and fastened to the slider (Figure 8-19(b)). Graphite was used as a lubricant. Washers functioned as spacers enabling the string to attach at equal distances above and below the spring, forcing the resultant load from the string to pass though the center of the spring's out-of-plane thickness. The string was 53.3N (12lb) braided nylon fishing line, and the

force gauge was a 49.0N (11lb) electronic hanging scale. A millimeter scale was attached at the input to measure the spring's displacement.

A series of turnbuckles (Figure 8-20) connected the force gauge's hook to a fixed point. For each data point, the turnbuckles were adjusted (lengthened or shortened) until the spring deformed to a prescribed distance. When the spring reached a target distance, the resultant load was recorded from the force gauge while the turnbuckle assembly maintained the target displacement.

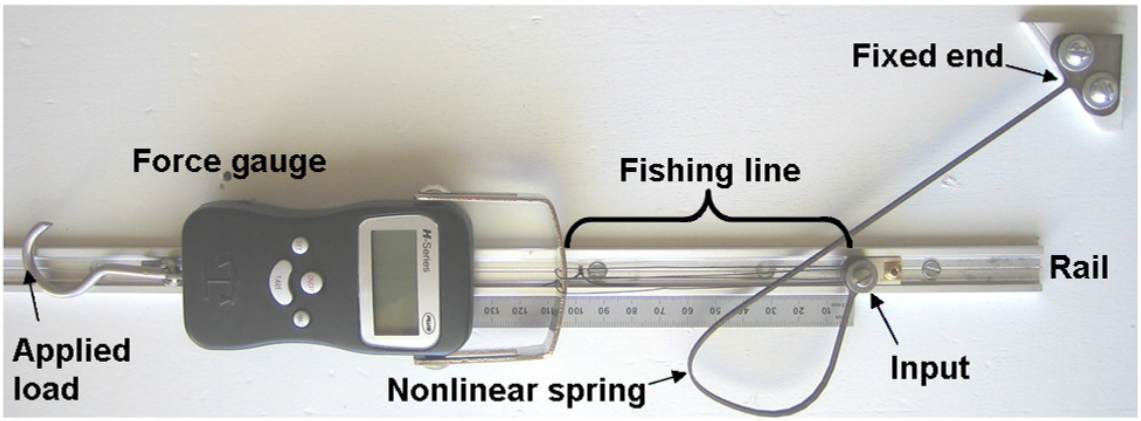

Figure 8-18: Test assembly.

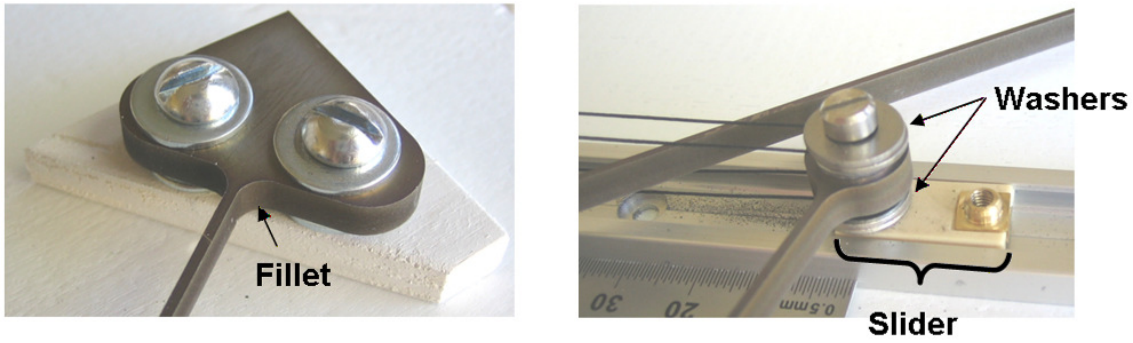

(a) (b)

Figure 8-19: Boundary conditions of the test assembly: (a) fixed end and (b) input with a slider and pin joint.

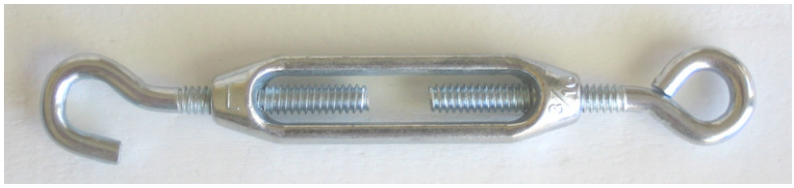

Figure 8-20: A turnbuckle used to control the displacement of the input.

8.2.2 Results

The comparison of Figure 8-21 and Figure 8-22 shows that the spring deformed as predicted by the FEA. The spring's resultant load was recorded for every 5mm of displacement over a 60mm displacement range. Four separate data sets were recorded and averaged. Figure 8-23(a) compares the design's FEA results with the averaged empirical results. The physical spring's shape function reveals a constant-force response; however, its load magnitude is 15% lower than predicted. The maximum load for the FEA is 10.2N, whereas the physical spring's maximum load is 8.7N.

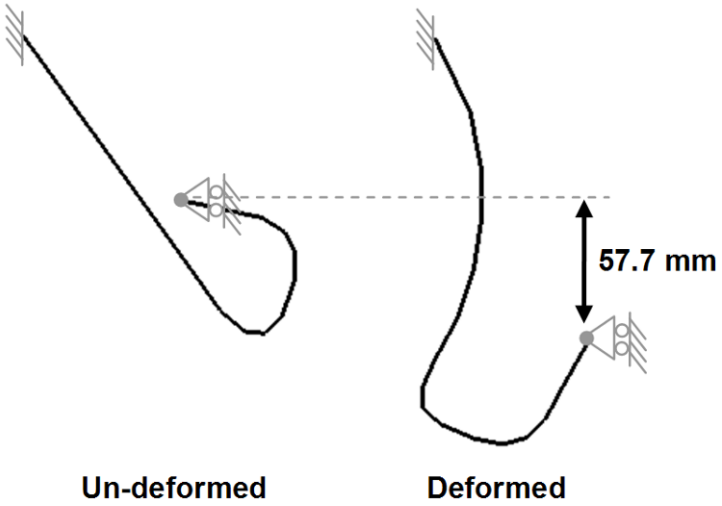

Figure 8-21: FEA prediction of deformation.

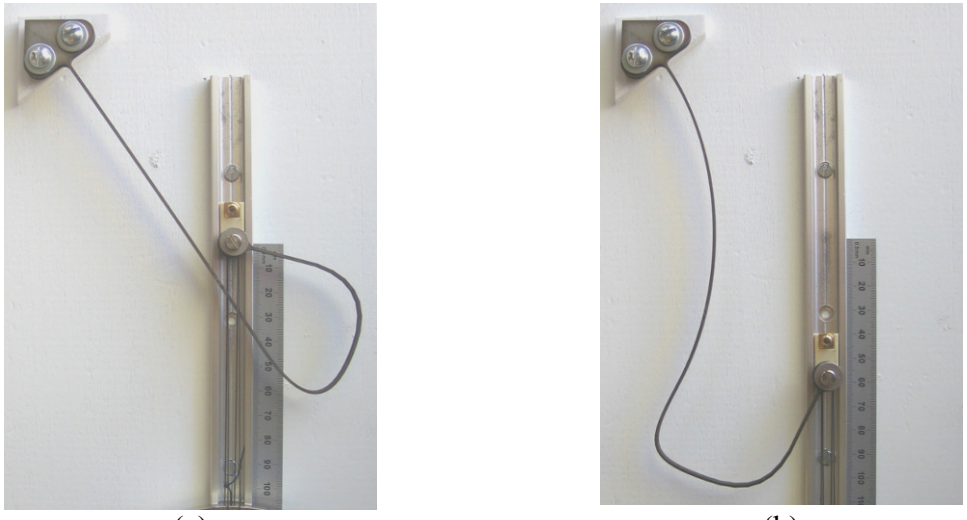

(a) (b)

Figure 8-22: Deformation of prototype: (a) un-deformed and (b) deformed.

To explain this discrepancy in load, several features of the test assembly were checked, including the force gauge, boundary conditions, and the fillet at the fixed end of the spring. None of these conditions greatly influenced the spring's load-range. Therefore, the spring's in-plane thickness was investigated for manufacturing inconstancies. Based on scaling rules, a slight difference in in-plane thickness (0.06mm (0.002in)) accounts for a 15% decrease in the load-range. Figure 8-23(b) verifies this by plotting the FEA results for a model with a 1.08mm (0.043in) in-plane thickness dimension instead of the original 1.14mm (0.045in) thickness. The FEA plot and the experimental data closely match. As with all manufactured products, it may take a few iterations before the manufacturing process is adjusted to cut the appropriate dimensions.

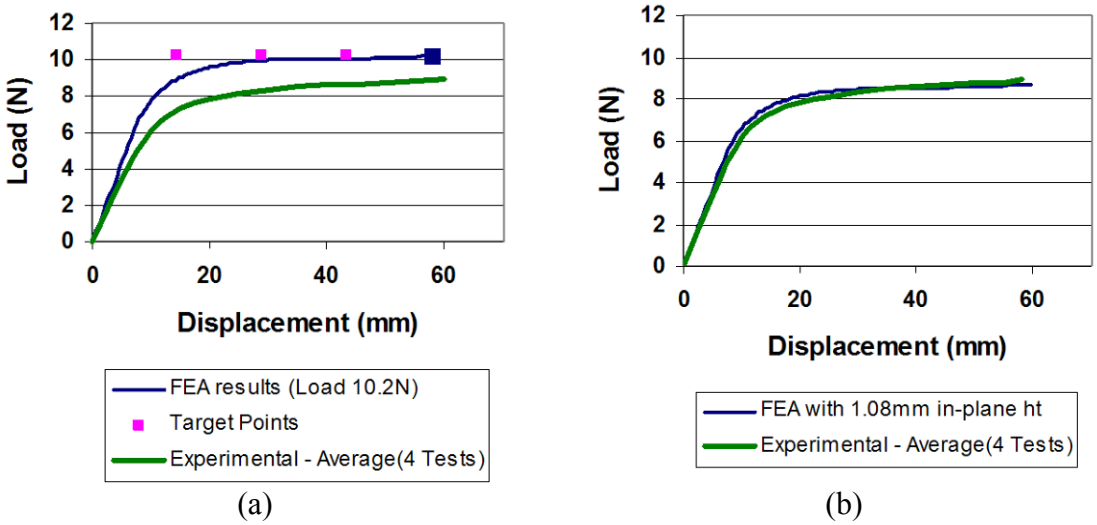

Figure 8-23: Load-displacement plots. (a) Comparison of FEA to experimental. (b) Comparison of the experimental data to FEA data where the FEA model has a reduction of in-plane thickness, 1.08mm from 1.14mm (difference = 0.06mm = 0.002in).

8.2.3 Closure

The prototype validated the FEA prediction of the nonlinear spring's constant-force response, deformation, and displacement-range. The majority of the 15% error in load-range is believed to be due to the load-range's sensitivity to the spring's in-plane thickness dimension. This sensitivity (cubed relationship) was established in the load-range scaling rules in Chapter 7. Designers must be aware of this sensitivity, and if possible, either optimize spring designs for larger in-plane thicknesses, such that the final

designs are less sensitive to manufacturing errors, or form springs from strips of metal whose thickness already meets tight manufacturing tolerances.

CHAPTER 9

EXTENSIONS OF THE METHODOLOGY

This chapter first explores two extensions of the current nonlinear spring synthesis methodology. The first investigation considers the generation of nonlinear springs having prescribed load-displacement functions in two directions. These springs are defined as anisotropic springs. The second investigation proposes a mechanism design parameterization using a network of splines. Both investigations are supported with design examples and a discussion of results.

This chapter concludes with an overview of manufacturing opportunities available for nonlinear springs with a particular focus on the less traditional meso-scale fabrication techniques. The feasibility and challenges of these manufacturing options are highlighted.

9.1 Anisotropic Springs

The examples presented for the generalized synthesis methodology have generated uniaxial nonlinear springs, i.e. springs with a nonlinear response in one direction. Springs having specified responses in different directions more closely match the properties of anisotropic materials, and thus, have the potential to synthesize structures that respond like anisotropic materials. For this reason, the springs generated in this section are referred to as anisotropic springs, as they are designed for prescribed responses in two different directions.

Three examples are presented to demonstrate the methodology's ability to generate anisotropic springs. Table 9-1 delineates the objective function for each of the three examples. The first example prescribes an S-curve in the -Y-direction while *maximizing* the stiffness in the X-direction. The second prescribes an S-curve in the -Y-direction while *minimizing* the stiffness in the X-direction. In both examples, the X-

direction is not specified as being positive or negative. Therefore, each spring design is analyzed first in the –Y-direction and then in both the positive and negative X-directions. The better of the two stiffnesses in the X-direction is evaluated in the objective function. The final example prescribes a J-curve in both the positive and negative Y-directions, such that each spring is analyzed in both directions.

Table 9-1: Objective functions for three different anisotropic spring examples.

Ex.	(A) -Y translation	(B) +Y translation	(C) X translation	Objective function
1	S-curve $(SFE+DP_{min}+BP_{slope})$	- -	Maximize stiffness $1/(max\ stiffness)*W_{stiff}$	$min(A+C)$
2	S-curve $(SFE+DP_{min}+BP_{slope})$	- -	Minimize stiffness $(min\ stiffness)*W_{stiff}$	$min(A+C)$
3	J-curve $(SFE+DP_{min}+BP_{slope})$	J-curve $(SFE+DP_{min}+BP_{slope})$	- -	$min(A+B)$

The three anisotropic spring examples began with the same problem setup parameters. The design space measured 90mm by 90mm with the input point located in the center. Each loading consisted of 10N with the input constrained in the direction perpendicular to the loading. Titanium was used as the material (E = 115 GPa). The maximum stress was constrained at or below the yield point at 830MPa. The beam element's out-of-plane thickness was set to 4mm, and the bounds on the in-plane thickness were set to 0.4-0.7mm. For the objective function, the minimum displacement percentage was 7.5% of the spring's footprint, the displacement penalty weight was 1, and the buckling penalty weight was 1000. Since these examples only serve for investigation purposes, the objective function did not include a prescribed displacement-range or a penalty for overlapping during deformation. For the optimization, each example problem had a population of 96 individuals with a 70% crossover rate and approximately a 3% mutation rate.

9.1.1 Example 1 - S-curve Spring (Y-translation), Stiff (X-translation)

After 30 generations, Figure 9-1 shows the generated anisotropic spring design in its un-deformed and deformed configurations. The corresponding load-displacement

functions for each of the loading conditions are illustrated in Figure 9-2. The load-displacement function in Figure 9-2(a) closely follows the S-curve target points, with a shape function error of 0.34%, while the stiffness was maximized to 1.47N/mm in the +X-direction. Both the displacement and buckling constraints were satisfied, including a negative eigenvalue check. The design's geometry and resulting stresses are provided in Table 9-2 in Section 9.1.3.

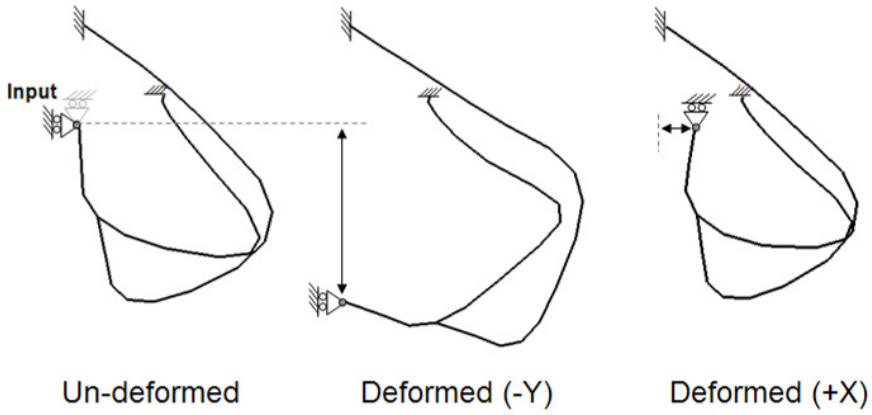

Figure 9-1: Configurations of the S-Stiff anisotropic spring.

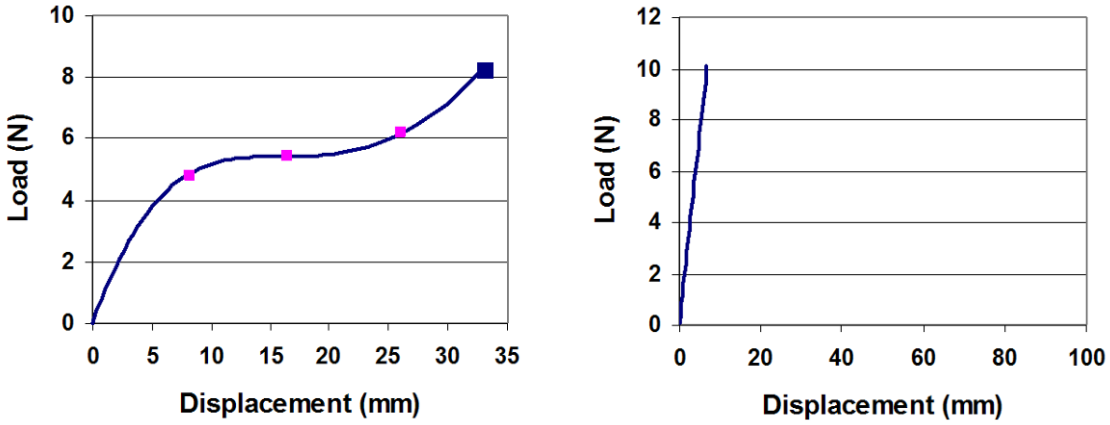

(a) (b)

Figure 9-2: Load-displacement functions for the S-Stiff anisotropic spring, (a) –Y translation, (b) +X translation.

9.1.2 Example 2 - S-curve Spring (Y-translation), Flexible (X-translation)

After 40 generations, Figure 9-3 shows the generated spring design in its un-deformed and deformed configurations. The corresponding load-displacement functions for each of the loading conditions are illustrated in Figure 9-4. The load-displacement

function in Figure 9-4(a) closely follows the S-curve target points, with a shape function error of 1.46%, while the stiffness was minimized to 0.06N/mm in the -X-direction. This stiffness is 24 times less than the stiffness in Example 1. Both the displacement and buckling constraints were satisfied, including a negative eigenvalue check. The design's geometry and resulting stresses are provided in Table 9-2 in Section 9.1.3.

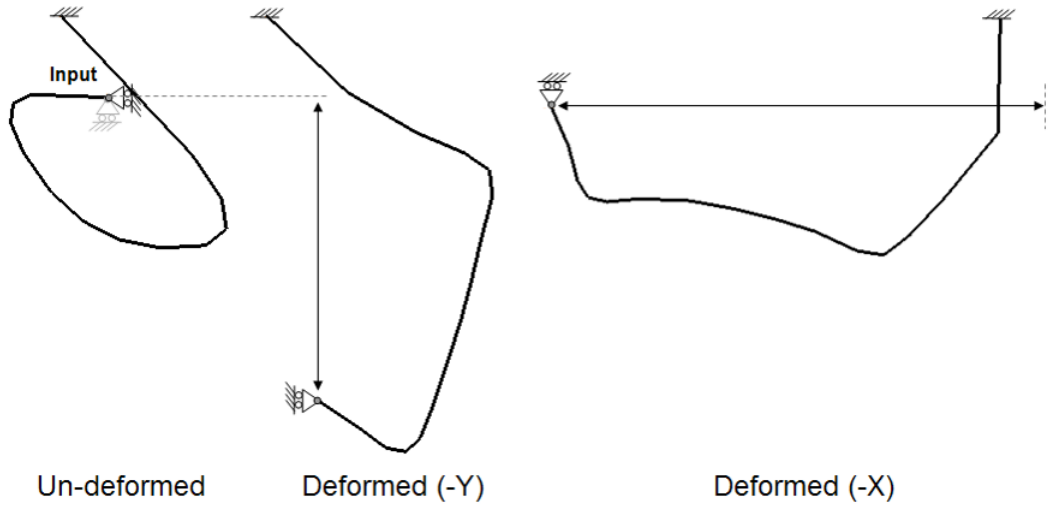

Figure 9-3: Configurations of the S-Flexible anisotropic spring.

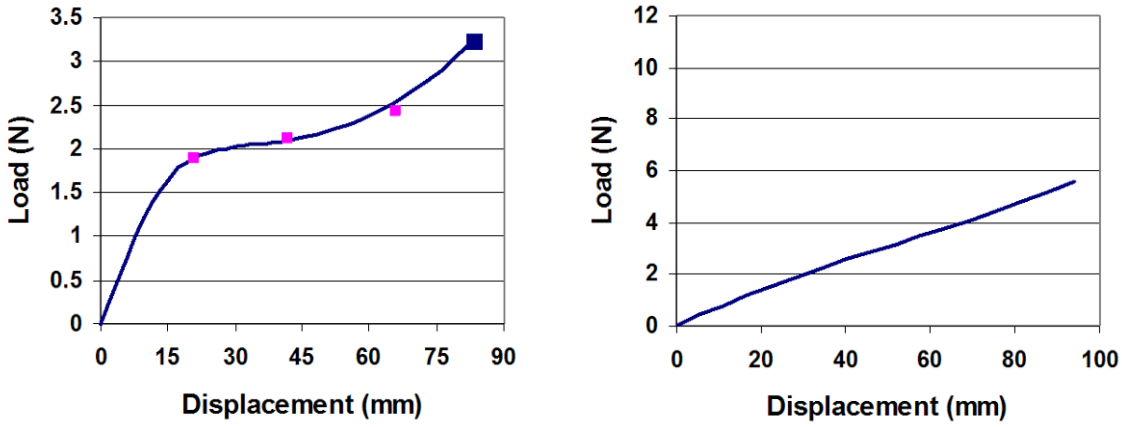

(a) (b)

Figure 9-4: Load-displacement functions for the S-Flexible anisotropic spring, (a) –Y translation, (b) -X translation.

9.1.3 Example 3 - J-curve Spring (+Y-translation), (-Y-translation)

After 40 generations, Figure 9-5 shows the generated spring design in its un-deformed and deformed configurations. This design has two splines with pinned and

fixed boundary conditions. The corresponding load-displacement functions for each of the loading conditions are illustrated in Figure 9-6. The shape function error for the J-curve in the –Y-direction is 2.97%, while the shape function error in the +Y-direction is 0.92%. Both the displacement and buckling constraints were satisfied, including a negative eigenvalue check. The design's geometry and resulting stresses are provided in Table 9-2.

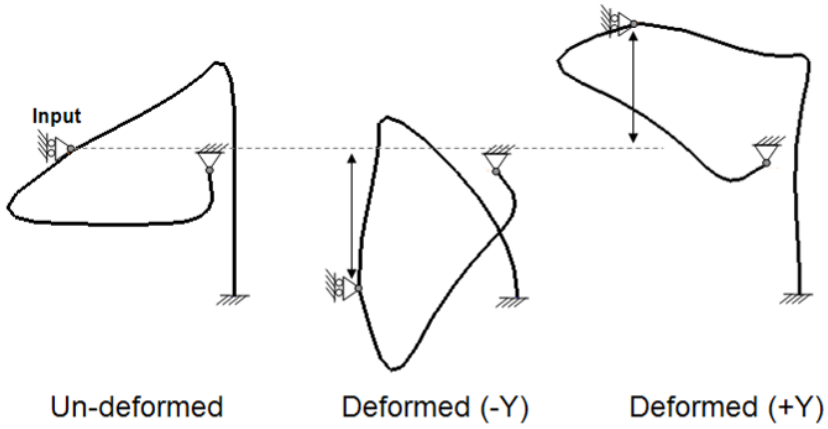

Figure 9-5: Configurations of the J-J anisotropic spring.

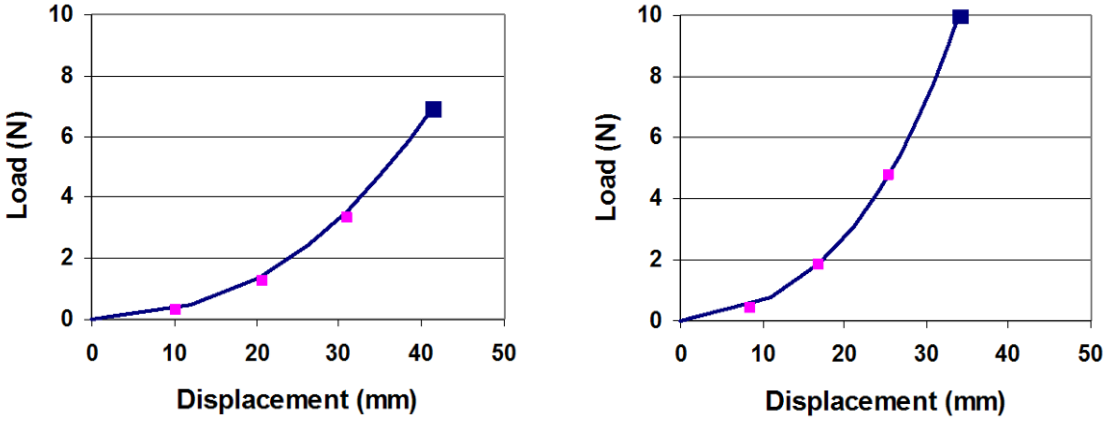

Figure 9-6: Load-displacement functions for the J-J anisotropic spring, (a) –Y translation, (b) +Y translation.

Table 9-2: Geometry and stress values for the three example problems.

	Footprint (mm)		In-plane thickness (mm)	Maximum stress (MPa)	
Example	x	y		-Y Direction	Other Direction
1- S, Stiff	36.9	53.2	0.67	830	531
2- S, Flexible	60.2	65.8	0.58	830	830
3- J,J	63.8	66.8	0.50	830	722

9.1.4 Discussion

The three example problems indicate that the nonlinear spring design parameterization is suitable for generating spring designs that match prescribed responses in two different directions. Examples 1 and 2 show that an S-curve spring can be generated to be either stiff or flexible in the perpendicular X-direction. Example 3 demonstrates that a spring can be generated to have the same shape function (J-curve) in opposite directions along one axis. Applications for anisotropic springs may have different boundary conditions than the ones imposed in these examples. Further investigations could determine the methodology's performance under different sets of boundary conditions.

The overall computational time for generating anisotropic springs is approximately N times greater than uniaxial springs, where N represents the number of directions that are analyzed per spring. Examples 1 and 2 analyzed three directions, -Y, -X, and +X. By eliminating the analysis in either the +X or –X direction, the computational time per spring would be reduced, but the optimization may require more iterations to achieve a satisfactory design. To minimize overall computational time, this trade-off should be further investigated.

9.2 Design Parameterization for Compliant Mechanisms

The section proposes and investigates a compliant mechanism design parameterization based on the nonlinear spring parameterization comprising splines. In developing the parameterization, the first task was to identify a generalized spline arrangement that could represent mechanism designs. Figure 9-7(a-c) illustrate three different compliant mechanisms: an amplifying mechanism (Hetrick, 1999), a path

generating mechanism (Rai et al., 2006), and a gripper mechanism (Lu and Kota, 2006), respectively. These three topologies all have two attributes in common. First, a single path connects the input point and the output point. This path was defined by Lu and Kota (2006) as the load path. Second, the topology's remaining members branch off the load path. The spline representation provided to the right of each design in Figure 9-7(a-c) illustrates the load path (solid curve) and branching splines (dotted curves). As shown in Figure 9-7(b), some branching splines protrude from the endpoints of the load path (the input and output) while others protrude from intermediate points. Figure 9-7(d) illustrates a compliant mechanism (Kim, 2005) with two different load paths. The generalized spline representation is less transferrable to designs like these having multiple load paths. However, the goal here is not to represent existing designs, but to compose a design parameterization capable of generating mechanism designs. For this reason, the spline representations shown in Figure 9-7 were the basis for the compliant mechanism design parameterization described below.

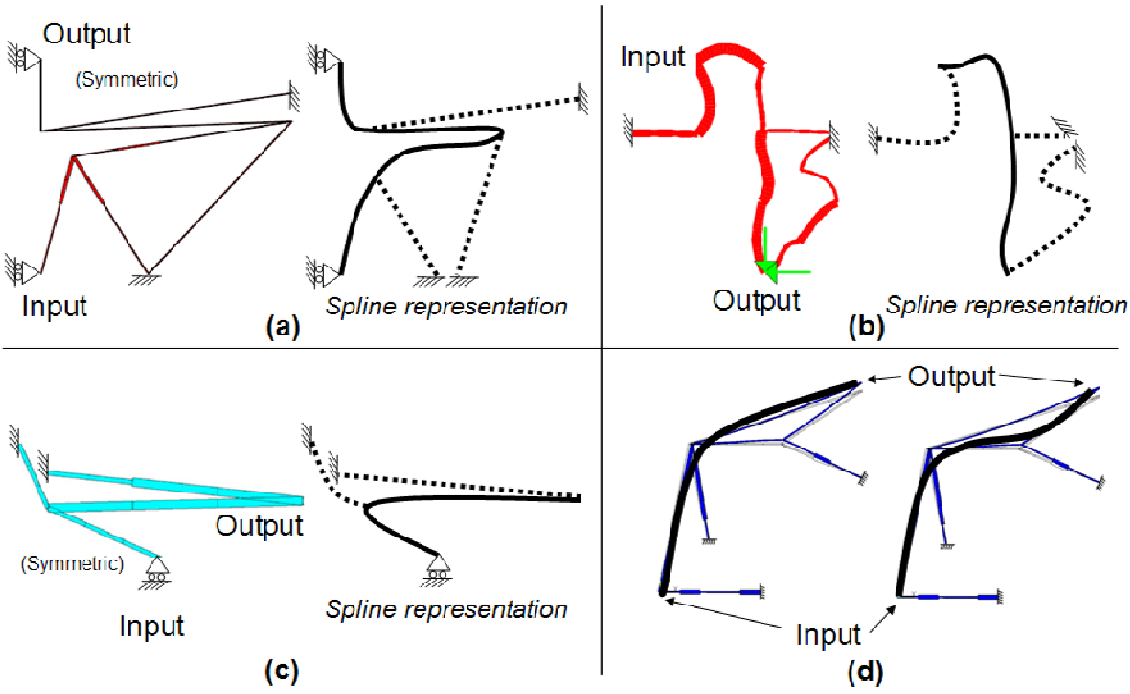

Figure 9-7: Existing compliant mechanism designs. (a-c) Compliant mechanism designs and their corresponding spline representations. (d) A compliant mechanism design having two load paths.

With a few modifications, the existing nonlinear spring parameterization of Figure 9-8(a) was converted to a compliant mechanism parameterization of Figure 9-8(b). First, the primary spline of Branch 1 in Figure 9-8(a) was redefined to represent a mechanism's load path, and its endpoint was converted to an output node. Then, Branch 3 was relocated to provide branching splines at the output node. Based on the spline representations in Figure 9-7, the secondary splines in Branch 2 and Branch 3 in Figure 9-8(b) may be unnecessary. To simplify the design parameterization, these splines were removed, leaving Figure 9-9(a) with only 4 branching splines: one at the input, one at the output, and two intermediate. Since spline representations of Figure 9-7 have relatively shorter branching splines compared to the length of the load path, an alternative design (Figure 9-9(b)) employs simplified branching splines having only 3 control points instead of 5. The following design examples utilize both design parameterizations in Figure 9-9. To ensure fully connected mechanisms, the load path and at least one branching spline is always constrained to be "on". Also, the spline endpoints are constrained to be fixed to ground to more closely match the boundary conditions of existing compliant mechanism designs.

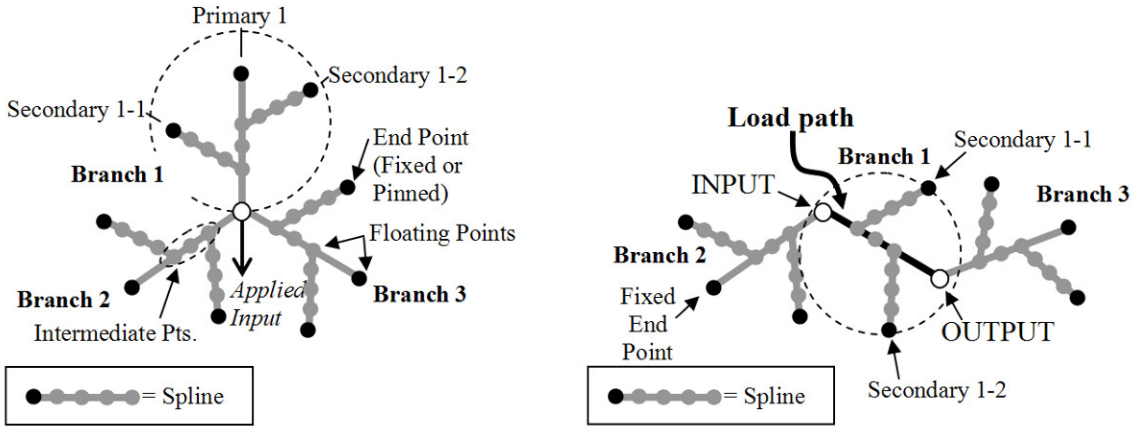

(a) Spring **(b) Mechanism**

Figure 9-8: Design parameterizations employing networks of splines.

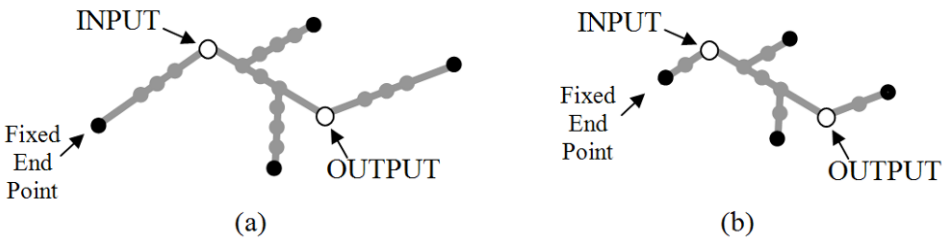

Figure 9-9: Simplified mechanism design parameterizations.

Three design examples are presented to demonstrate the performance of the proposed compliant mechanism design parameterization. To determine whether the parameterization is conducive to geometric nonlinearities, mechanisms are specified for a prescribed nonlinear velocity profile at the output, where the input is assumed to have a constant velocity. Due to the extreme geometric nonlinearities required of these mechanisms, their synthesis is yet to be explored in the compliant mechanism field. The design examples below, test a range of nonlinear velocity profiles (also defined as shape functions) shown in Figure 9-10. The first design example specifies the output point to accelerate by prescribing a J-curve relationship between the input and output displacements. The second example specifies the output point to decelerate by prescribing an inverse J-curve relationship between the displacements. Finally, the third example prescribes the output point to decelerate, dwell, and then accelerate, by prescribing an S-curve relationship between the input and output displacements.

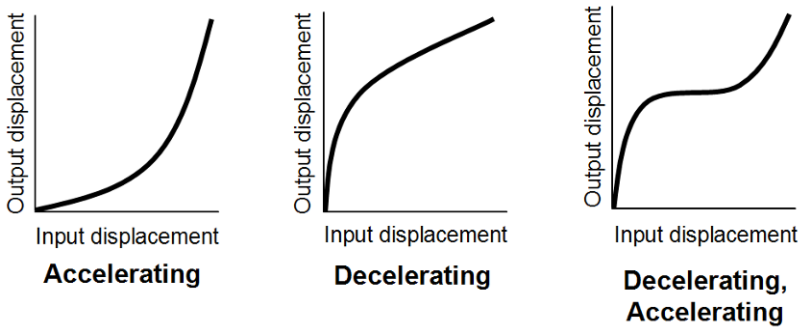

Figure 9-10: Three different nonlinear velocity profiles.

Figure 9-11 shows the design space used for all three examples. The input point is located in the lower left hand corner and constrained in both rotation and the horizontal

direction. A 30mm input displacement is applied to each design, and the subsequent evaluation occurs over the mechanism's elastic range. Similar to the spring problems, the output point is free to rotate but constrained along a single translational path. Since mechanisms are required to transmit force and motion, an external linear spring is included at the output to ensure a transfer of work. Without geometric nonlinearities, one might assume that each mechanism's output would decelerate as the spring compresses and increases its opposition to motion. The design examples below show otherwise.

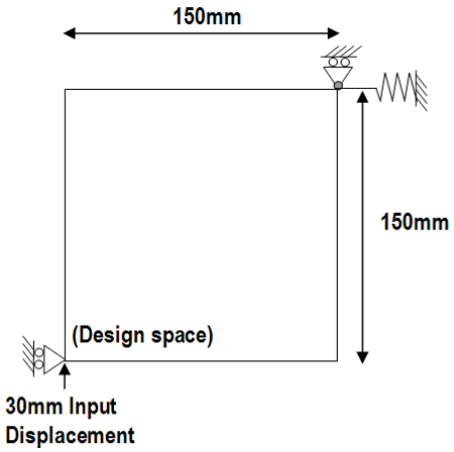

Figure 9-11: Design space used for the following three examples.

Table 9-3 delineates the design specifications for the three compliant mechanism design problems. The objective function formulation in Equation(4-2) includes the minimum displacement penalty, DP_{min}*, which was modified to penalize designs having negative displacements. The displacement penalty weight was 1, although designs with negative displacements were given a penalty value of 100. Buckling was checked in a post-processing step by noting the design's system matrix. For these preliminary investigations, splines were allowed to overlap in both the initial and deformed configurations. Each example below generated mechanism designs using the same optimization procedure employed for the nonlinear spring problem.

Table 9-3: Design specifications for three compliant mechanism design examples.

Output point	Accelerate	Decelerate	Decelerate, Dwell, Accelerate
Shape function	J-curve	Inverse J-curve	S-curve
Input displacement	30mm		
Minimum output disp.	10mm		
Spring stiffness	0.05 N/mm		
Material modulus (material)	2.0MPa (Nylon)	2.4MPa (Polycarbonate)	2.0MPa (Nylon)
Maximum stress (Safety factor)	35MPa (1.7)	60MPa (1)	35MPa (1.7)
Out-of-plane thickness	5mm		
In-plane thickness	2-5mm	1-4mm	2-5mm
Population size	96		
Crossover rate	70%		
Mutation rate	3%	9%	3%
Design parameterization	Figure 9-9(a)	Figure 9-9(b)	Figure 9-9(a)

$$Objective\ Function = min(SFE + DP_{min}^{*}) \tag{9-1}$$

9.2.1 Mechanism with Accelerating Output

This design example generates a mechanism whose output point accelerates while displacing. The employed design parameterization is found in Figure 9-9(a). An initial population of 96 designs was randomly created. The genetic algorithm then began to evaluate and create refined designs based on the objective function values. After 40 generations, the final design was retrieved.

Figure 9-12 shows the resulting output displacement versus input displacement plot for the accelerating mechanism. The plot closely follows the target values with a shape function error of 0.02%. The displacement and buckling constraints were satisfied. Figure 9-13 shows the resulting design in its un-deformed and deformed configurations. The topology has one branching spline at the input and another midway along the load path. Its uniform in-plane thickness is 3.78mm. Figure 9-14 illustrates the mechanism's stress distribution at the beams' edges. The maximum stress is 28MPa, roughly half the material's yield stress. By animating the design in the FEA post-processor, the acceleration of the output is visible. Initially, the mechanism undergoes much

deformation with very little displacement at the output. Eventually, the mechanism deforms into a configuration that is more effective in transmitting the input motion to the output.

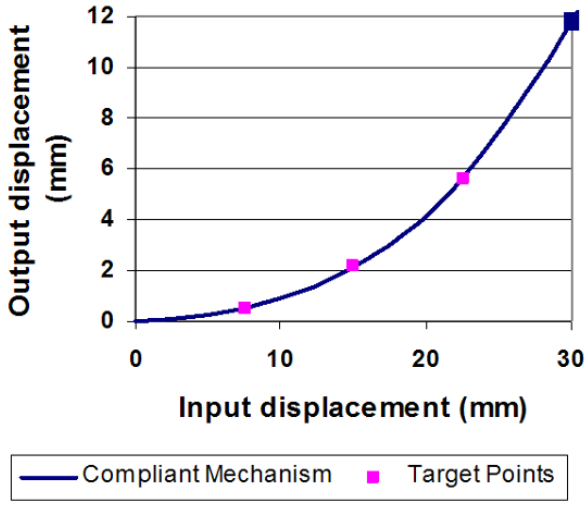

Figure 9-12: Output displacement vs. input displacement function for the compliant mechanism design with an accelerating output.

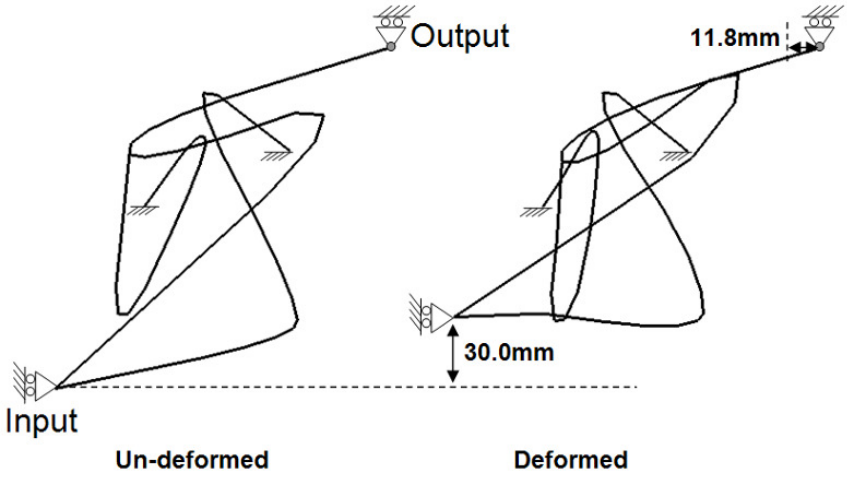

Figure 9-13: Accelerating output mechanism in its un-deformed and deformed configurations.

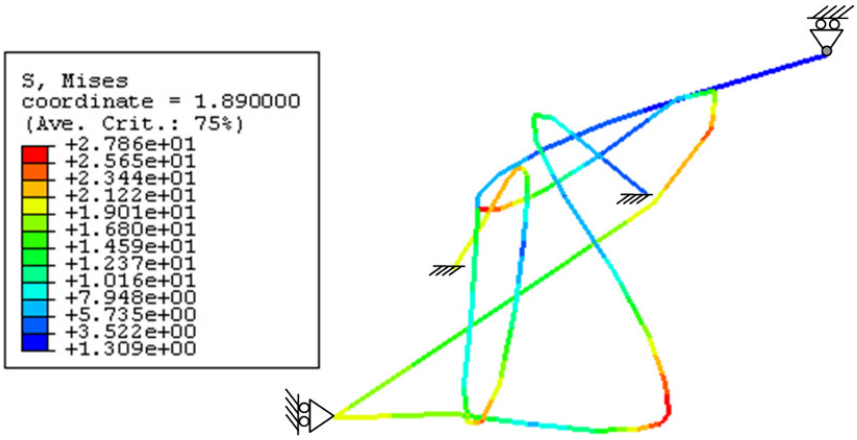

Figure 9-14: FEA stress contours for mechanism with accelerating output.

9.2.2 Mechanism with Decelerating Output

This design example generates a mechanism whose output point decelerates over its displacement. The employed design parameterization is found in Figure 9-9(b). After 60 generations, Figure 9-15 shows the resulting output displacement versus input displacement plot. The plot closely follows the target values with a shape function error of 1.04%. The displacement and buckling constraints were satisfied. Figure 9-16 shows the resulting design in its un-deformed and deformed configurations. Like the previous example, the topology has one branching spline at the input and another midway along the load path. Its uniform in-plane thickness is 1.0mm. Figure 9-17 illustrates the mechanism's stress distribution at the beams' edges. The maximum stress is 21MPa, roughly one-third the material's yield stress. By animating the design in the FEA post-processor, the deceleration of the output is visible. Initially, the mechanism is effective in transmitting the input displacement to the output displacement, but as the mechanism continues to deform, it becomes less effective in transmitting motion. This may be due to the load path beginning in a relatively straight configuration and ending in a bent one, as shown in Figure 9-16.

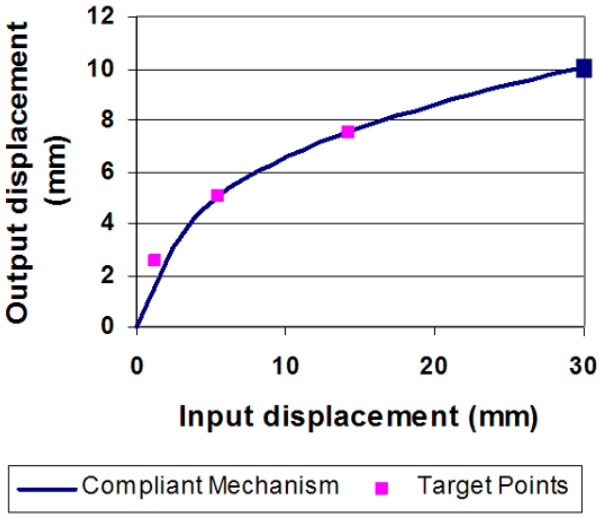

Figure 9-15: Output displacement vs. input displacement function for the compliant mechanism design with a decelerating output.

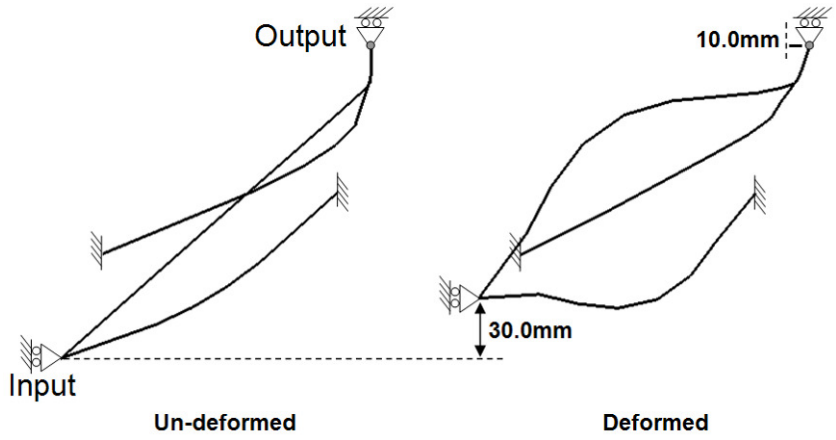

Figure 9-16: Decelerating output mechanism in its un-deformed and deformed configurations.

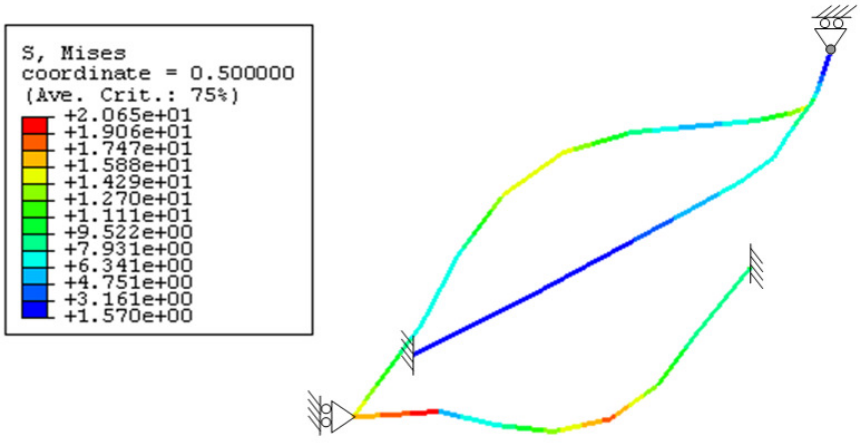

Figure 9-17: FEA stress contours for mechanism with decelerating output.

9.2.3 Mechanism with Output that Decelerates-Dwells-Accelerates

The final design example generates a mechanism whose output point decelerates, dwells, and then accelerates over its displacement. This prescribed behavior is the most nonlinear of the three examples. The employed design parameterization is the same as the first example. After 60 generations, Figure 9-18 shows the resulting output displacement versus input displacement plot. A portion of the plot has a negative slope. This does not signify buckling, since the plot is not a load-displacement plot; however, it reveals that this design's output displacement moves in the negative direction for a portion of its motion. Geometric nonlinearities indeed play a significant role by causing the output to move in two directions (both positive and negative), while the displacement at the input only moves in one direction (positive). This forward and backward output motion is clear in the FEA animation of the design.

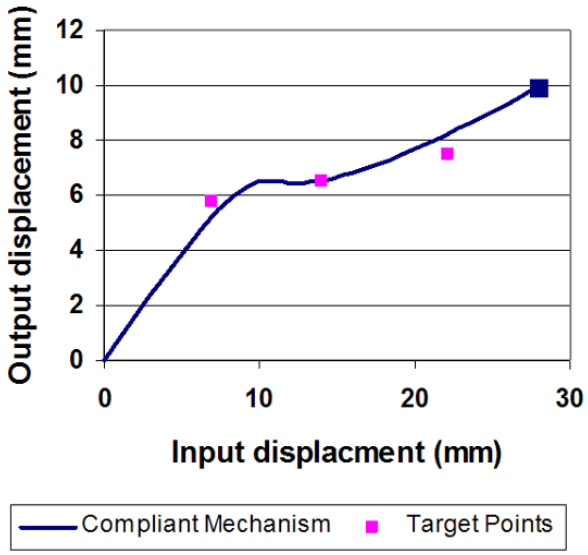

Figure 9-18: Output displacement vs. input displacement function for the compliant mechanism design with decelerating then accelerating output.

The resulting design's shape function error is 5.1%. Several trials were executed to improve the shape function error, but the decelerate-dwell-accelerate behavior proved difficult to generate. The displacement and buckling constraints were satisfied. Figure 9-19 shows the resulting design in its un-deformed and deformed configurations. This topology has one branching spline at the output and another midway along the load path. Its uniform in-plane thickness is 2.21mm.

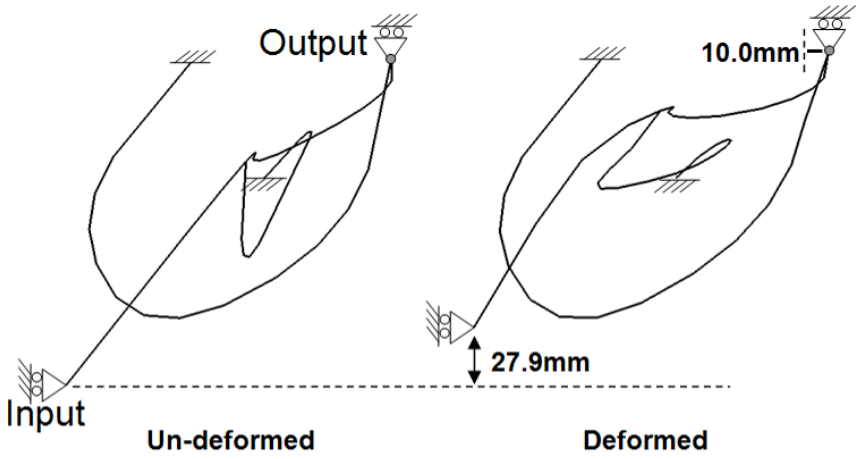

Figure 9-19: Final design in un-deformed and deformed configurations.

Figure 9-20 illustrates the mechanism's stress distribution at the beams' edges. The maximum stress is 35MPa, the limit stress for this problem. Spline #3 in Figure 9-20 indicates low stress. To simplify the design, this spline was removed from the topology, and the modified design in Figure 9-21(a) was reanalyzed with FEA. Figure 9-21(b) illustrates the resulting output displacement versus input displacement plot. The absence of spline #3 greatly hinders the nonlinearity of the mechanism's response. These results suggest that spline #1 and #2 have an antagonistic relationship with spline #3 in the original design. In general, spline #3 acts as an extension spring between its fixed point and the output. The shape function's negative slope near 10mm input displacement depicts instances where spline #3 is the dominant spline, forcing the output to move in the negative direction. This mechanism example offers insight into the design of highly nonlinear compliant mechanisms.

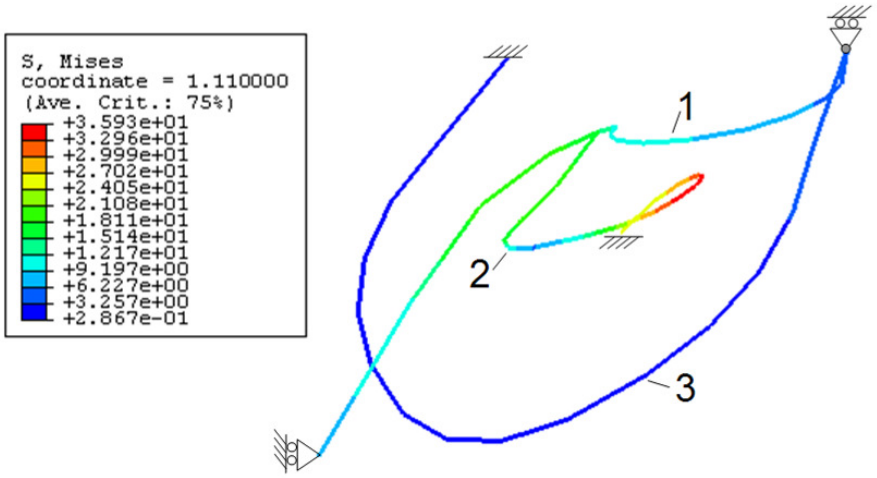

Figure 9-20: FEA stress contours for mechanism with decelerating then accelerating output.

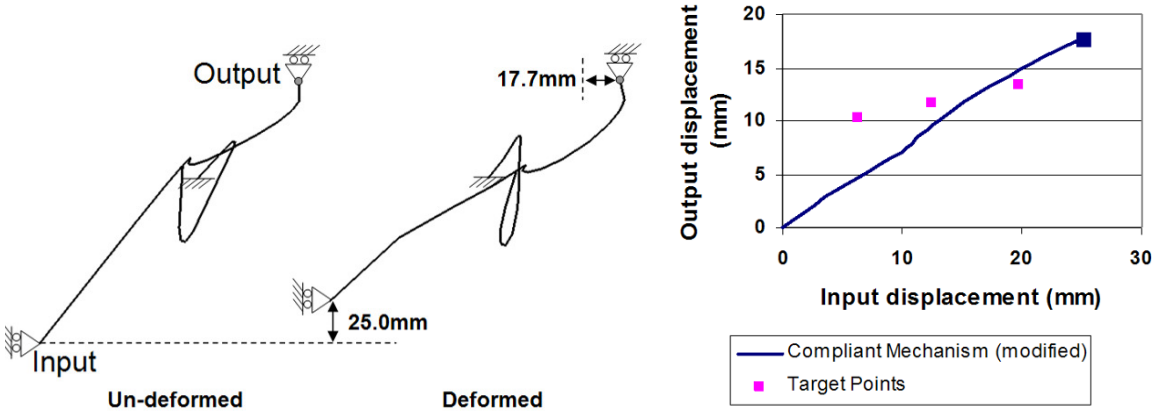

Figure 9-21: Modified compliant mechanism: (a) un-deformed and deformed configurations, (b) output displacement vs. input displacement function.

9.2.4 Discussion

These preliminary investigations confirm that geometric nonlinearities can produce nonlinear relationships between the input and output points of compliant mechanisms. When comparing the un-deformed and deformed configurations, large geometric nonlinearities are visible and greatly dependent on the long, slender curvilinear geometry. It is questionable whether typical compliant mechanism parameterizations, like homogenization or ground structure approaches, could produce such nonlinear mechanisms. The proposed parameterization could further improve by eliminating overlapping; however, this modification may weaken the optimization's performance since overlapping was a predominant feature of the three example problems. Since large

geometric nonlinearities require a significant level of compliance (i.e. energy storage), this parameterization works best for designs whose primary function is not energy transmission.

The proposed compliant mechanism design parameterization was successful in generating compliant mechanisms. The spline representations in Figure 9-7(a-c) illustrate how the parameterization can approximate existing compliant mechanism designs. At this point, more studies are needed to determine whether this parameterization outperforms the other existing compliant mechanism design parameterizations. Already, the parameterization offers two new benefits: simplified designs (a single load path) and smooth nonlinear geometries.

9.3 Manufacturing Opportunities

To meet the requirements of various spring applications, nonlinear springs must be manufacturable at the micro-, meso,- and macro-scales. On the macro-scale, conventional manufacturing methods provide various fabrication options for planar springs. Examples include stamping, injection molding, die casting, and forming. On the micro-scale, silicon based fabrication methods are well established and used for manufacturing MEMS devices; these methods have been successfully employed to fabricate planar compliant mechanisms used in MEMS applications (Kota et al., 2001). Meso-scale fabrication options along with non-silicon based micro-scale fabrication options are less traditional. The remainder of this section explores the manufacturing options available for meso-scale nonlinear springs (springs with roughly a one square centimeter footprint and micro-scale features).

Common examples of meso-scale fabrication technologies are available at Sandia National Laboratories. Engineers at Sandia define meso-machining processes as fabrication techniques that can create minimum feature sizes of 25 microns or less (Benavides et al., 2001). Table 9-4 provides a listing of the various meso-scale machining technologies at Sandia. The table depicts the minimum feature size, feature tolerance, positional tolerance of features, material removal rate, and compatible materials. The feature tolerance is dependent on the alignment of the tool within the machine, whereas the feature positional tolerance is dependent on the tool's alignment

with the workpiece. The data within the table is representative of the technologies across various manufacturers. Each technology is capable of creating features in at least two dimensions. Of the six machining processes listed, the first five are subtractive (material is removed) whereas the final process, LIGA, is additive (material is added) (Benavides et al., 2001).

Table 9-4: Meso-scale fabrication options available at Sandia National Laboratories (Benavides et al., 2001).

Technology / *Feature Geometry*	Minimum feature size / *Feature tolerance*	Feature positional tolerance	Material removal rate	Materials
Focused Ion Beam / *2D & 3D*	200 nanometers / *20 nanometers*	100 nanometers	.5 cubic microns/sec	Any
Micro milling or micro turning / *2D or 3D*	25 microns / *2 microns*	3 microns	10,400 cubic microns/sec	PMMA, Aluminum, Brass, mild steel
Excimer laser / *2D or 3D*	6 microns / *submicron*	submicron	40,000 cubic microns/sec	Polymers, ceramics and metals to a lesser degree
Femto-second laser / *2D or 3D*	1 micron / *submicron*	submicron	13,000 cubic microns/sec	Any
Micro-EDM (Sinker or Wire) / *2D or 3D*	25 microns / *3 microns*	3 microns	25 million cubic microns/sec	Conductive materials
LIGA / *2D*	submicron / *0.02um~ 0.5 um*	~0.3um nom. across 3"	N/A	Electroformable: copper, nickel, permalloy (see note)

Note: LIGA can also be used to fabricate parts in polymers, pressed powders, ceramics, and rare-earth magnets with a little degradation in machining performance specifications.

Focused Ion Beam (FIB) machining removes material by blasting gallium ions at the work piece. Compared to the other meso-scale machining options, this process has the most precision; however, it has a very low material removal rate. At Sandia, it is typically only employed for micro-tool fabrication. Micro-milling or micro-turning operations are similar to their macro-scale counterparts; however, their tool dimensions can be as small as 25 microns in diameter. Chips and burrs can be detrimental to the final work piece and thus must be minimized (Benavides et al., 2001).

Laser technology is also employed for meso-scale machining. To achieve clean, accurate cuts, thermal diffusion within the work piece is minimized by pulsing the laser. In Table 9-4 , the excimer laser has nanosecond pulse widths, whereas the fetmosecond

laser has pulse widths on the order of 10^{-15}, producing better results. Overall, the fetmosecond laser is powerful tool but a relatively new technology (Benavides et al., 2001). Figure 9-22 provides an example of a fetmosecond laser's capability; the part is made of out kovar and resting on a pencil eraser.

Figure 9-22: A part fabricated by a fetmosecond laser out of kovar (Precision Meso Manufacturing, 2008).

Like its macro-scale counterpart, micro-electro-discharge machining (micro-EDM) exploits the spark erosion process. The electrode can either be a wire (one-dimensional) or a sinker (multi-dimensional), where wire-EDM is more relevant to planar spring fabrication. Figure 9-23 shows a four bar flexure fabricated with micro-EDM. The flexure has roughly a one centimeter footprint and 50 micron features. Micro-EDM is a relatively mature form of meso-scale fabrication. Similar to laser machining, the heat affected zone must be minimized through an optimal choice of process parameters. To fabricate EDM sinkers, LIGA is often used. LIGA is an additive fabrication process that electroplates material within meso-scale molds (Benavides et al., 2001).

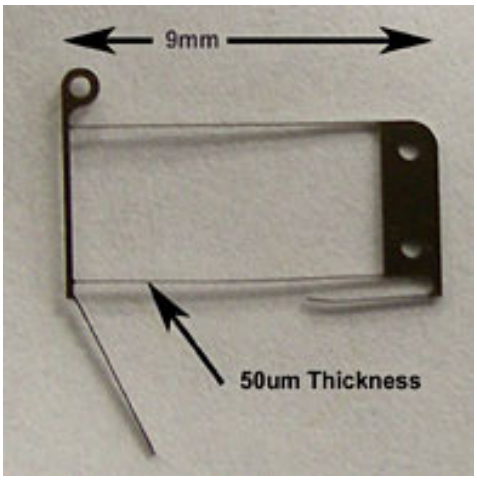

Figure 9-23: A four bar flexure fabricated by micro-EDM (Precision Meso Manufacturing, 2008).

Another meso-scale fabrication technology currently available at Sandia but not included in Table 9-4 is a Sony SCS-6000 High Resolution Stereolithography Apparatus. This machine uses an additive process to build polymer parts layer-by-layer, where the minimum feature dimensions are 75 microns wide and 50 microns tall (layer height) (Precision Meso Manufacturing, 2008).

Typical challenges relevant to meso-scale fabrication processes include cleanliness (the avoidance of dirt and debris), surface finish, and surface morphology. At the meso-scale, material instability can cause parts to warp as they relax after fabrication. Researchers at Sandia are currently compiling a list of stable materials including titanium and beryllium copper. Tool forces may also cause a part to warp. To continually improve the performance of these meso-scale manufacturing options, parametric studies are being conducted for various process settings on these machines (Benavides et al., 2001). Herrero et al. (2006) provides an overview of the current state-of-the-art and ongoing research activities in this area. One research lab, the Rapid Prototyping Laboratory at Stanford University led by Dr. Fritz Prinz, focuses primarily on nano- and micro-scale fabrication techniques; however, they do employ non-silicon based fabrication methods, including Focused Ion Beam milling (Rapid Prototyping Laboratory, 2008).

Microforming is an alternative approach to creating micro- and meso-scale components by using typical forming processes such as bending, forging, and blanking. Compared to the technologies mentioned above, the field of microforming is less developed. Geissdorfer et al. (2006) provides the current state-of-the-art in microforming and recommendations for future research activities.

CHAPTER 10

CONCLUSIONS AND FUTURE WORK

10.1 Conclusions

This dissertation presented a generalized nonlinear spring synthesis methodology for prescribed load-displacement functions. Four spring examples, J-curve, S-curve, constant-force, and linear, demonstrated the effectiveness of the methodology in generating planar spring designs having distributed compliance and matching desired load-displacement functions. Two fabricated designs validated nonlinear spring responses, while demonstrating the applicability of nonlinear springs. By examining various nonlinear spring designs, several interpretations were provided for how a spring's shape, topology, and loading (i.e. axial and bending) influence its response. Additional investigations offered spring scaling rules, guidelines for arranging nonlinear springs in series and parallel, insights into designing anisotropic springs, and a compliant mechanism parameterization based on the spring parameterization.

This is the first known attempt at developing a generalized nonlinear spring synthesis methodology. Previous research in compliant mechanism design has focused on large displacement *mechanisms* not *springs*. The spring design problem is a more constrained problem since a spring's load-displacement function defines its strain energy absorption rate, whereas a mechanism's strain energy absorption rate is an additional design degree of freedom. A few researchers have attempted the spring design problem but only for one particular load-displacement function and their resulting designs revealed lumped compliance.

10.1.1 Summary of Generalized Synthesis Methodology

Various aspects of the generalized synthesis methodology contributed to its ability in generating nonlinear spring designs. These aspects are highlighted below with respect to optimization, design parameterization, and implementation.

Optimization

The goal was to design planar nonlinear springs that meet designers' prescribed load-displacement functions and space, material, and stress constraints. By breaking down the load-displacement function into its three parameters, (i) shape function, (ii) load-range, and (iii) displacement-range, the objective function was formulated to focus primarily on the spring's nonlinearity (its shape function), while addressing the load-range and displacement-range requirements with either penalty constraints and/or scaling. Scaling proved to be a powerful tool in improving the performance of the optimization. It prevented the stress constraint from becoming an extra term in the objective function. This was accomplished by evaluating spring designs only over their allowable stress range, and then scaling them if their maximum load did not reach the prescribed load-range. For the displacement-range constraint, several formulations of a displacement penalty were provided. One formulation employs scaling to allow for a *range* of acceptable displacements, enabling the genetic algorithm to focus primarily on optimizing the shape function. As long as springs are designed within a *smaller* design space and their total displacement is *less than* the prescribed displacement-range, the designs can be scaled up to meet exact displacement requirements while maintaining stress constraints.

Design Parameterization

The nonlinear spring design parameterization introduced in this work employs boundary conditions and a specific use of curves (splines) to make it conducive to geometric nonlinearities. Chapter 3 provided a simple demonstration of how boundary conditions at the input can induce nonlinearities on a simple cantilever spring design. Chapter 6 illustrated that the nonlinear responses of four springs closely correlated with their magnitude of axial stresses over their range of motion. Thus, by constraining as spring's input along a path, the spring is forced to stretch or compress during its range of

motion, activating its axial stiffness and potentially inducing nonlinearities. Bending stresses are less influential in this regard but greatly contribute to a spring's resulting displacement-range, since bending stresses are limited by the stress constraint. Thus, the parameterization employs long, slender splines that enable large geometric nonlinearities within prescribed stress constraints.

The discrete nature of the design parameterization enables several other benefits. First, splines can assume either fixed or pinned end conditions. Pinned endpoints enable large geometric nonlinearities while minimizing bending stresses. The constant-force spring in Chapter 5 utilized this benefit. Second, the ability to turn splines "on" and "off" enabled the generation of fully connected planar spring designs that utilize the entire design space. If two splines happen to overlap in the initial configuration, one spline is simply turned off. Thus, the loop and overlap checks combined with the uniform size variable generated planar spring designs of constant thickness which are easier to manufacture. Applicable primary manufacturing methods include stamping (when the out-of-plane thickness is small), forming/bending strips of material (when the out-of-plane thickness is large), injection molding, and die casting.

Implementation

The design parameterization was easy to implement into nonlinear finite element analysis and discrete optimization routines, including a genetic algorithm and a local polling search method. For the nonlinear analysis, it was helpful to employ an arc-length method to measure the degree of instability within a design. This was accomplished by checking for the largest negative slope in a design's load-displacement function. In the end, checking for negative eigenvalues in a spring's system matrix proved to be the most robust indication of buckling.

10.1.2 Contributions

This dissertation provided several contributions to the field of compliant mechanism/spring design. The main contributions are summarized as follows:

- Development of a generalized nonlinear spring synthesis methodology that
  (i) synthesizes a spring for any prescribed load-displacement function and

(ii) generates designs with distributed compliance. The methodology produces planar, non-buckling spring designs that meet specified stress, material, and space requirements. Its objective function exploits scaling rules to improve optimization performance and meet specified load- and displacement-ranges within the allowable stress range.

- Development of a design parameterization that is conducive to geometric nonlinearities and implementable in nonlinear finite element analysis. Key features of the parameterization include: (i) a branching network of compliant beams used for topology synthesis, (ii) curved beams without sudden changes in cross-section, offering a more even stress distribution, and (iii) boundary conditions that impose both axial and bending loads on the compliant members and enable large rotations while minimizing bending stresses.

Other relevant and important contributions include:

- Formulation of guidelines for arranging nonlinear springs in series and parallel, offering new design options and applications for nonlinear springs.
- Formulation of scaling rules based on the elastic flexure formula (stress equation) and the beam deflection formulas. Besides improving design optimization, these scaling rules are powerful tools when modifying existing spring designs to meet new design requirements.
- Demonstration of the practical utility of the synthesis methodology by designing a nonlinear spring for (i) an automotive seat cushion assembly and (ii) constant-force applications. The nonlinear spring prototypes confirmed the nonlinear response of the physical springs and revealed several manufacturing precautions and sensitivities relative to nonlinear spring fabrication.

This research provided additional insights on nonlinear spring design. The main insights are summarized below:

- Geometric nonlinearities and boundary conditions enable spline segments (beam elements) to vary the contribution of their axial stiffness over the spring's range of motion. When the magnitude of a spring's axial stiffness response is nonlinear, springs are likely to have a correlating nonlinear load-displacement response. The influence that axial stresses have on a spring's response seems independent of the fluctuation of bending stresses.
- The folding and unfolding deformations of single spline topologies have fairly predictable nonlinear responses. A spring folding on itself generally has a stiffening response, while a spring unfolding generally has a softening response. The combination of these two deformations is capable of generating constant stiffness responses.
- The nonlinear spring design parameterization is suitable for generating spring designs that match prescribed responses in two different directions.
- The nonlinear spring parameterization can be converted to a compliant mechanism parameterization and successfully generate compliant mechanisms. The modified parameterization offers two new benefits to compliant mechanism synthesis: simplified designs (a single load path) and smooth nonlinear geometries. Using this parameterization, geometric nonlinearities can be exploited to produce nonlinear relationships between the input and output points.

10.2 Future Work

10.2.1 Synthesis of Three Dimensional Nonlinear Springs

A logical extension of planar spring design is three dimensional spring design. For example, Chapter 5 presented the synthesis of a linear spring design. A linear spring has a three dimensional counterpart, the helical spring. The planar spring has a

rectangular cross-section and is dependent on both axial and bending forces, while the helical spring has a circular cross-section and is primarily dependent on torsional forces. It remains to be investigated how a nonlinear spring, like an S-curve spring that first softens and then hardens, would be designed in three dimensions.

Before converting the nonlinear spring design parameterization to a three dimensional design space, several considerations must be made:

- Torsion will be an additional mode of loading. This research has already explored the effects that axial and bending loads have on planar spring designs. Now, the influence of torsional stresses must be investigated with relation to a spring's stiffness response.
- The cross-sectional geometry must be either chosen or optimized to accommodate axial, bending, and torsion loads.
- The scaling rules for planar springs are no longer applicable when torsion is included as a mode of deformation.
- Boundary conditions at the input remain to be determined due to the three additional degrees of freedom. Similar to planar spring designs, boundary conditions that encourage geometric nonlinearities and minimize stresses are most favorable.
- Expanding the design parameterization model to a three dimension space further complicates overlap and looping checks.
- With more degrees of freedom, the splines may warp into positions having lower potential energy, thereby lowering the load capacity of the springs.

10.2.2 Synthesis of Nonlinear Springs with Adjustable Stiffness

The utility of nonlinear springs would broaden by designing them for adjustable stiffness. For instance, one may require a constant-force spring to be adjustable across a range of forces. Preliminary studies in this research (not included within this dissertation) have revealed that the rotation of nonlinear springs about their input causes continuous alterations of their load-displacement functions. An equivalent adjustment would be leaving the spring in its original orientation and rotating the translational slide

that the input traverses. Depending on the design, the spring's shape function, load-range, and/or displacement-range is usually sensitive to the rotation, enabling the spring's stiffness to be adjustable. A proposed synthesis problem is provided as follows: Design a constant-force spring that has a load-range of F_1 at zero degrees rotation and a load-range of F_2 at 10 degrees rotation (clockwise). Therefore, at intermediate rotations, the resulting spring should have continuous load-ranges between F_1 and F_2. In conclusion, the synthesis of adjustable nonlinear springs should be further investigated to determine the best objective function formulation for this problem.

10.2.3 Compliant Mechanism Synthesis

The previous chapter introduced a design parameterization for compliant mechanisms. More studies are needed to determine whether this parameterization outperforms the other existing compliant mechanism design parameterizations. As mentioned earlier, the parameterization already offers two new benefits: simplified design (a single load path) and smooth nonlinear geometries.

Secondly, it was shown that geometric nonlinearities can cause significant nonlinear responses in compliant mechanisms. These geometric nonlinearities require a considerable level of compliance (i.e. energy storage). For applications requiring energy transmission to the output, an energy efficiency metric should be added to the objective function and tested for its performance.

10.2.4 Improving the Current Nonlinear Spring Synthesis Approach

The computational time for the nonlinear spring synthesis methodology could be reduced by making the following improvements. First, the parameters (constants) for the objective function and the genetic algorithm could be optimized to reduce the number of design analyses necessary to generate optimal designs. Second, a better understanding of when to employ the local search could speed the convergence to a local or global optimum. Finally, each spring's analysis time could potentially decrease by eliminating the use of a commercial FEA software program and implementing FEA code directly into the Matlab program already containing the genetic algorithm.

As a starting point, nine splines were arbitrarily chosen to provide adequate complexity within the design parameterization. This research shows that generated spring topologies rarely employed three primary splines within their final designs. Therefore, a simplified design parameterization having only two branches should be investigated for its performance within the genetic algorithm. Once again, each branch would have one primary spline and two secondary splines, reducing the total number of splines from nine to six.

Finally, this research has revealed that a translational slide at the input helps induce axial stresses, which facilitate nonlinear responses. However, these axial forces and boundary conditions cause reaction forces perpendicular to the slide. Thus, low friction components, such as bearings, are sometimes needed to enable smooth motion of the input. Therefore, this tradeoff between nonlinearity and slide reaction forces should be investigated to minimize frictional forces without hindering the nonlinear responses of the springs.

BIBLIOGRAPHY

Abramson, M. A., 2006, “NOMADm” version 3.85 User’s Guide.

Ananthasuresh, G.K. and Kota, S., 1995, "Designing Compliant Mechanisms," Mechanical Engineering, **117**(11), pp. 93-96.

Ananthasuresh, G. K., Kota, S., and Kikuchi, K., 1994, “Strategies for Systematic Synthesis of Compliant MEMS,” 1994 International Mechanical Engineering Congress and Exposition, ASME, Chicago, IL, **55**, pp. 677–686.

Bajaj, A. and Krousgrill, C.M., 2001, “Nonlinear System Resonance Phenomena,” *Encyclopedia of Vibrations* (Ed. S.G. Braun), Academic Press, San Diego, pp. 928-935.

Beer, F. P. and Johnston, E.R., 1992, *Mechanics of Materials*, McGraw-Hill.

Benavides, G.L., Adams, D. P., and Yang, P., 2001, “Meso-Machining Capabilities,” Sandia National Laboratories, SAND2001-1708.

Bruns, T.E. and Tortorelli, D.A., 2001, “Topology Optimization of Non-linear Elastic Structures and Compliant Mechanisms,” Computer Methods in Applied Mechanics and Engineering, **190**(26-27), pp. 3443-59.

Buhl, T., Pedersen, C. B. W., and Sigmund, O., 2000, “Stiffness Design of Geometrically Non-Linear Structures Using Topology Optimization,” Structural and Multidisciplinary Optimization, **19**(2), pp. 93–104.

Buscemi, K., 2004, “Assembly: One goal, one part,” Appliance Manufacturer, **52**(8), pp. 44-46.

Chipperfield, A., Fleming, P., Pohlheim, H., and Fonseca, C., 2002, “Genetic Algorithm Toolbox for Use with Matlab,” User’s Guide Version 1.2.

Eiben, A.E. and Smith, J.E., 2003, *Introduction to Evolutionary Computing*, Springer-Verlag.

Frecker, M., Ananthasuresh, G.K., Nishiwaki, N., Kikuchi, N., and Kota, S., 1997, “Topological Synthesis of Compliant Mechanisms using Multi-Criteria Optimization,” ASME Journal of Mechanical Design., **119**(2), pp. 238–245

Geissdorfer, S., Putz, A., and Engel, U., 2006, “Microforming – Current Status and Future Demands,” Journal of Mechanical Engineering, **52**(7-8), pp. 495-505.

Goldberg, D., 1989, *Genetic Algorithms in Search, Optimization, and Machine Learning,* Addison-Wesley.

Herder, J., 2001, “Energy-free Systems. Theory, conception, and design of statically balanced spring mechanisms.” PhD-thesis. Delft University of Technology, Delft, The Netherlands.

Herrero, A., Goenaga, I., Azcarate, S., Uriarte, L., Ivanov, A., Rees, A., Wenzel, C., and Muller, C., 2006, “Mechanical Micro-Machining Using Milling, Wire EDM, Die-Sinking EDM and Diamond Turning,” Journal of Mechanical Engineering, **52**(7-8), pp. 484-494.

Hetrick, J.A., 1999, “An Energy Efficiency Approach for Unified Topological and Dimensional Synthesis of Compliant Mechanisms,” Ph.D. Dissertation, University of Michigan, Ann Arbor.

Hetrick, J.A., Kota, S., 1999, “An Energy Formulation for Parametric Size and Shape Optimization of Compliant Mechanisms,” ASME Journal of Mechanical Design, **121**, pp. 229-234.

Hibbitt, Karlsson, and Sorensen, 2004, “ABAQUS Analysis User’s Manual” ver. 6.5.

Howell, L.L., 2001, *Compliant Mechanisms*, John Wiley and Sons, Inc.

Howell, L.L. and Midha, A., 1994, “A Method for the Design of Compliant Mechanisms with Small-Length Flexural Pivots,” ASME Journal of Mechanical Design, **116**(1), pp. 280-290.

Howell, L. L., Midha, A., and Murphy, M.D., 1994, “Dimensional Synthesis of Compliant Constant-force Slider Mechanisms,” Machine Elements and Machine Dynamics: Proceedings of the 1994 ASME Mechanisms Conference, DE-Vol. 71, pp. 509-515.

Humphrey, J.D., Strumpf , R.K., and Yin, F.C.P., 1990, "Determination of a Constitutive Relation for Passive Myocardium: I. A New Functional Form," Journal of Biomechanical Engineering, **112,** pp. 333-339.

Humphrey, J.D., Strumpf , R.K., and Yin, F.C.P., 1990, "Determination of a Constitutive Relation for Passive Myocardium: II. Parameter Estimation," Journal of Biomechanical Engineering, **112**, pp. 340-346.

Jenuwine, J.G. and Midha, A., 1994, “Synthesis of Single-Input and Multiple-Output Port Mechanisms with Springs for Specified Energy Absorption,” ASME Journal of Mechanical Design, **116**, pp. 937-943.

Joo, J. and Kota, S., 2004, “Topological Synthesis of Compliant Mechanisms Using Nonlinear Beam Elements,” Mechanics Based Design of Structures and Machines, **32**(1), pp. 17-38.

Joo, Y., Kota, S., and Kikuchi, N., 2000, "Topological Synthesis of Compliant Mechanisms Using Linear Beam Elements," Mechanics of Structures and Machines, **28**(4), pp. 245-280.

Kim, C.J., 2005, "A Conceptual Approach to the Computational Synthesis of Compliant Mechanisms", Ph.D. Dissertation, University of Michigan, Ann Arbor.

Klisch, S.M. and Lotz, J.C., 1999 , "Application of a Fiber-reinforced Continuum Theory to Multiple Deformations of the Annulus Fibrosus," Journal of Biomedical Engineering, **32**(10), pp. 1027-36.

Klute, G.K., Berge, J.S., and Segal, A.D., 2004, "Heel-region Properties of Prosthetic Feet and Shoes," Journal of Rehabilitation Research and Development, **41**(4), pp. 535-545.

Knauf, T., LaValley, R., Sivulka, B., and Thomas, J., "Compliant Seat Cushion Pan for an Automotive Seat," University of Michigan. December 2006.

Kota, S., Joo, J., Li, Z., Rodgers, S. M., and Sniegowski, J., 2001, "Design of Compliant Mechanisms: Applications to MEMS," Analog Integrated Circuits and Signal Processing, **29**(1-2), pp. 7-15.

Lan, C. and Cheng, J., 2007, "Distributed Shape Optimization of Compliant Mechanisms Using Intrinsic Functions," Proceedings of the 2007 ASME Design Engineering Technical Conferences, Las Vegas, NV, DETC2007-34191.

Levy, R. and Spillers, W.R., 2003, *Analysis of Geometrically Nonlinear Structures*, Kluwer Academic Publishers.

Lu, K., 2004, "Synthesis of Shape Morphing Compliant Mechanisms", Ph.D. Dissertation, University of Michigan, Ann Arbor.

Lu, K. and Kota, S., 2003, "Design of Compliant Mechanisms for Morphing Structural Shapes," Journal of Intelligent Material Systems and Structures, **14**(6), pp. 379-391.

Lu, K. and Kota, S., 2006, "Topology and Dimensional Synthesis of Compliant Mechanisms Using Discrete Optimization," ASME Journal of Mechanical Design, **128**(5), pp. 1080-91.

Migliore, S.A., Brown, E.A., and DeWeerth, S.P., 2007, "Novel Nonlinear Elastic Actuators for Passively Controlling Robotic Joint Compliance," ASME Journal of Mechanical Design, **129**(4), pp. 406-412.

Murphy, M. D., 1993, "A Generalized Theory for the Type Synthesis and Design of Compliant Mechanisms," Ph.D. Dissertation, Purdue University, West Lafayette, Indiana.

Parmley, R.O., 2000, *Illustrated Sourcebook of Mechanical Components*, McGraw-Hill.

Paros, J.M. and Weisbord, L., 1965, "How to Design Flexural Hinges," Machine Design, Nov. 25, pp. 151-156.

Pedersen, C., Buhl, T., and Sigmund, O., 2001, "Topology Synthesis of Large-Displacement Compliant Mechanisms," International Journal for Numerical Methods in Engineering, **50**, pp. 2683-2705.

Pedersen, C.B.W., 2004, "Crashworthiness Design of Transient Frame Structures Using Topology Optimization," Computer Methods in Applied Mechanics and Engineering, **193**(6-8), pp. 653-678.

Pedersen, C.B.W., Fleck, N.A., and Ananthasuresh, G.K., 2006, "Design of a Compliant Mechanism to Modify an Actuator Characteristic to Deliver a Constant Output Force," ASME Journal of Mechanical Design, **128**(5), pp. 1101-1112.

Precision Meso Manufacturing. Sandia National Laboratories. 18 Jan 2008 <http://www.sandia.gov/mst/organizations/meso-mfg.html>.

Rai, A., Saxena, A., Mankame, N.D., and Upadhyay, C.S., 2006, "On Optimal Design of Compliant Mechanisms for Specified Nonlinear Path Using Curved Frame Elements and Genetic Algorithm," Proceedings of the 2006 ASME Design Engineering Technical Conferences, Philadelphia, PA, DETC2006-99298.

Rapid Prototyping Laboratory. 17 Jan 2008. Stanford University. 18 Jan 2008 <http://www-rpl.stanford.edu>.

Rhoads, J.F., Shaw, S.W., Turner, K.L., and Baskaran, R., 2005,"Tunable Microelectromechanical Filters that Exploit Parametric Resonance," Journal of Vibration and Acoustics, **127**(5), pp. 423-430.

Rodgers, M.S., 2005, "Non-Linear Actuator Suspension for Microelectromechanical Systems." United States Patent No. 6,894,420.

Saxena, A. and Ananthasuresh, G.K., 2001, "Topology Synthesis of Compliant Mechanisms for Nonlinear Force-Deflection and Curved Path Specifications," ASME Journal of Mechanical Design**, 123**(1), pp. 33-42.

Sigmund, O., 1997, "On the Design of Compliant Mechanisms Using Topology Optimization," Mechanics of Structures and Machines, **25**(4), pp. 495-526.

Tai, K. and Akhtar, S., 2005, "Structural Topology Optimization Using a Genetic Algorithm with Amorphological Geometric Representation Scheme," Structural and Multidisciplinary Optimization**, 30**(2), pp. 113–127.

Vogel, S., 1998, *Cats' Paws and Catapults*, W. W. Norton.

Xu, D. and Ananthasuresh, G.K., 2003, "Freeform Skeletal Shape Optimization of Compliant Mechanisms," ASME Journal of Mechanical Design, **125**(2), pp. 253-261.

Zhou, H. and Ting, K., 2006, "Shape and Size Synthesis of Compliant Mechanisms Using Wide Curve Theory," ASME Journal of Mechanical Design, **128**(3), pp. 551-558.